

UNIVERSITÀ DEGLI STUDI DI MODENA E REGGIO EMILIA
DIPARTIMENTO DI INGEGNERIA “ENZO FERRARI”

PhD SCHOOL

INDUSTRIAL AND ENVIRONMENTAL ENGINEERING
INGEGNERIA INDUSTRIALE E DEL TERRITORIO

XXXII CYCLE

**AN INVESTIGATION ON CYCLE-TO-CYCLE VARIABILITY
IN INTERNAL COMBUSTION ENGINES USING PROPER
ORTHOGONAL DECOMPOSITION AND LARGE-EDDY
SIMULATIONS**

Advisor:

Prof. Stefano Fontanesi

Candidate:

Federico Rulli

PhD School Director:

Prof. Alberto Muscio

Abstract

The main goal of research on reciprocating internal combustion engines (ICEs) consists in increasing the power output while reducing pollutant emission and fuel consumption. Cycle-to-cycle variability (CCV) is closely coupled with the intrinsic turbulent nature of in-cylinder flow and is detrimental in terms of combustion efficiency, fuel consumption, and tailpipe emissions. Due to fluctuations in flame propagation, heat release, and burnt product formation, CCV is now seen as one of the major limiting factors for higher power output and lower fuel consumption in ICEs. Therefore, it is essential to understand and control CCV to improve the overall engine efficiency and performance. Experimental techniques like particle image velocimetry (PIV) provide a powerful technical support for the analysis of the spatial and temporal evolution of the flow field in ICEs. Proper orthogonal decomposition (POD) has been largely used in conjunction with PIV to analyze flow field characteristics. Several methods involving POD have been proposed in the recent years to analyze engine CCV. In this work, phase-dependent POD analysis, conditional averaging, triple and quadruple POD decomposition methods are introduced and applied to a large database of PIV data from the optically accessible TCC-III research engine. Results are discussed with particular emphasis on the capability of the methods to perform both quantitative and qualitative evaluations on CCV. A new quadruple POD decomposition methodology is proposed and compared to those available in the literature. Besides experimental techniques, Computational Fluid Dynamics (CFD) has become a fundamental tool for understanding the complex aero-thermochemical processes that take place in the cylinder and for driving the development of new technological solutions. Large-eddy simulation (LES) is the most practical simulation tool to understand the nature of CCV. This work investigates LES capabilities to simulate CCV. The accuracy and the reliability of CFD simulations stands in the models used for the discretization of the fluid domain and for the numerical computation of the governing equations. Three subgrid-scale models are assessed on 50 LES cycles datasets on the TCC-III engine under motored conditions by means of comparison with the experimental results and phase dependent POD analysis on a portion of the intake and compression stroke. The findings of this analysis are used to furtherly improve the LES results focusing on the meshing strategy. This last plays a central role in the computational efficiency, in the management of the moving components of the engine, and in the accuracy of results. The overset mesh approach, usually referred to as Chimera grid or Composite grid, was rarely applied to the simulation of ICEs, mainly because of the difficulty in adapting the technique to the specific complexities of ICE flows. This work demonstrates the feasibility and the effectiveness of the overset mesh technique application to ICEs thanks to a purposely designed meshing approach. 50 LES cycles were performed on the TCC-III engine under motored conditions. The proposed POD quadruple decomposition methodology is extensively applied to assess both the accuracy of the simulated results and the potential of the method itself for understanding CCV.

Il principale obiettivo della ricerca sui motori a combustione interna (internal combustion engines, ICEs) consiste nell'incremento della potenza erogata a fronte di una contemporanea riduzione di consumi ed emissioni inquinanti. La variabilità ciclica (Cycle-to-cycle variability, CCV) è fortemente legata alla natura intrinsecamente turbolenta della fluidodinamica dei motori a combustione interna, ed i suoi effetti sono nocivi sull'efficienza di combustione, sul consumo di carburante e sulle emissioni inquinanti. A causa delle fluttuazioni nella propagazione del fronte di fiamma, nel rilascio di calore e nella formazione dei prodotti di combustione, la CCV è individuata tra i fattori più limitanti per il raggiungimento di sempre più alte potenze specifiche a fronte di minori consumi. È dunque fondamentale capire e controllare la CCV per migliorare l'efficienza e le prestazioni dei motori. Tecniche sperimentali come la Particle Image Velocimetry (PIV) forniscono un importante supporto tecnico per l'analisi dell'evoluzione spaziale e temporale dei flussi nei motori. La Proper Orthogonal Decomposition (POD) è stata largamente usata insieme alla PIV per analizzare le caratteristiche del campo di moto dei motori. Negli ultimi anni, diversi metodi basati sulla POD sono stati proposti per analizzare la CCV sui motori. In questo lavoro vengono illustrati la phase-dependent POD, la media condizionale, e la decomposizione tripla e quadrupla della POD. Questi metodi sono applicati ad un vasto database di dati PIV sul motore di ricerca ad accesso ottico TCC-III. I risultati sono discussi dando particolare risalto alle capacità di ciascun metodo di dare una stima sia qualitativa che quantitativa della CCV. Un nuovo metodo di decomposizione quadrupla della POD viene proposto e comparato ai metodi presenti in letteratura. Oltre alle tecniche sperimentali, la fluidodinamica computazionale (Computational Fluid Dynamics, CFD) è ormai diventata uno strumento imprescindibile per la comprensione dei complessi fenomeni aero-termochimici che hanno luogo nel cilindro e per guidare lo sviluppo di nuove soluzioni tecniche. Le simulazioni LES (large-eddy simulations) sono lo strumento più indicato per simulare la CCV. In questo lavoro è stato valutato il potenziale della LES nella simulazione della CCV. Tre modelli di subgrid sono stati valutati tramite dataset da 50 cicli LES sul motore TCC-III in trascinato attraverso la comparazione con i risultati sperimentali ed una phase-dependent POD su una porzione della corsa di aspirazione e compressione. Le evidenze riscontrate in questa analisi vengono usate per migliorare ulteriormente i risultati lavorando sulla strategia di discretizzazione (meshing). Quest'ultima assume un ruolo centrale nell'efficienza computazionale, nella gestione dei componenti in movimento nel motore e nell'accuratezza dei risultati. L'approccio Overset mesh, chiamato anche Chimera o Composite grid, è stato raramente applicato ai motori, soprattutto a causa delle difficoltà nell'adattamento di questa tecnica alle complessità specifiche della fluidodinamica dei motori. In questo lavoro viene dimostrata l'applicabilità della tecnica overset mesh ai motori a combustione interna, attraverso un approccio di discretizzazione sviluppato appositamente, e ne viene mostrata l'efficacia. 50 cicli LES sono stati calcolati sul motore TCC-III in trascinato. La tecnica di decomposizione quadrupla della POD sviluppata è stata ampiamente applicata per valutare sia l'accuratezza dei risultati simulati, sia l'efficacia del metodo stesso nella comprensione della CCV.

Table of contents

Introduction

- 1.1 Background and motivation
- 1.2 Cycle-to-cycle variability
- 1.3 Methods of analysis of CCV
- 1.4 Large Eddy Simulations
- 1.5 Proper Orthogonal Decomposition
- 1.6 Objectives of the work

Chapter 1

Transparent Combustion Chamber (TCC-III) engine

Chapter 2

Physical models and numerical methods for motored flow

- 2.1 Turbulence
- 2.2 Direct Numerical Simulation (DNS)
- 2.3 Reynolds-averaged Navier Stokes (RANS)
- 2.4 Large Eddy Simulation (LES)
 - 2.4.1 Smagorinsky subgrid scale model
 - 2.4.2 Dynamic structure model

Chapter 3

Proper Orthogonal Decomposition

- 3.1 Introduction
- 3.2 Mathematical procedures
- 3.3 Phase-dependent POD analysis
- 3.4 Conditional averaging methodology
- 3.5 POD Triple decomposition
- 3.6 POD Quadruple decomposition

3.7 Alternative POD decomposition

3.8 Discussion

Chapter 4

LES investigation: subgrid models and quality criteria

4.1 Numerical setup

4.2 LES quality indices

4.3 Results

Chapter 5

LES Analysis using the overset mesh technique

5.1 Overset Mesh

5.2 Numerical Setup

5.2.1 Mesh

5.2.2 Boundary layer mesh approach

5.2.3 Computational setup

5.3 Results

5.3.1 Tumble center

5.3.2 POD results

5.3.3. POD quadruple decomposition results

5.4 Conclusions

Conclusions and future research

Definitions / Acronyms

References

Introduction

1.1 Background and motivation

The topic of CO₂ and fuel consumption reductions from vehicles is a very broad and complex issue, encompassing vehicle regulations, biofuel mandates, and a vast assortment of engine and vehicle technologies. From 2020 the regulation (EC) No 443/2009 of the European Parliament and of the Council establishes CO₂ emission performance requirements for new passenger cars to achieve the target of 95 g CO₂/km for the average emissions of the new car fleet as measured in accordance with Regulation (EC) No 715/2007. The reduction of GreenHouse Gas (GHG) emission has become a mandatory target in engine research to fight the climate change. According to a study [1] by the U.S. National Research Council, there are four potential technology pathways that can reduce fuel consumption and GHG emissions by 80% from the LDV fleet by 2050: highly efficient conventional vehicles, biofuels, plug-in hybrid and electric vehicles, and hydrogen fuel cell vehicles. In the current market, light-duty vehicles run mostly using internal combustion engines (ICEs) with fuels such as gasoline, diesel, compressed natural gas, liquefied petroleum gas, and flex-fuel. Despite the spread of Battery Electric Vehicles, the projections on the sales, shown in Figure 1, highlights how the role of ICEs will continue to be predominant in the transport sector.

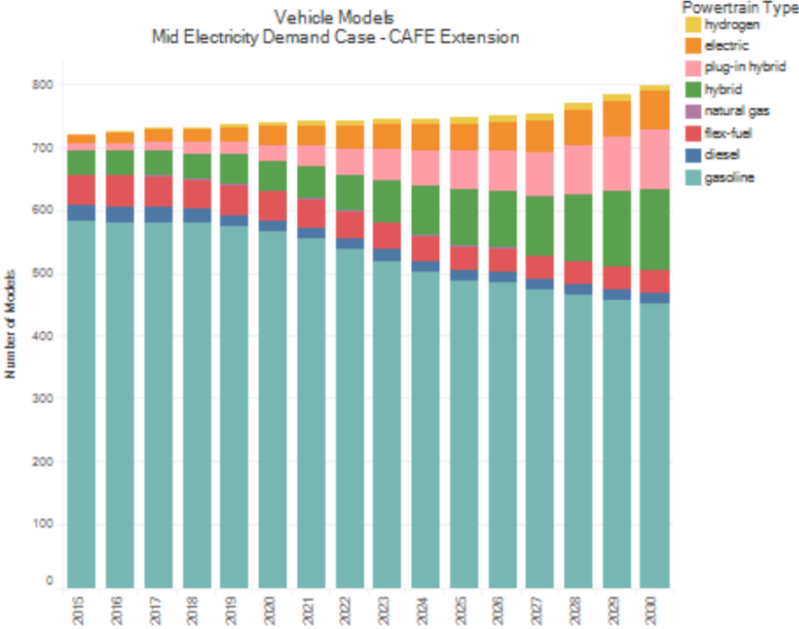


Figure 1 Number of the projections on light-duty vehicle demand [2]

The report from the Global Fuel Economy Initiative [3] projects that even with the cost reduction in the non-conventional technology (fuel cells and batteries) based vehicles, global sales of ICE based vehicles will have a larger market share until about 2040, and will remain significant well after 2040. This leads us to the conclusion that improvements in the fuel economy and GHG emissions of ICEs is of utmost importance. The fuel efficiency and the pollutant emissions in ICEs are closely coupled with the complex aero-thermo-chemical processes that take place inside the cylinder. One way to increase the overall fuel efficiency of ICEs is the reduction/elimination of cycle to cycle variability.

1.2 Cycle-to-cycle Variability

Cycle-to-cycle variability (CCV) is nowadays seen as one of the most limiting factors in increasing the specific power in Internal Combustion Engines (ICEs). Even though the components in a spark ignited piston engine follow a repeatable law of motion, the time evolution of the cylinder pressure shows a scatter of the individual cylinder pressure curves around the phase averaged mean. As a result, the work provided by each single cycle is different from the mean work, which is the design target for the engine. CCV may jeopardize combustion efficiency, drivability, fuel consumption, and tailpipe emissions. In extreme cases misfire or partial burns may occur, causing the increase in pollutant emissions. In 1994, Ozdor estimated that the complete or partial elimination of CCV could provide up to a 10% increase in power output for the same fuel consumption[4]. Nowadays, the main objective of research on ICEs is the increase in the power output with the contemporary reduction of the emission of the green-house gas CO₂. Among the technologies introduced to fulfill this target, the increased dilution rates of fresh charge by exhaust gas recirculation and the aim of a lean combustion tend to decrease the laminar flame speed. This could lead to a further amplification of the cyclic variations [5]. Therefore, it is essential to understand and control the mechanisms that lead to CCV to improve the overall engine efficiency and performance. CCV is closely coupled with the intrinsic turbulent nature of in-cylinder flow. The local flow pattern around the spark plug at the early stage of the flame kernel development can convect the spark kernel away from or towards the electrodes. This could either reduce or emphasize local quenching phenomena and the early flame propagation. Since the early phases of combustion play a fundamental role on the history of flame propagation, turbulence-related flow perturbations will certainly increase CCV. Other factors impacting on CCV exist, such as large-scale gas-dynamics, injection and ignition repeatability. A significant contribution to CCV comes in fact from combustion related factors, such as mixture composition, ignition, and flame propagation. In the last decades, several studies on Cycle-to-cycle variations[4-6] have identified some leading factors, such as:

- Variations of the spark discharge characteristics
- Variation of in-cylinder mixture

- Spatial mixture inhomogeneity at the spark plug
- Variations of turbulence intensity
- Variations of the mean flow speed and direction in the spark plug vicinity
- Variations of the overall in-cylinder flow pattern

All these phenomena are closely coupled and it's hard to determine their relative importance in the occurrence of cyclic variations. Besides, since an ICE works under different loads and environmental conditions during the normal usage, the leading factors for CCV may not always be the same[6]. However, the literature agrees on the intake turbulence being the leading actor in changing flame propagation and related combustion pathway[7].

1.3 Methods of analysis for CCV

It is extremely difficult to analyze and understand engine CCV, due to the complex superimposition of many different mechanisms. The cylinder pressure has been used to measure the fluctuations. This has led to the use of pressure related parameters to quantify the fluctuation intensity. The maximum pressure and its crank angle location are frequently used parameters, together with the indicated mean effective pressure (IMEP) produced per engine cycle. The standard deviation is usually normalized with the average value to give a coefficient of variation, COVimep. These parameters have the benefit of requiring no modeling and the COVimep shows how much torque fluctuation that the transmission etc. must tolerate, and it is therefore used as an indicator for the component design. The major drawback with the parameters derived from the pressure is the lack of knowledge on the ongoing process. The importance of those mechanisms and their interactions can hardly be studied using only standard engine experiments based on cylinder pressure analysis[6].

To address the effects of flow variability without the hurdle of other CCV-promoting factors, extensive analyses on engines in motored condition can help isolating flow-effects on cyclic variability.

The rapid development of optical diagnostic techniques such as Particle Image Velocimetry provided a powerful technical support to the study of CCV[8, 9]. PIV has been used to measure in-cylinder flow velocities in reciprocating ICEs since 1989[10]. Since then, the adoption of high-speed lasers and digital cameras made possible to make PIV measurements through the entire engine cycle for multiple contiguous cycles[11]. These flow measurements are essential for resolving cycle-to-cycle flow variations, as well as the cause-and-effect relationships between flow, mixing, and combustion. PIV measurements also gave a fundamental contribution in the validation and the development of computational techniques such as large eddy simulation (LES) [12].

1.4 Large Eddy Simulations

In conjunction with the experimental techniques, computational fluid dynamics (CFD) simulations have become a fundamental tool in ICE design and development, thanks to its ability of giving an insight on the complex aero-thermochemical processes that take place in the cylinder. CFD has been applied to a wide variety of phenomena related to the ICE, such as heat transfer[13-15], combustion [16-18], pollutant formation[19], knock events [20-22], and Cycle-to-Cycle variability[23-25]. To improve the computational efficiency and the accuracy of results, extensive research has been done on methods of the CFD, such as numerical schemes, turbulence models, wall-functions, and mesh motion strategies. In an ICE, the strategy adopted to handle the motion of the valves and the piston plays a fundamental role. The gaps are extremely thin and high pressure and temperature are involved. Therefore, the mesh motion strategy must guarantee reliability, stability and the conservation of turbulent quantities. The approach implemented in many commercial software, such as STAR-CD, licensed by SIEMENS PLM, is the so-called “dynamic cell layering”, consisting in adding or removing layers of cells in accordance with the motion of a translating boundary (i.e. the valves and the piston), while the majority of the grid remains fixed. A set of control vertices is used to define the initial movement imposed to the mesh by the morpher. Another widely used method is the morphing motion formulation. A displacement vector is associated with each control vertex and is used to move nearby vertices. These displacements are used to generate an interpolation field using multiquadric interpolation theory [26]. This approach was as well implemented in many CFD commercial packages, like VECTIS, licensed by RICARDO, and FIRE, licensed by AVL. The overset grids approach was first introduced in 1983[27]. The computational domain is composed by several different meshes. Each moving component is surrounded by a dedicated mesh, which interacts with the background mesh and the other moving components meshes through interpolation in the overlapping zones. More details on this technique will be illustrated later on. Problems involving multiple bodies relative motion are easily handled thanks to the flexibility of this approach in matching each different grid component. A wide use of overset grids has been done in industrial applications, specifically in aerospace. However, the complexity of ICEs simulation makes the implementation of this methodology challenging. Only few applications are available in the literature[28], but the level of flexibility guaranteed by the overset approach makes its application to ICEs desirable and promising. Turbulence models are an essential part of CFD simulations. Even though Unsteady Reynolds Averaged Navier Stokes (URANS) analysis is still the most-established method to design and develop ICEs, RANS models are designed to capture the ensemble averages. Therefore, only little information can be obtained on CCV, because a higher turbulent viscosity tends to dampen or remove the variations in in-cylinder flows and combustion, that coincide with cycle-to-cycle variability. A RANS approach can still be used to predict deeply stochastic phenomena, as for example knock [20], and URANS can predict variability under different degrees of dilution of the air-fuel mixture with

exhaust gas recirculation [29]. However, the literature agrees on the necessity of relying on Scale Resolving Simulations (SRS), e.g. Large Eddy Simulations (LES), to simulate and understand CCV. Thanks to a lower dissipation in LES turbulence models compared to a RANS model, a higher level of kinetic energy usually characterizes LES flows and more flow structures, eddies, and vortices are represented on the computational grid. LES models are designed to filter the smallest scales and retain the less dissipative largest scales, responding to the non-linearities inherent to the Navier-Stokes equations. Therefore, LES simulations have the intrinsic potential to simulate many aspects of the cyclic fluctuations[30]. Extended reviews on the state of the art of LES application for internal combustion engines can be found in [31-33]. Since many engine cycles must be simulated while performing an LES analysis on CCV, a compromise between accuracy and LES quality must be found to optimize the necessary computing resources. In order to assess the quality of the simulation and to provide the necessary localized mesh resolution, severe research efforts were made to develop LES quality indices[34-36].

Haworth et al.[33, 37] were among the first to study cycle-to-cycle variability in a motored engine, simulating several motored cycle and studying instantaneous flow structures. More recently, an increasing number of studies were dedicated to cycle-to-cycle velocity fluctuations by means of LES simulations, considering their impact on spray, mixing process, and ignition [38-42]. Despite a considerable number of investigations though, the relevant underlying physics of cycle-to-cycle variability is not yet fully understood. Many attempts have been made to divide the velocity field in three parts including the mean part, a low-frequency part and a high frequency part by means of Fast Fourier Transform [43, 44], but the difficulties in determining cutoff and the consequent differences in results made non-definitive conclusions. LES capabilities in making both quantitative and qualitative analysis on cycle-to-cycle variability are well established. It's harder to evaluate LES capabilities to understand the origin of cycle-to-cycle variability and to use it as a tool to reduce it.

1.5 Proper Orthogonal Decomposition

Many analysis methods rely on Proper Orthogonal Decomposition (POD). POD was first introduced into the turbulence field by Lumley in 1967[45]. POD has been widely presented as a powerful and elegant method of data analysis aimed at obtaining low-dimensional approximate descriptions of high-dimensional processes[46]. In recent years it has been proposed as a promising tool to objectively extract and identify coherent structures in turbulent flows. POD has been applied to in-cylinder velocity data of reciprocating engines by a number of groups[47-52]. Graftieaux et al. [53] suggested using POD to separate pseudo-fluctuations attributed to the unsteady nature of the large-scale vortices from fluctuations due to small-scale turbulence. Chen et al. [54] proposed a practical guide to apply POD in

ICE research. Several methods of analysis can be found in literature based on the so-called phase dependent POD, performed with the “method of snapshots” introduced by Sirovich[55]. Buhl et al [30] proposed the conditional averaging method. Roudnitzky et al [56] proposed the POD triple decomposition and Qin et al. [57] proposed the quadruple decomposition.

1.6 Objectives of the work

This work focuses on CCV on two main aspects: on one side the capability of POD in understanding cyclic variations. Several methods of analysis involving POD were tested on an experimental PIV dataset publicly available for the TCC-III engine in motored conditions [58]. A new quadruple POD decomposition is proposed with the intent of improving the drawbacks highlighted in the previously mentioned methods. On the other side, first an assessment over three subgrid-scale models is performed. From the findings of this research, the Overset mesh methodology is investigated to improve the accuracy of the CFD simulation of CCV. Thanks to a purposefully designed mesh approach, the Overset Mesh methodology was firstly applied to an ICE for CCV investigation. Results are shown to assess the accuracy of the simulation. The new quadruple POD decomposition methodology is applied to this dataset.

The thesis is structured as follows:

- In chapter 1 the experimental setup of the TCC-III engine is recalled.
- In chapter 2 a brief introduction on turbulence and CFD theory is given.
- In chapter 3 first, a theoretical introduction on POD is given. Each analyzed method is briefly recalled to highlight the underlying principles and assumptions. Then, the developed method for an alternative quadruple POD decomposition is proposed and its potential in describing flow-originated CCV is highlighted.
- In chapter 4 the analysis of three subgrid scale models is given on three 50 LES cycles dataset on the TCC-III engine. Results are analyzed in terms of ensemble average comparison, alignment parameter, and POD analysis on both simulated and experimental results
- In chapter 5, first an introduction on the overset mesh methodology is given. Then, the computational setup for 50 LES cycles on the TCC-III engine is described and results are shown. Finally, the POD quadruple decomposition is extensively applied and results are discussed.
- Finally, conclusions are summarized and a perspective on future research is discussed.

Chapter 1

TCC-III engine

The first version of the TCC engine (TCC-0) was designed and built by General Motors in 1990. The engine was designed to provide benchmark data at the next logical level beyond the Imperial College data on ICEs, where laser-doppler anemometry was used to quantify the mean velocity and turbulence characteristics of the isothermal and incompressible flow within a piston-cylinder arrangement motored without compression at 200rpm[59]. Several publications have been made on the first version of the TCC [9, 60-62]. Then, in 2010 the TCC-II version was created to renew the fundamental investigation of CCV using experiments in conjunction with the evaluation of three different LES approaches[12]. As for the original design, the geometry was purposefully chosen to be simple for ease of computational gridding, and optimized for optical access to the entire combustion chamber. The TCC-II configuration had the same engine geometry but a different intake system, exhaust system, and valve seat (two angles) compared to the TCC-0. The experimental results from the TCC-II configuration were useful for establishing the LES-to experimental data-comparison protocols, to identify desired improvements in the hardware and operating procedures, and to assess the impact of engine and system imperfections on the in-cylinder flow. Based on the TCC-II studies, new results are reported here from a third configuration, TCC-III, which has refurbished valve hardware and the intake/exhaust systems upgraded for fired testing. Also, the TCC-III data are significantly more repeatable and with expanded operating conditions.

The TCC-III optical engine, illustrated in Figure 2. It is a spark-ignition 2-valve, 4-stroke, pancake-shaped combustion chamber engine with a geometrical compression ratio of 10:1. It is equipped with a full quartz cylinder and a 70 mm-diameter flat quartz piston window. The intake air, intake port and plenum, exhaust port, and coolant are heated to maintain an engine temperature of 318 K to minimize thermal gradients in air flow during motored operation. Each intake and exhaust port is connected to a plenum. Detailed engine specifications are listed in Table 1.

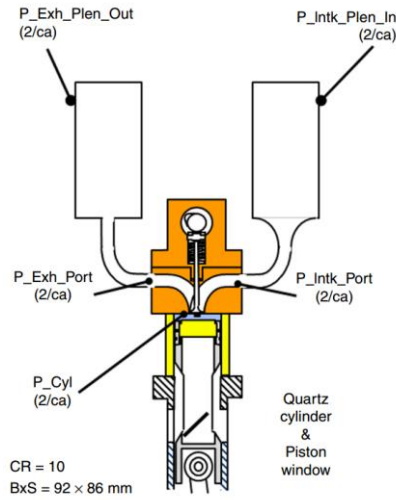


Figure 2 Schematic of TCC Engine and high-speed pressure measurement locations[58]

Parameter	Specification
Engine	TCC-III engine
Displacement Volume	570 cc
Bore	92 mm
Stroke	86 mm
Compression Ratio	10.0
Engine Speed	1300 RPM
Intake Pressure	0.4 bar

Table 1 TCC-III engine specifications

A full quartz liner and quartz piston-top window allow maximum optical access to the pancake-shaped combustion chamber. Silicone-oil droplets are added to the intake air and illuminated with a high-repetition-rate frequency doubled Nd:YLF laser (Darwin Duo, Quantronix). Images of the Mie scattering signal are recorded using a monochrome high-speed CMOS camera (Phantom v1610, Vision Research) with a 1280x800 pixel sensor. All velocity fields are calculated with a commercial particle-image velocimetry (PIV) code (DaVis v8.x, LaVision GmbH) employing a decreasing interrogation window with a final window size of 32x32 pixel with 50% overlap. This leads to spatial velocity resolution of approximately 2.6 mm and a vector separation of 1.3 mm. Velocity data are acquired successively in the four planes shown in Figure 3, at an interval of 2.5 Crank Angles (CA). The field of view in horizontal planes ($z = -5$ mm and $z = -30$ mm) is limited by the piston window to approximately 70 mm in diameter, and in vertical planes ($x = 0$ mm and $y = 0$ mm) to approximate 70 mm in width.

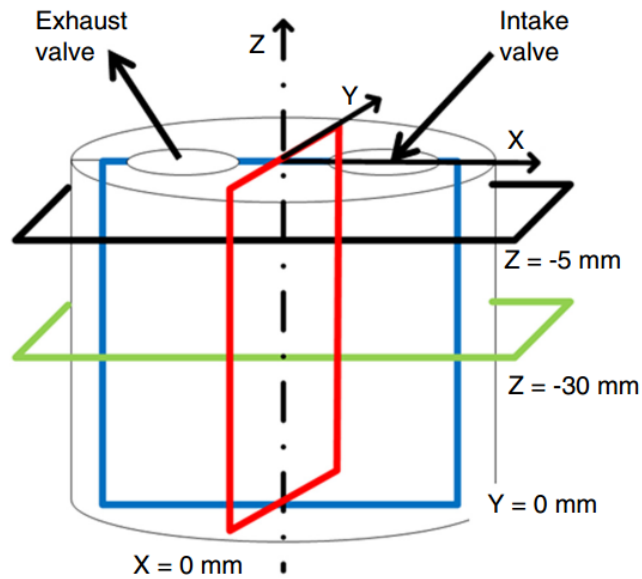


Figure 3 PIV planes for the TCC-III engine[58]

The PIV measurement of each section plane were recorded successively every 5 CA for at least 235 cycles. Even though the PIV measurements were carried out on the four section planes at different times, full similarity between different PIV measurements in terms of pressure traces and flow motion was achieved. A detailed description of the experimental setup can be found in [58]. On $Y=0$ and $X=0$ planes, PIV data are recorded on a 52×82 grid with a base size of 1.15 mm. On the $Z= -5$ and $Z= -30$ planes, PIV data are recorded on a 49×50 grid, with a base size of 1.38 mm. Due to the limitations in optical access on the Z plane, the flow field is available on 75% of the bore dimension. The TCC-III engine is well known in the literature for the reliability and the accuracy of the experimental data provided. For this reason, it is chosen as reference dataset for the following analysis.

In this work, the dataset identified as S_2013_10_24_01 is used. This dataset has been generated from 240 consecutive cycles. The analysis focuses on the XZ plane, considered as the most representative of the in-cylinder flow.

Chapter 2

Physical models and numerical methods for motored flow

The flow inside an ICE is always turbulent in nature. An essential feature of turbulent flows is that the fluid velocity field significantly and irregularly varies in both position and time. Due to the high velocity of the motion of piston and valves, the turbulent structures continuously vary during the cycle, and the flow structures at a particular phase/CA can vary from a cycle to another. In this chapter, turbulence is introduced, and the numerical models used to simulate it are described. The turbulence theory is synthesized from [63]. Specific attention is given to the Kolmogorov hypothesis that will be mentioned in Section 3.6.

2.1 Turbulence

Turbulence consists of fluid motions over a wide range of length and time scales. In engineering applications turbulent flows are prevalent, thanks to the ability of turbulence of transporting and mixing fluids much more effectively than a comparable laminar flow. Turbulence is also effective at mixing the momentum of the fluid, resulting, for example, in an increase in the drag and the wall shear stress on an aircraft's wing. Similarly, compared to laminar flows, rates of heat and mass transfer at solid-fluid and liquid-gas interfaces are much enhanced in turbulent flows. For high Reynolds number there is a separation of scales. The large-scale motions are strongly influenced by the geometry of the flow (i.e. by the boundary conditions), and they control the transport and mixing. The behavior of the small-scale motions, on the other hand, is determined almost entirely by the rate at which they receive energy from the large scales and by the viscosity. Therefore, the small-scale motions have a universal character, independent of the flow geometry. The idea of the energy cascade, introduced by Richardson in 1922, is that kinetic energy enters the turbulence (through the production mechanism) at the largest scales of motion. The first concept in Richardson's view of the energy cascade is that the turbulence can be considered to be composed of eddies of different sizes. These eddies have energy of the order of u_0^2 and a timescale of $\tau_0 = l_0/u_0$, where u_0 , l_0 and τ_0 are the characteristic velocity, length and time scales of the largest eddies, respectively. Hence, the rate of energy transfer/dissipation will scale as $u_0^2/\tau_0 = u_0^3/l_0$, independent of the viscosity.

The energy is transferred (by inviscid processes) to smaller and smaller scales until, at the smallest scales, the energy is dissipated by viscous action. Kolmogorov in 1941 added and quantified this picture. In particular, he identified the smallest scales of turbulence to be those that now bring his name. His theory is based on three hypotheses. The first hypothesis concerns the isotropy of the small-scale

motions: while the large eddies are anisotropic and largely affected by the boundary conditions, the directional bias of the large scales are lost in the chaotic scale-reduction process. Therefore:

Kolmogorov's hypothesis of local isotropy: at sufficiently high Reynolds number, the small-scale turbulent motions ($l \ll l_0$) are statistically isotropic.

A demarcation to define the length scale where the vortices are anisotropic is identified with $l_{EI} \approx 1/6 l_0$. All the information about the geometry of the large eddies, determined by the boundary conditions, is also lost when the energy passes down the cascade. As a consequence, the statistics of the small-scale motions are similar for every high-Reynolds number turbulent flow. In the energy cascade (for $l < l_{EI}$), the two dominant processes are the transfer of energy to successively smaller scales, and viscous dissipation. A plausible hypothesis, then, is that the important parameters are the rate at which the small scales receive energy from the large scales (called T_{EI}) and the kinematic viscosity ν . The dissipation rate ε is determined by the energy transfer rate T_{EI} , so that these two rates are nearly equal. Consequently:

Kolmogorov's first similarity hypothesis: In every turbulent flow at sufficiently high Reynolds number, the statistics of the small-scale motions ($l < l_{EI}$) have a universal form that is uniquely determined by ν and ε .

Given the two parameters ε and ν , there are unique length, velocity, and time scales that can be formed. These Kolmogorov scales are:

$$\eta \equiv \left(\nu^3/\varepsilon\right)^{1/4} \quad [2.1]$$

$$u_\eta \equiv (\nu\varepsilon)^{1/4} \quad [2.2]$$

$$\tau_\eta \equiv (\nu/\varepsilon)^{1/2} \quad [2.3]$$

Kolmogorov scales characterize the very smallest, dissipative eddies. On the small scales, all high-Reynolds number turbulent velocity fields are statistically similar and they are statistically identical by the Kolmogorov scales. However, at sufficiently high Reynolds number, there is a range of scales l that are very small compared with l_0 , and yet very large compared with η , i.e. $l_0 \gg l \gg \eta$. In this range eddies are much bigger than dissipative eddies, and it can be supposed that their motion is little affected by the effect of viscosity. Consequently:

Kolmogorov's second similarity hypothesis: In every turbulent flow at sufficiently high Reynolds number, the statistics of the motions of scale l in the range $l_0 \gg l \gg \eta$ have a universal form that is uniquely determined by ε , independent of ν .

A lengthscale l_{DI} (with $l_{DI} = 60\eta$) is introduced, so that the range in the above hypothesis can be written $l_{EI} \gg l \gg l_{DI}$. This lengthscale splits the universal equilibrium range into two subranges: the inertial subrange $l_{EI} > l > l_{DI}$ and the dissipation range $l < l_{DI}$. In the energy cascade, a quantity of central importance, denoted as $T(l)$, is the rate at which energy is transferred from eddies larger than l to those smaller than l . If this transfer process is accomplished primarily by eddies of size comparable to l , then $T(l)$ can be expected to be in the order of $u(l)^2/\tau(l)$.

The energy contained in different length scales can be represented by the energy spectrum function $E(k)$, where $k = \frac{2\pi}{l}$ is the wavenumber which is inversely proportional to the length scale l . $E(k)$ is the turbulent energy contribution per unit mass per unit wavenumber from the eddies corresponding to wavenumber k . The energy spectrum for an isotropic turbulence in the log-log format is shown in Figure 4. To summarize, the spectrum is divided in three parts over the wavenumber/length scale range:

- 1) The energy containing range with the large-scale eddies
- 2) The dissipation range with the small-scale eddies
- 3) The inertial subrange with all the scales in between

The area under the energy-spectrum function gives the total turbulent kinetic energy.

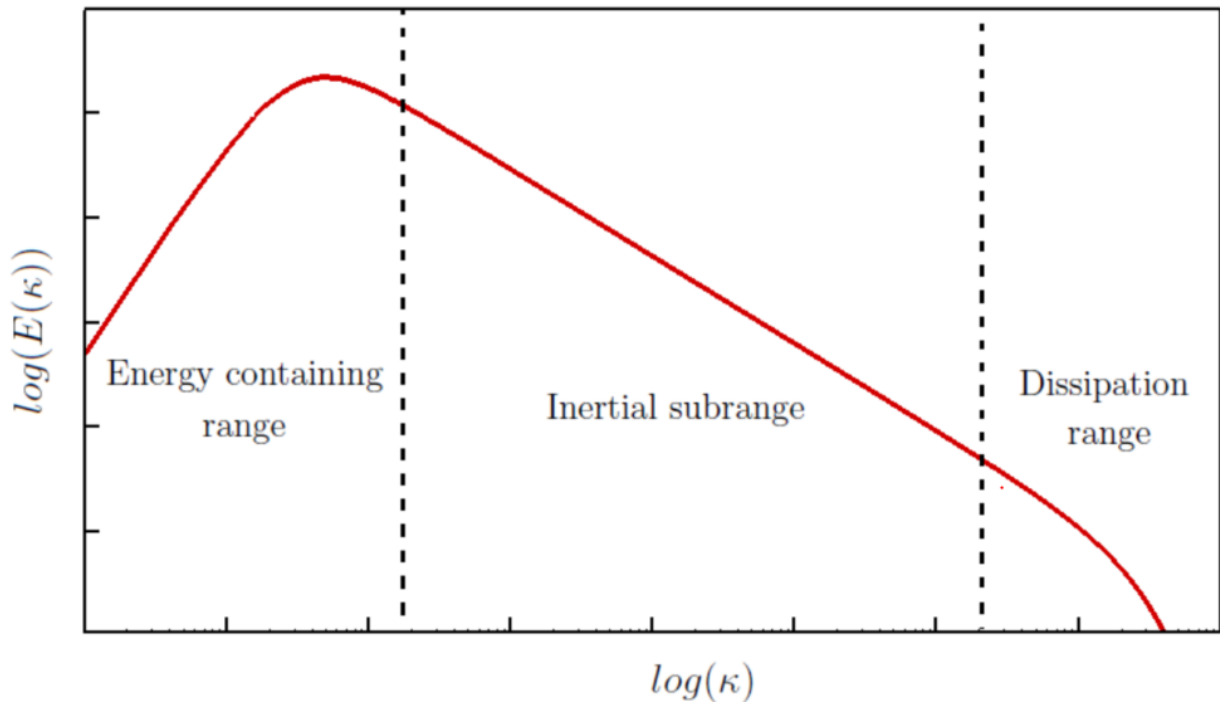


Figure 4 Energy spectrum for isotropic turbulence

There are three general ways to simulate turbulent flows:

- Direct Numerical Simulation (DNS)
- Reynolds Averaged Navier Stokes (RANS)
- Large Eddy Simulation (LES)

2.2 DNS

Navier-Stokes equations describe the three dimensional flow field of a generic fluid; they are a system of 5 differential equations along with two equations of state. The most straightforward method for the numerical solution of a fluid-dynamic field, is the one based on the direct discretization of the Navier-Stokes equations and it is called Direct Numerical Simulation (DNS). The obtained solutions are exact, that is they retain the fluctuation contributions typical of turbulent phenomena: a time average of the obtained solutions will then be needed to get a solution describing the mean flow motion of the fluid.

Nevertheless, the direct solution of the Navier-Stokes equations leads to relevant problems: they mostly come from the computational cost: only using extremely fast and massively-parallel super computers with huge memory amounts, together with very refined numerical techniques, it is possible to get solutions within acceptable times. In fact, in order to have a correct solution, the computational grid must be so fine that it is able to capture all the temporal and spatial scales of the fluid-dynamic field.

This leads to extremely fine grids and very small computational/integration time steps. Up to the present times, hardware evolution is still far away from allowing the researchers to apply DNS for practical problems except for very “simple” cases. Nevertheless, DNS is extremely useful to provide a forecast of the flow field in standard geometries which require “acceptable” computational demands. These simplified geometries can then become test-cases for the validation of the other subsequent approaches.

2.3 RANS

The Reynolds-Averaged Navier-Stokes equations (RANS) are derived from the time-averaging operation performed on the Navier-Stokes original set of equations. Time-averaging is based on the decomposition of a generic fluctuating variable into a mean part and a fluctuation around the mean value. The resulting set of equations expresses the time-averaged behaviour, or in case of quasi-periodic flows such as those in internal combustion engines, phase-averaged flow realizations.

RANS equations need closure terms to model the Reynolds Stresses, i.e. the product terms between velocity fluctuations.

In this context the 2-equations k- ϵ turbulence model is developed and it is still nowadays the most widespread and used model for turbulent flows in commercial CFD software. The idea is introducing two transport equation for k and ϵ . These have the form of:

$$\frac{\partial(\bar{\rho}k)}{\partial t} + \nabla \cdot (\bar{\rho}k\bar{u}) = \nabla \cdot \left(\frac{\mu_t}{\sigma_k} \nabla k \right) + 2\mu_t \tilde{S}_{ij} \tilde{S}_{ij} - \bar{\rho}\epsilon \quad [2.4]$$

$$\frac{\partial(\bar{\rho}\epsilon)}{\partial t} + \nabla \cdot (\bar{\rho}\epsilon\bar{u}) = \nabla \cdot \left(\frac{\mu_t}{\sigma_\epsilon} \nabla \epsilon \right) + C_{1\epsilon} \frac{\epsilon}{k} 2\mu_t \tilde{S}_{ij} \tilde{S}_{ij} - C_{2\epsilon} \frac{\epsilon}{k} \bar{\rho}\epsilon \quad [2.5]$$

The modeled equations give a relation for the energy transfer represented by the energy-cascade process, which is determined by the problem-dependent large-scale motions. The equations above, represent the turbulent kinetic energy and its dissipation rate process at a small scale.

The origin of the model comes from experimental observations: at high Reynolds numbers, the energy dissipation rate and the turbulent kinetic energy undergo variations in time which are more or less proportional. An increase of k corresponds to an increase of ϵ of equal intensity, and vice versa; the same happens for decreasing rates. From a mathematical perspective, this is converted into a direct proportionality between the productive and dissipative terms of k and ϵ : this assumption is called “turbulent equilibrium hypothesis”. The mentioned time correlation which stands between k (defined in

m^2/s^2) and the dissipation rate ε (m^2/s^3) represents the inverse of the time-scale of the large scale eddies, i.e. it indicates the turn-over frequency of the large-scale eddies, measured in s^{-1} .

One major advantage of k - ε model is that it is based on the Boussinesq assumption, typical of eddy viscosity turbulence models. It allows to simplify the evaluation of the turbulent stresses, reducing computational times and explaining why such models are the most used from an industrial point of view for the analysis of turbulent flows. Another advantage is their considerable robustness: from a computational point of view they are highly stable and efficient. On the contrary, some inner simplifications in the transport equations can lead to poor accuracy in the representation. Major error sources in two-equation models are the turbulent equilibrium assumption and the Boussinesq hypothesis. As for the turbulent equilibrium assumption, this is sufficiently true only for free-flows at high Reynolds numbers. Boussinesq hypothesis introduces the concept of eddy viscosity in perfect analogy with the molecular one; the definition as a scalar, implicitly, imposes an isotropy condition to the eddy viscosity. This assumption leads to a linearity between the strain rate and the Reynolds stresses, which is never verified, except for very simple flows, far from solid walls; for complex fields, highly distorted, where geometry effects are relevant (bended pipes, etc.), a linear relation is wrong.

2.4 LES

In large-eddy simulation (LES), the large three-dimensional unsteady turbulent motions are directly represented, while the effects of the smaller-scale motions are modelled. LES' computational cost lies between Reynolds-stress models and DNS. Since the large-scale motions are represented explicitly, LES is expected to be more accurate and reliable than Reynolds-stress models for flows in which large-scale unsteadiness is significant. There are four conceptual steps in LES.

- 1) A filtering operation is defined to decompose the velocity $\mathbf{U}(\mathbf{x}, t)$ into the sum of a filtered (or resolved) component $\bar{\mathbf{U}}(\mathbf{x}, t)$, which represents the motion of large eddies, and a residual (or subgrid-scale, SGS) component $\mathbf{u}'(\mathbf{x}, t)$.
- 2) The equations for the evolution of the filtered velocity field are derived from the Navier-Stokes equations.
- 3) Closure is obtained by modelling the residual-stress tensor, most simply by an eddy-viscosity model.
- 4) The model filtered equations are solved numerically for $\bar{\mathbf{U}}(\mathbf{x}, t)$, which provides an approximation to the large-scale motions in one realization of the turbulent flow.

As mentioned in 1), the governing equations for LES are obtained by spatially filtering the instantaneous continuity and Navier-Stokes equations. Each quantity can be decomposed as the sum of the spatially filtered contribution and the fluctuations about the spatially filtered value. For example:

$$u_i = \bar{u}_i + u_i' \quad [2.8]$$

Here, u_i is the velocity component in the i -direction, $\bar{(\cdot)}$ denotes a spatially filtered quantity, and $(\cdot)'$ is the associated fluctuations about the spatially filtered quantity. The filter velocity is defined by:

$$\bar{u}_i(x, t) = \int G(x, x') u_i(x', t) dx' \quad [2.9]$$

Where $G(x, x')$, the filter kernel, is a localized function. Filter kernels, which have been applied in LES include a Gaussian, a box filter (a simple local average) and a cutoff (a filter which eliminates all Fourier coefficients belonging to wavenumber above a cutoff). Every filter has a length scale associated with it, Δ . Roughly, eddies of size larger than Δ are large eddies while those smaller than Δ are small eddies, the ones that need to be modeled. When the Navier-Stokes equations with constant density (incompressible flow) are filtered, a set of equations similar to the RANS equations is obtained:

$$\frac{\partial(\rho \bar{u}_i)}{\partial t} + \frac{\partial(\rho \bar{u}_i \bar{u}_j)}{\partial x_j} = -\frac{\partial \bar{p}}{\partial x_j} + \frac{\partial}{\partial x_j} \left[\mu \left(\frac{\partial \bar{u}_i}{\partial x_j} + \frac{\partial \bar{u}_j}{\partial x_i} \right) \right] \quad [2.10]$$

Since the continuity equation is linear, filtering does not change it:

$$\frac{\partial(\rho \bar{u}_i)}{\partial x_j} = 0 \quad [2.11]$$

It is important to note that, since

$$\overline{\bar{u}_i \bar{u}_j} \neq \bar{u}_i \bar{u}_j \quad [2.12]$$

And the quantity on the left side of this inequality is not easily computed, a modeling approximation for the difference between the two sides of this inequality must be introduced:

$$\tau_{ij}^s = -\rho(\overline{\bar{u}_i \bar{u}_j} - \bar{u}_i \bar{u}_j) \quad [2.13]$$

In the context of LES, τ_{ij}^s is called the subgrid-scale Reynolds stress. The width of the filter Δ is not necessarily linked to the grid size h , however $\Delta > h$.

2.4.1 Smagorinsky subgrid-scale model

The earliest and most commonly used subgrid scale model is the one proposed by Smagorinsky in 1963. It is based on a Boussinesq hypothesis, it is therefore an eddy viscosity model. All such models are based on the notion that the principal effects on SGS Reynolds stress are increased transport and dissipation. The model can be viewed in two parts. First, the linear eddy-viscosity model

$$\tau_{ij}^r = -2\nu_r \bar{S}_{ij} \quad [2.14]$$

Is used to relate the residual stress to the filtered rate of strain. The coefficient $\nu_r(\mathbf{x}, t)$ is the eddy viscosity of the residual motion. Second, using Prandtl's mixing-length hypothesis, the eddy viscosity is modelled as:

$$\nu_r = l_s^2 \bar{S} = (C_s \Delta)^2 \bar{S} \quad [2.15]$$

Where \bar{S} is the characteristic filtered rate of strain, l_s is the Smagorinsky lengthscale (analogous to the mixing length) which, through the Smagorinsky coefficient C_s , is proportional to the filter width Δ . According to the eddy-viscosity model, the rate of transfer of energy to the residual motion is

$$P_r \equiv -\tau_{ij}^r \bar{S}_{ij} = 2\nu_r \bar{S}_{ij} \bar{S}_{ij} = \nu_r \bar{S}^2 \quad [2.16]$$

For the Smagorinsky model (and for every eddy-viscosity model with $\nu_r > 0$), the energy is always transferred from the filtered motions to the residual motions, without any backscatter. Most of the methods apply to isotropic turbulence and they all agree that $C_s \approx 0.2$. Unfortunately, C_s is not constant: it is zero in laminar flow and it is attenuated near walls compared with its value in high-Reynolds-number free turbulent flows. Therefore, it may be a function of Reynolds number and/or other non-dimensional parameters and may take different values in different flows. It can be calculated using the van Driest damping that has long been used to reduce the near-wall eddy viscosity in RANS models:

$$C_s = C_{s0} \left(1 - e^{-n^+/A^+}\right)^2 \quad [2.17]$$

Where n^+ is the distance from the wall in viscous wall units and A^+ is a constant.

The dynamic model provides a methodology for determining an appropriate local value of the Smagorinsky coefficient. The dynamic model is based on the scale similarity assumption. The idea, introduced by Bardina et al.[64], is that the smallest scales that are resolved in a simulation are similar in many ways to the still smaller scales that are treated via the model. The model was proposed by Germano et al. [65]. The velocity \bar{u}_i can be filtered using a filter broader than the one used in the LES

itself to obtain a very large scale field \bar{u}_i . An effective subgrid-scale field can be obtained by subtraction of the two fields. By multiplying and filtering, the subgrid-scale Reynolds stress tensor produced by that field can be computed. From the large-scale field, the Reynolds stress produced by the model can be estimated.

$$\tau_{ij}^R \equiv \overline{U_i U_j} - \bar{U}_i \bar{U}_j \quad [2.18]$$

$$T_{ij} \equiv \widetilde{\overline{U_i U_j}} - \widetilde{\bar{U}_i \bar{U}_j} \quad [2.19]$$

An identity due to Germano is obtained by applying the test filter to Eq. 2.18 and subtracting the results from Eq. 2.19:

$$L_{ij} \equiv T_{ij} - \widetilde{\tau_{ij}^R} = \widetilde{\overline{U_i U_j}} - \widetilde{\bar{U}_i \bar{U}_j} \quad [2.20]$$

The term L_{ij} , which is called resolved stress, is known in terms of \tilde{U} , whereas T_{ij} and τ_{ij}^R are not. L_{ij} can be interpreted as the contribution to the residual stress from the largest unresolved motions.

This can be done at every spatial point at every timestep. For this model it is fundamental to assume that the same model with the same value of the parameter C_s can be applied to both the actual LES and LES done on a coarser scale. A secondary assumption that is made more for convenience than necessity is that the parameter is independent of location.

2.4.2 Dynamic Structure Model (DSM)

The eddy-viscosity-based model, like the Smagorinsky one, are purely dissipative and there is no backscattering. This is not always true as energy can also flow in the reverse direction. Also, equal amounts of energy are dissipated from every scale in the Smagorinsky model. To overcome this limitation, in the dynamic structure model the subgrid stresses are modeled as:

$$T_{ij} = c_{ij} k_r \quad [2.21]$$

$$k_r = \frac{1}{2} (\overline{u_i u_j} - \bar{u}_i \bar{u}_j) \quad [2.22]$$

Where c_{ij} is a symmetric tensor and k_r is the subgrid turbulent kinetic energy. The tensor c_{ij} has components with negative values, that introduce backscattering. Since the components are not equal in every location, the energy dissipation will not be equal, i.e. lower energy will be dissipated from the larger scales and higher energy will be dissipated from smaller scales. To define the tensor c_{ij} , a test level model is defined:

$$T_{ij} = c_{ij}K \quad [2.23]$$

$$K = \frac{1}{2}(\widetilde{u_i u_j} - \widetilde{u_i} \widetilde{u_j}) = \widehat{k} + \frac{1}{2}L_{ij} \quad [2.24]$$

Using the test level kinetic energy, K , can be written as a function of the sub-grid kinetic energy and the trace of the L_{ij} tensor. Then, the Germano identity is used to formulate an equation for the tensor coefficient c_{ij} :

$$L_{ij} = Kc_{ij} - \widehat{kc_{ij}} \quad [2.25]$$

By solving this integral equation for the coefficient tensor, or by assuming that the coefficient tensor can be brought outside the integral, the dynamic structure model becomes:

$$\tau_{ij} = \left(\frac{L_{ij}}{L_{kk}} \right) 2k \quad [2.26]$$

Therefore, the dynamic structure model is a one-equation, non-turbulent viscosity model [66]. In Section 4 an evaluation of the abovementioned SGS models is shown on three 50 LES cycles datasets on the TCC-III engine.

Chapter 3

Proper Orthogonal Decomposition

3.1 Introduction

POD has been described as an elegant method of data analysis aimed at obtaining low-dimensional approximate description of high-dimensional processes [46].

In recent years, the Proper Orthogonal Decomposition (POD) has been extensively used as an analysis tool for evaluating the turbulence of in-cylinder reciprocating engine flows thanks to its potential for resolving the discourse between turbulence and cyclic variability [67]. POD was first introduced in 1967 by Lumley [45] for application to atmospheric turbulence to separate eddies with scales on the order of the average flow by the turbulent motion, whose scale is substantially smaller. Grafiteux et al. [53] suggested using POD to separate pseudo-fluctuations attributed to the unsteady nature of the large-scale vortices fluctuations due to small-scale turbulence. Many applications on in-cylinder flows were presented. Baby et al. [7] used POD to demonstrate its capability to separate small scale turbulent fluctuations from cycle-to-cycle variations. Bizon et al. used POD to reconstruct missing data from an optically accessible engine in order to obtain pseudo-cycle-resolved sequences [68] and demonstrates that the use of POD has allowed the analysis of cyclic variations of two-dimensional scalar combustion images [69]. Buhl et al. [30] used POD as an objective method to identify subsets to perform a conditional average for the analysis of CCV. Roudnitzky et al. [56] proposed an energy-based filtering procedure based on the POD that recognizes the mean part, the coherent and the incoherent part of the turbulence, while Qin et al. [57] proposed a further decomposition with the recognition of a transition part. These last methods will be furtherly analyzed later on. Liu and Haworth [50] described the main POD approach for the analysis of ICEs and extend the phase invariant approach, firstly introduced by Fogleman [47]. Chen et al. produced a practical guide for the use and the interpretation of POD in internal combustion engines analysis [67, 70].

POD technique decomposes any original vector or scalar field into a sum of weighted linear basis functions, usually called modes ϕ^i . The modes can be computed from two-component 2D velocity distributions, but also from 3D distributions and from one component scalar distributions. In the so-called phase-dependent POD, also referred to as method of snapshots, the modes are generated from a sample of snapshots, in our case, the PIV/LES velocity fields. In practice, the snapshots are samples of the velocity field obtained at a discrete spatial location and at discrete instants in time. The number of modes is equal to the considered number of snapshots. In addition, the modes are orthogonal to each other and normalized so that the magnitude of each mode is unity. The energy of each mode in each

snapshot is given by the so-called POD coefficients. Their value depends on the projection of each mode onto the single snapshot. The contribution of each mode to the single snapshot determines the weight of that single mode in the snapshot. Consequently, each snapshot can be reconstructed by summing all modes multiplied by their respective coefficients for that snapshot [30].

The method of snapshots can be applied only to velocity fields that are obtained from multiple engine cycles at a given CA position, that's why this analysis is also called "phase dependent" POD. The intent is to extract the dominant energy-containing structures for a defined phase. The objective of the "phase invariant" POD is to provide a single set of POD modes that is representative of the flow dynamics over the full engine cycle [50]. For this purpose, snapshots obtained at multiple piston positions must be used. To deal with the change of the geometry due to the piston position, three modifications were proposed in [47]: a linear spatial transformation was applied so that the velocity components are defined at the same spatial locations (a baseline grid) for all snapshots. Second, a linear velocity transformation was applied to retain the one-dimensional global dilatation from each snapshot during the spatial transformation. And third, the velocities were rescaled so that each snapshot has the same kinetic energy prior to performing the POD analysis.

In this work, "phase dependent" POD was used. In particular, several methods involving POD were applied to the experimental dataset of the TCC-III engine in motored condition to assess their potential and limitations in analyzing CCV. Then, a new quadruple POD decomposition methodology is proposed and compared to those available in the literature. This section is structured as follows: first the mathematical procedures of POD are given. Then, phase dependent POD, triple, and quadruple decomposition are introduced and applied to the TCC-III engine. Results are discussed with particular emphasis on the capability of the methods to perform both quantitative and qualitative evaluations on CCV. Then, a new quadruple POD decomposition methodology is proposed and compared to those available in the literature[71].

3.2 Mathematical procedures

A brief theoretical introduction on phase-dependent POD follows. For a given CA position, the input data for the POD consists of N two-dimensional velocity fields $V_{CA}^{(N)} = (u_{i,j}, w_{i,j})^{(N)}$, where i,j are the indices of the grid points of the PIV measurements, and N is the index of the velocity field. Consequently, for each snapshot a number of M points, with $M = i \times j$ is used for the POD analysis. A $M \times N$ matrix A is created at each CA position,

$$A_n^m = \begin{bmatrix} a_1^1 & a_1^2 & \cdots & a_1^N \\ a_2^1 & a_2^2 & \cdots & a_2^N \\ \vdots & \vdots & \ddots & \vdots \\ a_M^1 & a_M^2 & \cdots & a_M^N \end{bmatrix} \quad [3.1]$$

There are no general rules on how rows and columns of the A matrix must be organized. Since the considered flow field is a vector field, we chose to set the A matrix as below:

$$A_n^m = [u^1 \quad u^2 \quad \cdots \quad u^N] = \begin{bmatrix} u_1^1 & u_1^2 & \cdots & u_1^N \\ u_2^1 & u_2^2 & \cdots & u_2^N \\ \vdots & \vdots & \ddots & \vdots \\ u_M^1 & u_M^2 & \cdots & u_M^N \\ w_1^1 & w_1^2 & \cdots & w_M^1 \\ w_2^1 & w_2^2 & \cdots & w_M^2 \\ \vdots & \vdots & \ddots & \vdots \\ w_M^1 & w_M^2 & \cdots & w_M^N \end{bmatrix} \quad [3.2]$$

The covariance $N \times N$ matrix R is calculated as:

$$R = A^T A \quad [3.3]$$

The eigenvalue problem is given by Eq. 3.4

$$Rv^i = \lambda^i v^i \quad [3.4]$$

A set of eigenvalues in decreasing order is obtained by solving the eigenvalue problem. A set of eigenvectors corresponding to each eigenvalue is also calculated.

Then, POD modes are calculated as:

$$\phi^i = \frac{\sum_{n=1}^N v_n^i u^n}{\|\sum_{n=1}^N v_n^i u^n\|} \quad [3.5]$$

With $i = 1, 2, \dots, N$

POD coefficients for snapshot n are obtained by Eq. 3.6

$$a_i = \phi^i u^n \quad [3.6]$$

Finally, the snapshot reconstruction is carried out as:

$$u^n = \sum_{i=1}^N a_i^n \phi^i \quad [3.7]$$

The energy content of each mode is represented by its corresponding eigenvalue. Consequently, the energy fraction of each mode is obtained as from Eq. 3.8:

$$e_i = \frac{\lambda_i}{\sum_{n=1}^N \lambda_n} \quad [3.8]$$

3.3 Phase-dependent POD analysis

Several methods of analysis are based on POD. In POD decomposition, POD modes are processed to perform a flow reconstruction of the main turbulent structures. POD can also be used as a standalone analysis method. Many examples can be found in the literature [50, 70, 72]. To understand the information given by this method, it is worth to focus on the physical meaning of the POD modes. POD is a purely mathematical method and a physical interpretation is not necessarily allowed. However, the literature agrees on the interpretation of, at least, the first mode. The first POD mode is generally associated with the average flow field. Observed confirmation can be found in Figure 5, where the first three POD modes and the average flow field are shown for four significant crank angle positions, namely:

- 240CA, exhaust stroke
- 475CA, intake stroke
- 540 CA, BDC of expansion stroke
- 630CA, compression stroke

The tumble flow structure generation during the intake stroke, as well as its decay during the compression stroke, are visible. The first mode is very similar to the average flow for all the snapshots. The energy spectrum related to the second and the third modes provides some information about their weight in reconstructing the original flow field.

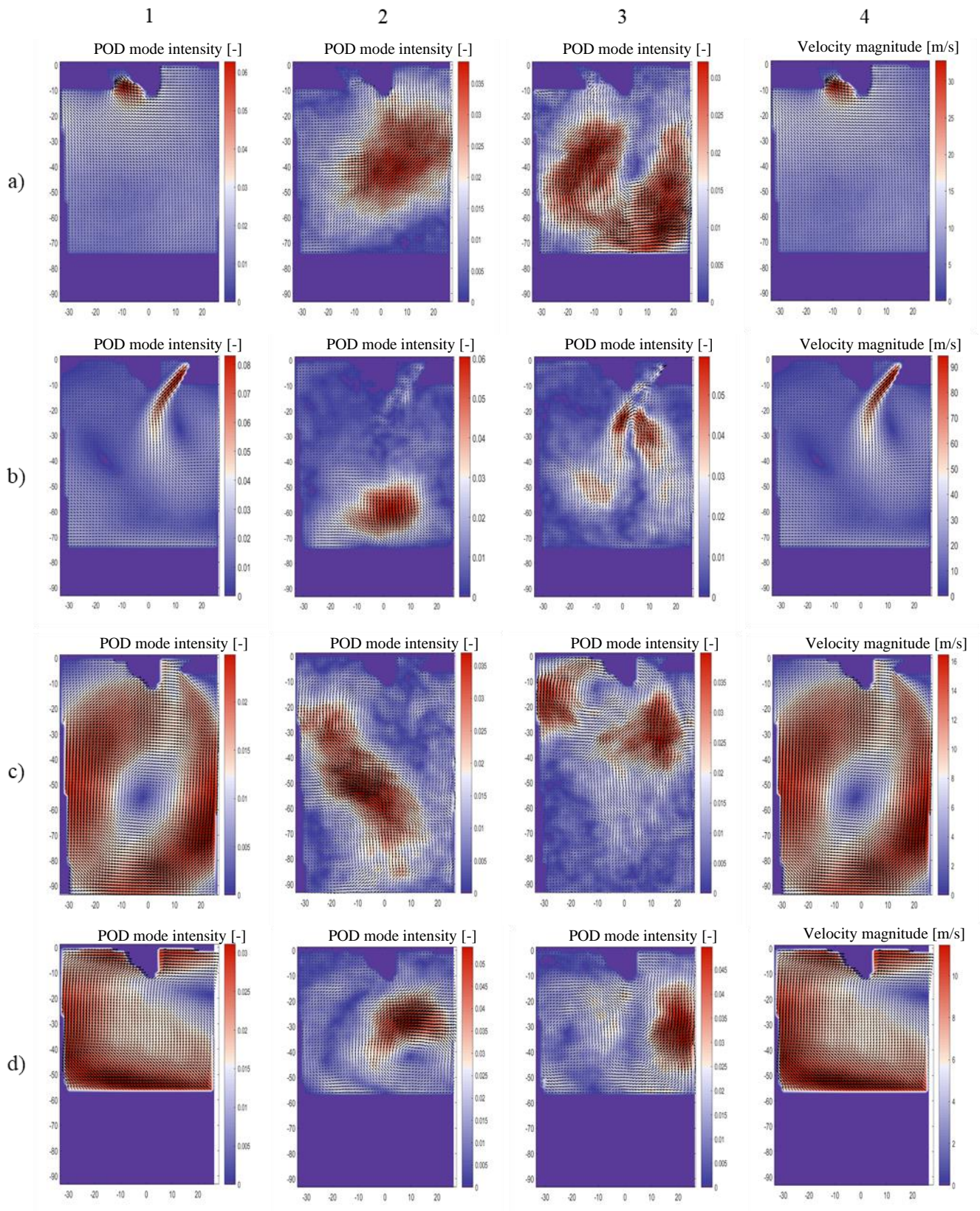


Figure 5 POD Modes: 1) Mode 1, 2) Mode 2, 3) Mode 3, 4) Average Flow Field for CA position a) 240CA, b) 475 CA, c) 540CA, d) 630 CA

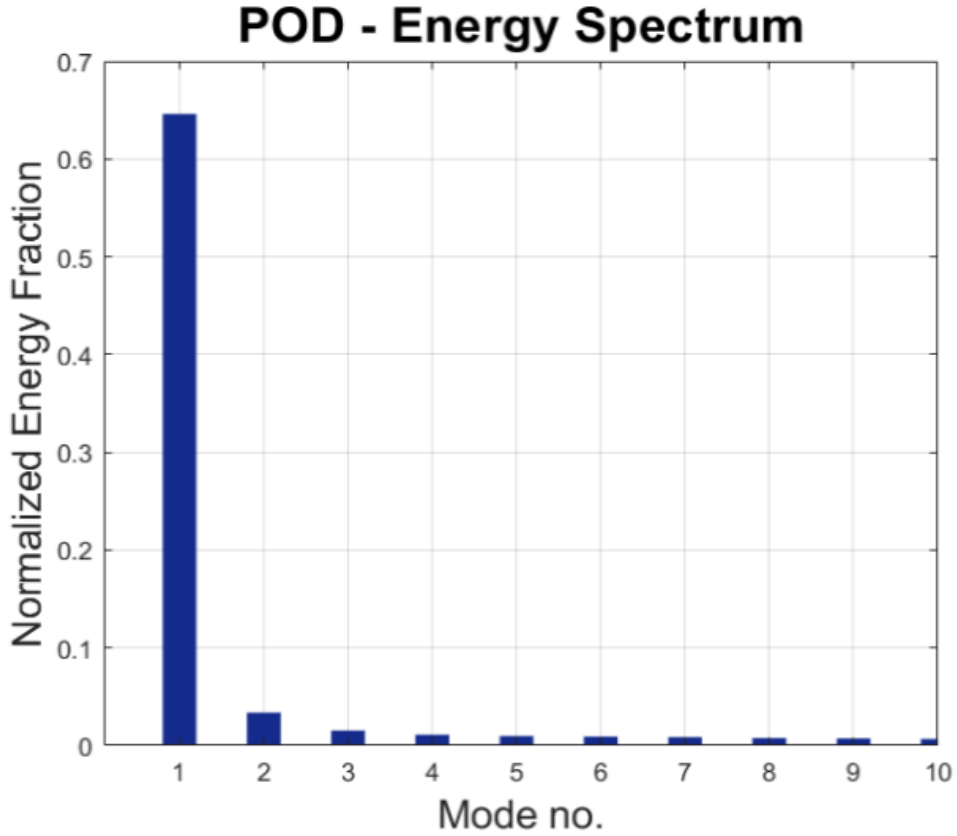


Figure 6 Energy spectrum for the first 10 POD modes for 475 CA position

Focusing on the 475CA position, i.e. mid intake stroke, the POD energy spectrum is reported in Figure 6. A predominance of the first mode can be observed: in this case, most of the energy (64.6%) is associated to the average flow. The second mode has only the 3.37% of the total energy, while the third mode has less than half the energy of the second (1.51%). The energy associated with the remaining modes progressively decreases. While a visual representation of the first POD mode allows to resemble the average flow, no recognizable turbulent structures can be observed in the representation of the second and third mode. However, their importance is highlighted by the Root Mean Square deviation (RMS), shown in Figure 7. The RMS is calculated as:

$$u_{RMS}(CA) = \sqrt{\frac{\sum_{i=1}^N (V_{CA}^i - \bar{V}_{CA})^2}{N}} \quad [3.9]$$

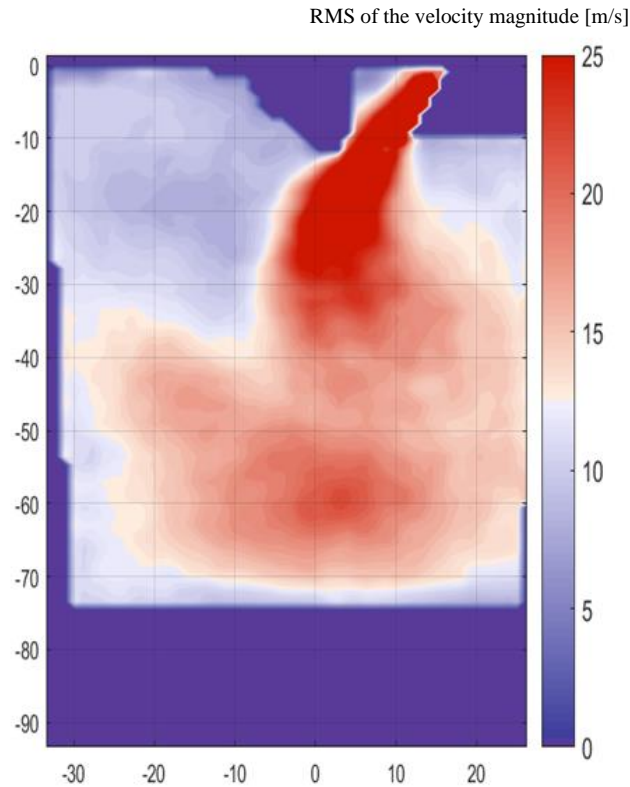


Figure 7 RMS of the flow field at CA position 475

The highest deviations are in the zones identified by modes 2 and 3. This means that the most energetic secondary flow structures are mainly responsible for the deviation around the mean flow field. Therefore, they can be looked as potential candidates for CCV promotion. The contribution to CCV of the remaining modes is certainly not negligible. However, since the energy associated with each mode is progressively lower, it becomes harder to understand each mode's macroscopic effect on CCV. As described in Section 2.2, POD decomposition may be used to group low energy POD modes and to reconstruct coherent and incoherent parts of the flow field turbulence.

Having a set of 240 engine cycles, therefore 240 snapshots, phase invariant POD provides a full set of 240 coefficients for each sample. POD coefficients are directly linked to POD modes and they give useful information on each snapshot. Assuming that the first modes are always the most relevant for general considerations, Figure 8 shows the evolution of the coefficients of the first three modes along the whole engine cycle.

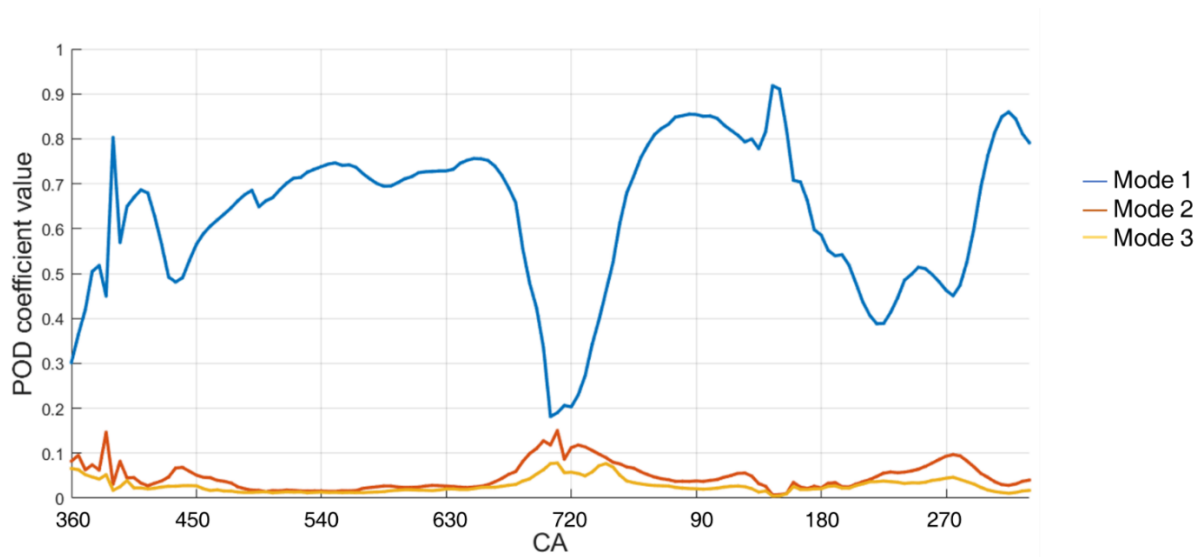


Figure 8 Energy spectrum of the first 3 POD modes along the whole intake phase

The first mode is always the most energetic, its energy fraction ranging from 20% to 90% of the total energy. A high energy associated with the first mode is an indicator of the presence of a dominant turbulent structure. In the specific case of the TCC-III engine, this structure is identified as the tumble motion. Conversely, low values of the first POD mode along the cycle could be associated with the lack of dominant structures. Although this is reasonable and generally true, this purely mathematical results must always be critically analyzed. For example, the lowest peaks in the cycle correspond to TDC positions. Considering the compression TDC, the organized tumble motion is progressively destroyed by the flat shape of the piston and the relatively low flow velocity, thus explaining the low value of the first mode. Nevertheless, looking at the ensemble average flow field, in Figure 9, the cause of the anomaly could be concurrently found in the lack of data in the Field Of View (FOV).

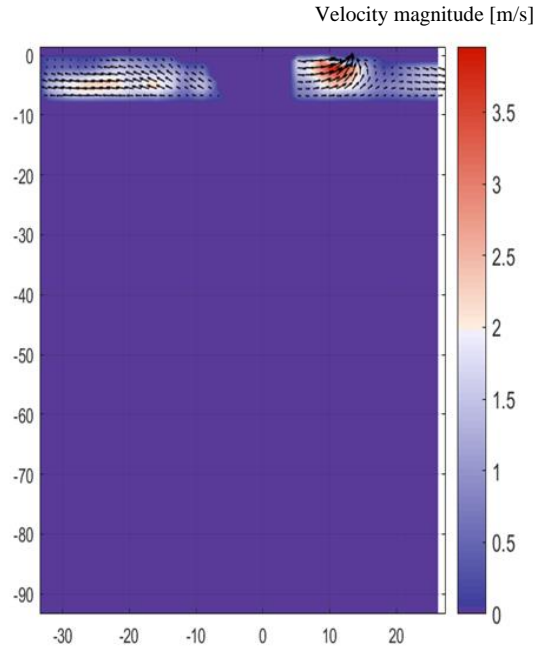


Figure 9 Average flow field for the CA position 360

This affects both the interpretation of the POD outcomes and a possible comparison with CFD data.

3.4 Conditional averaging methodology

The conditional averaging method proposed by Buhl et al. [30] uses POD as a tool to objectively identify cyclic variation in macroscale vortices. As for most comparisons between experimental and calculated values, the calculation of mean values is performed on equal crank angle position, so that the instantaneous flow fields are consistent in terms of geometry and boundaries. The ensemble average is calculated as:

$$\bar{\mathbf{u}}(\mathbf{x}, \phi) = \frac{1}{N} \sum_{n=1}^N \mathbf{u}(\mathbf{x}, \phi, n) \quad [3.10]$$

based on N available flow realizations for the velocity field $\mathbf{u}(\mathbf{x}, \phi, n)$ at a specific crank angle ϕ for each individual cycle n . Even though the ensemble average gives a clear idea on the macroscopic behavior of the flow field, only little information can be extracted by this analysis in terms of large-scale fluctuations, which can be linked to CCV. Instead of calculating the ensemble average on the full set of data, Buhl et al. propose calculating the average on reduced sets of instantaneous flow fields, which are

identical in terms of a conditioning vector ϕ . The conditioning vector must be able to detect the cycle-dependent dynamics of the large-scale structures. This method of conditional averaging is defined according to:

$$\hat{\mathbf{u}}(\Phi) = \frac{1}{M(\Phi)} \sum_{n=1}^{M(\Phi)} (\mathbf{u}(n, \phi) | \phi = \Phi) \quad [3.11]$$

Eq. 3.10 and Eq. 3.11 are very similar, while the value $M(\Phi)$ denotes the number of instantaneous flow fields for which $\phi = \Phi$ is valid. Since the high energetic POD modes are generally associated with large-scale structures, as recalled in Section 1.2, the cycle-dependent coefficients indicate the contribution of each POD mode to that cycle. Consequently, they can be used as a criterion to find the conditioning vector ϕ . It is possible to reduce the conditioning vector to a single conditioning variable, which can be represented by a set of four combinations of POD coefficients. Buhl et al. call these combinations subsets. They are denoted by the simple variable $s(n)$, whereby the dependency of the individual cycle n is not explicitly shown in the following for notational convenience. Furthermore, the conditioning variable s can take the discrete values 1, 2, 3 or 4. Accordingly, the subset-dependent averaged flow field is denoted as $\hat{\mathbf{u}}(s)$. Subsets are defined using the well-established capability of POD to identify the coherent flow structures. Cyclic variations of these flow structures are reflected in a variation of the high-energetic POD coefficients, which become the discriminating factor to cluster cycles into subsets. Figure 10 shows the schematic procedure of Buhl's methodology.

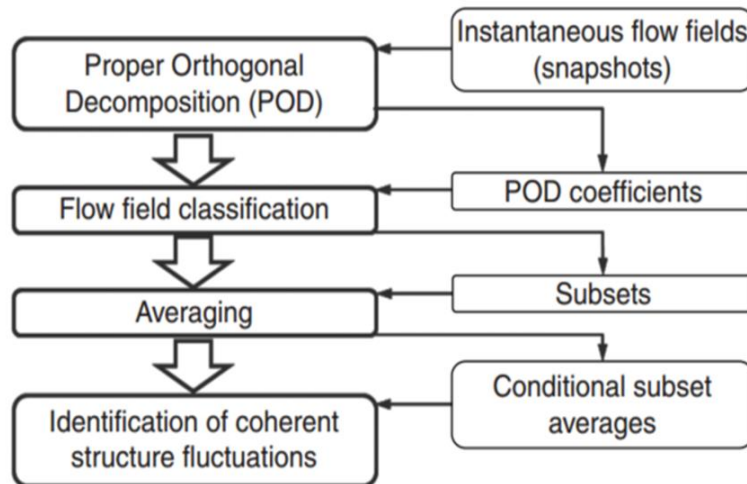


Figure 10 Scheme of the procedure of conditional averaging developed by Buhl et al.[30]

For the analysis of the intake stroke of an engine, Buhl et al. propose the criterion reported in Table 2.

Subset	M2 coefficient	M3 coefficient
1	≥ 0	≥ 0
2	≥ 0	< 0
3	< 0	≥ 0
4	< 0	< 0

Table 2 Criterion for the subset selection table by Buh et al. [30]

Buhl's criterion is hereafter applied for the generation of the subsets. The intake phase is at first analyzed. As stated in Section 2.1, a coefficient for each POD mode is associated with every single sample. In Phase Dependent POD, the samples are the flow fields at a given CA position for each cycle. The POD coefficients define the weight of the flow structure described by each mode in every single sample. As shown in Figure 11 for modes 1, 2 and 3, these POD coefficients are highly variable within the set of available cycles. The POD coefficients related to the first mode show a slight variation around a positive value. POD coefficients of the modes higher than 1 oscillate around zero. The deviation of peaks and troughs decreases for increasing mode number. The higher is the magnitude of the POD coefficient, the higher is the energy associated with the respective POD mode. POD coefficients with negative values are included. This can be deduced from Equation 3.7: the velocity flow field reconstruction is given from the contribution of the POD mode multiplied by the POD coefficient. The energy is given by the square of velocity, therefore it is proportional to the square of POD coefficients. A pictorial view of the different subsets for the 475CA position can be found in Figure 12.

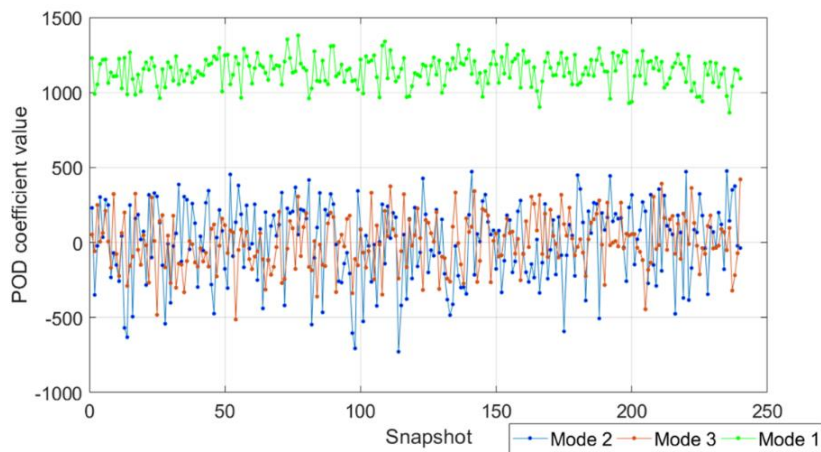


Figure 11 POD coefficients for the modes 1,2 and 3 over the 240 cycles for 475 CA position

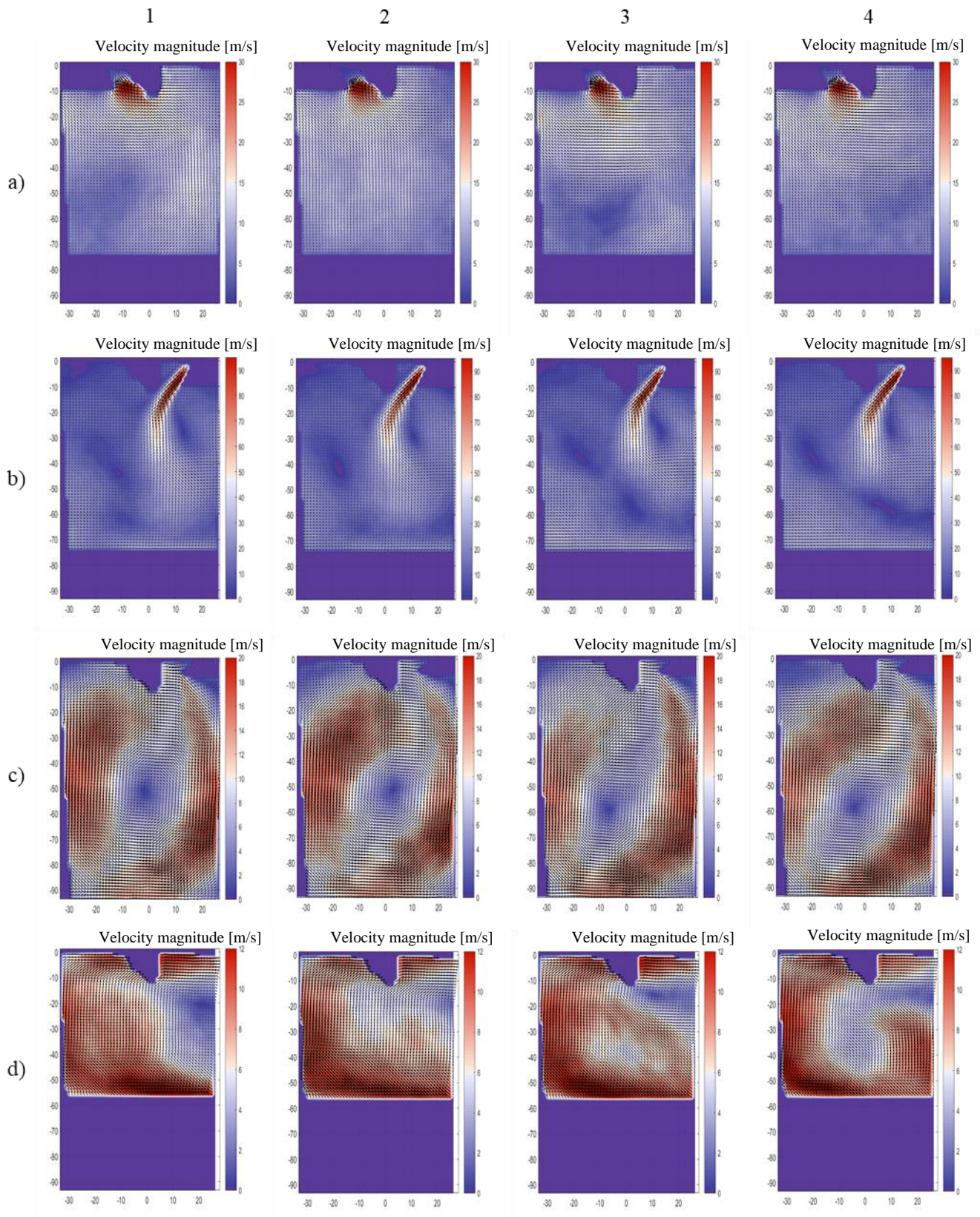


Figure 12 Conditional averaging method: 1) Subset 1, 2) Subset 2, 3) Subset 3, 4) Subset 4 for CA position a) 240CA, b) 475 CA, c) 540CA, d) 630 CA

Subsets 1 and 2 show a higher intake jet penetration, while subsets 3 and 4 show a more tumble-prone jet orientation. Since mode 2 coefficients of subsets 1 and 2 are higher than 0, a higher energy is expected for the pertaining cycles. Such expectation is confirmed by the higher jet penetration.

It is harder to highlight the effects of mode 3 on each subset.

A further step in the subset selection is then performed focusing on one mode at a time, for example Mode 2. Two subsets are now selected, picking up the highest and the lowest coefficients rather than choosing positive and negative ones. The average value of the positive and the negative coefficients are then calculated. Finally, all samples lying on the top 20% and bottom 20% values are included in the two new subsets.

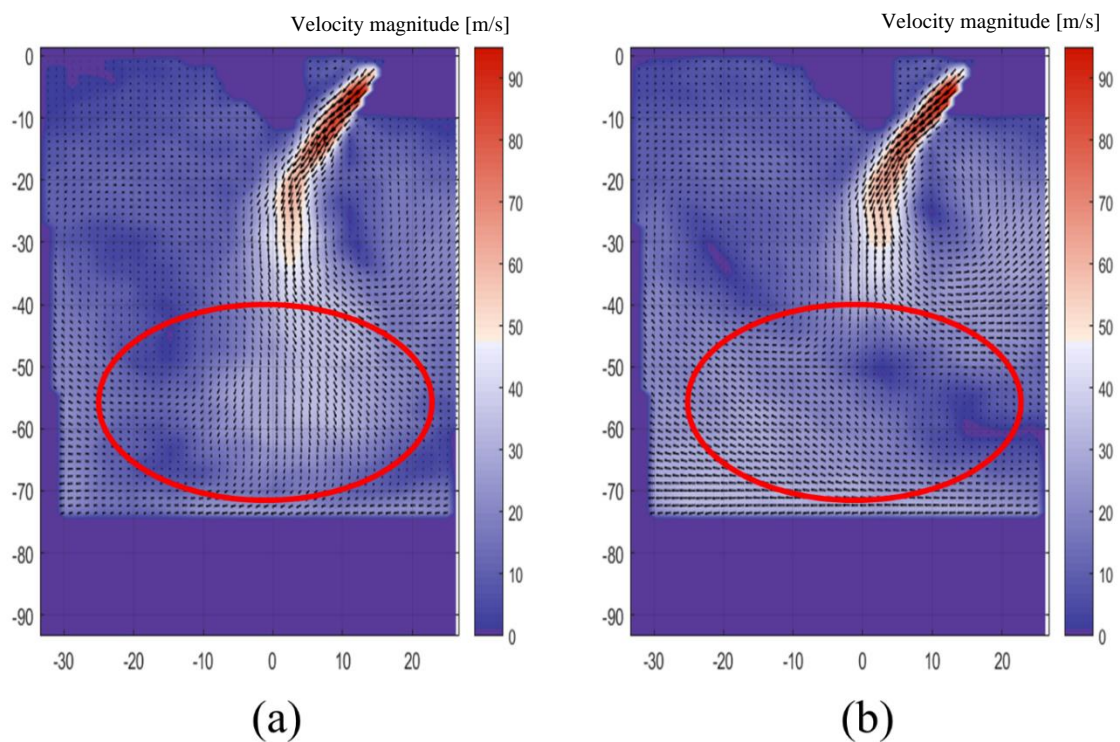


Figure 13 Subsets selected according to the second POD mode criterion. (a) 2 POD mode peaks (b) 2 POD mode troughs. The contribution of the second POD mode is highlighted

Results are reported in Figure 13. As expected, the aforementioned difference between subsets 1 and 2 becomes now even more evident.

This method is useful to emphasize the contribution of the third mode as well.

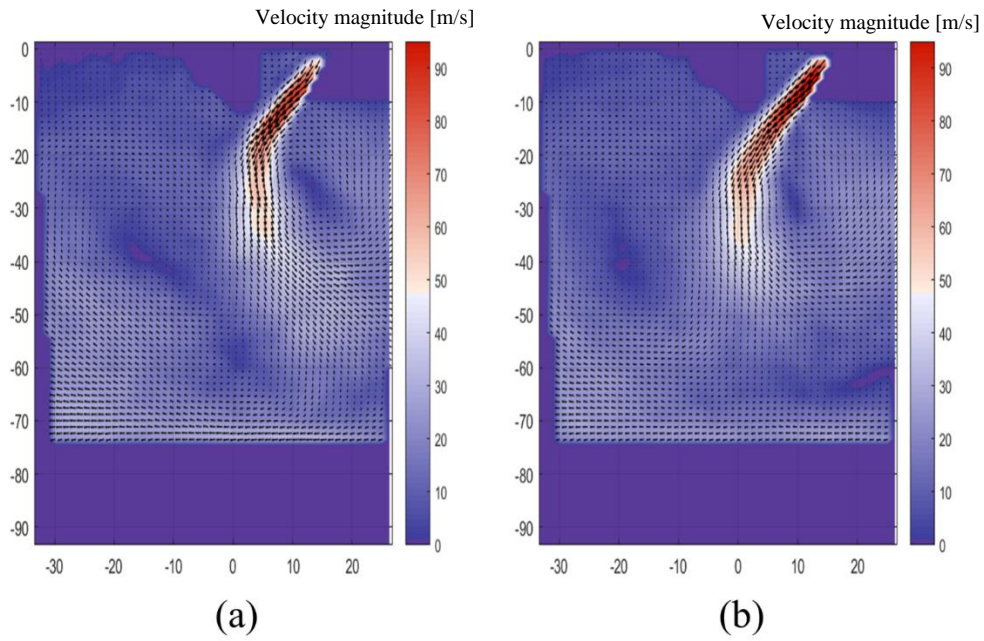


Figure 14 Subsets selected according to the third POD mode criterion. (a) 3 POD mode peaks (b) 3 POD mode troughs.

Figure 14 shows that it is harder to identify a clear correlation between the third mode structure and the variation in the flow fields of the two subsets. However, differences in the jet tendency to generate a recirculation motion are now visible.

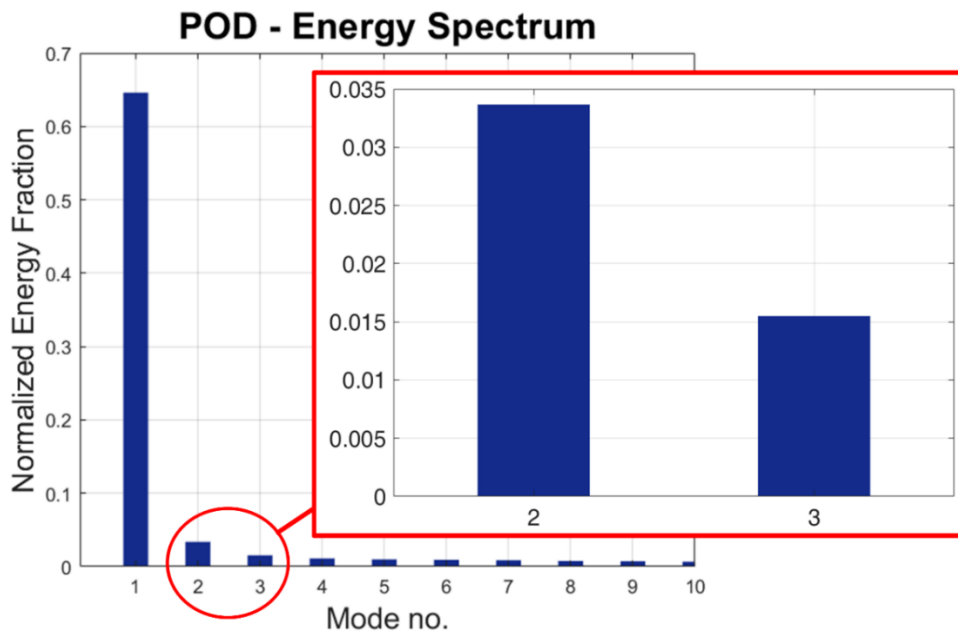


Figure 15 Detail of the energy contribution of the POD modes 2 and 3 at CA position 475

Again, the lower energy content of mode 3 structures, highlighted in Figure 15, is the main reason why it is more difficult to correlate variations in subsets with the third mode structures themselves.

For the sake of completeness, the same method is also applied to the first POD mode. Results are shown in Figure 16.

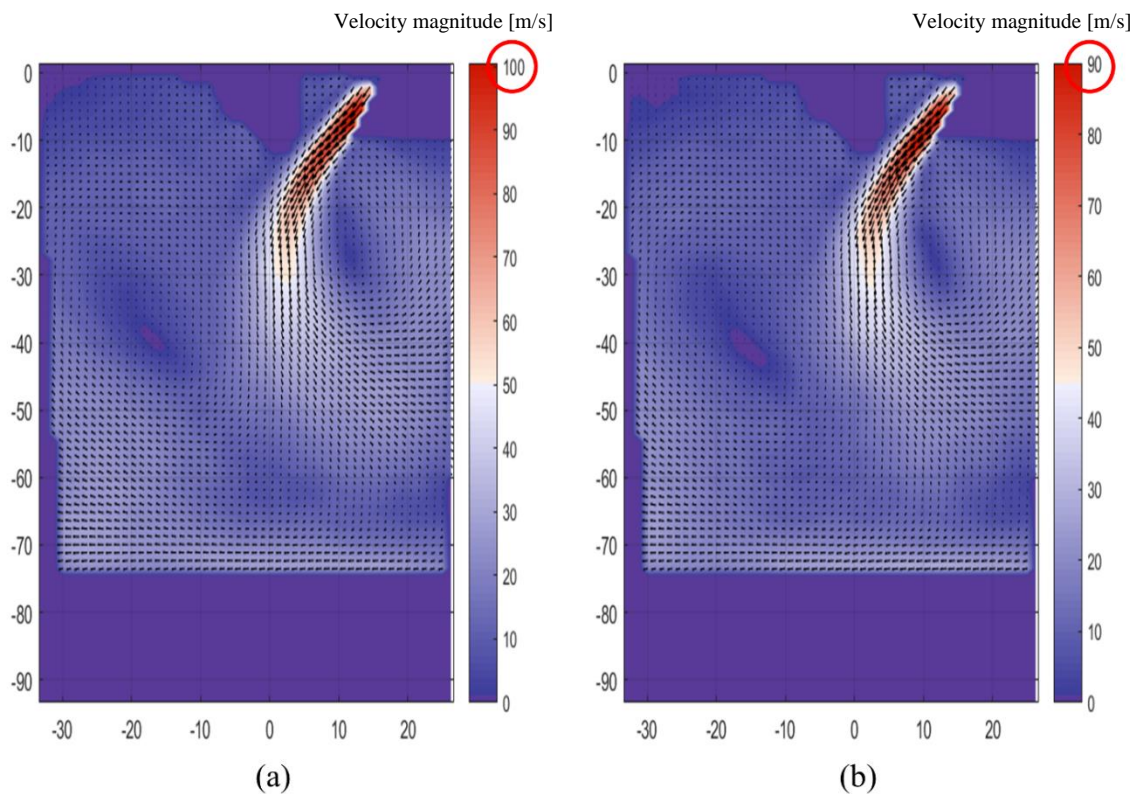


Figure 16 Subsets selected according to the first POD mode criterion. (a) 1 POD mode peaks (b) 1 POD mode troughs. The contribution of the first POD mode is highlighted

As expected by looking at the POD coefficients in Figure 11, no differences in the flow field can be highlighted. There is, however, a difference in the local maximum velocities in the flow field: the peak subset shows higher velocities than the trough one. This result represents a visual representation of the mathematical nature of POD coefficients: high POD coefficients are associated with high energy content.

Selecting just the peaks and troughs is useful for a better understanding and for emphasizing the macroscopic variations between subsets. However, the drawback is that each subset is populated by a lower number of samples. The population of each subset with both the original and the new criterion are

reported in Table 3. If the number of available cycles is high enough, as in the case of PIV measurements on the TCC-III engine under consideration, the statistical value of each subset may not be relevantly affected. One may object that the reduction of the subset population may become critical when applying the method to a reduced number of samples, which may be the case of multi-cycle LES simulations.

SUBSET	245 CA	475 CA	540 CA	630 CA
1	59	67	70	57
2	60	66	54	69
3	66	50	51	59
4	55	57	65	55
High M2	28	29	30	31
Low M2	34	31	34	38
High M3	29	31	33	32
Low M3	36	33	36	32

Table 3 Number of cycles associated with each subset using Buhl criterion and highest/lowest criterion

Considering, for example, a dataset of 50 LES cycles, subsets could consist of less than 10/20 samples. Consequently, the statistical value of each subset could be compromised and the resulting interpretation of the results misleading. Nevertheless, useful information can be obtained even when applying the method to low-populated subsets. As a demonstration, Figure 17 compares the four different subsets generated with the whole 240 cycles to those resulting from a selection of 50 experimental cycles. Differences between the two groups of subsets appear negligible.

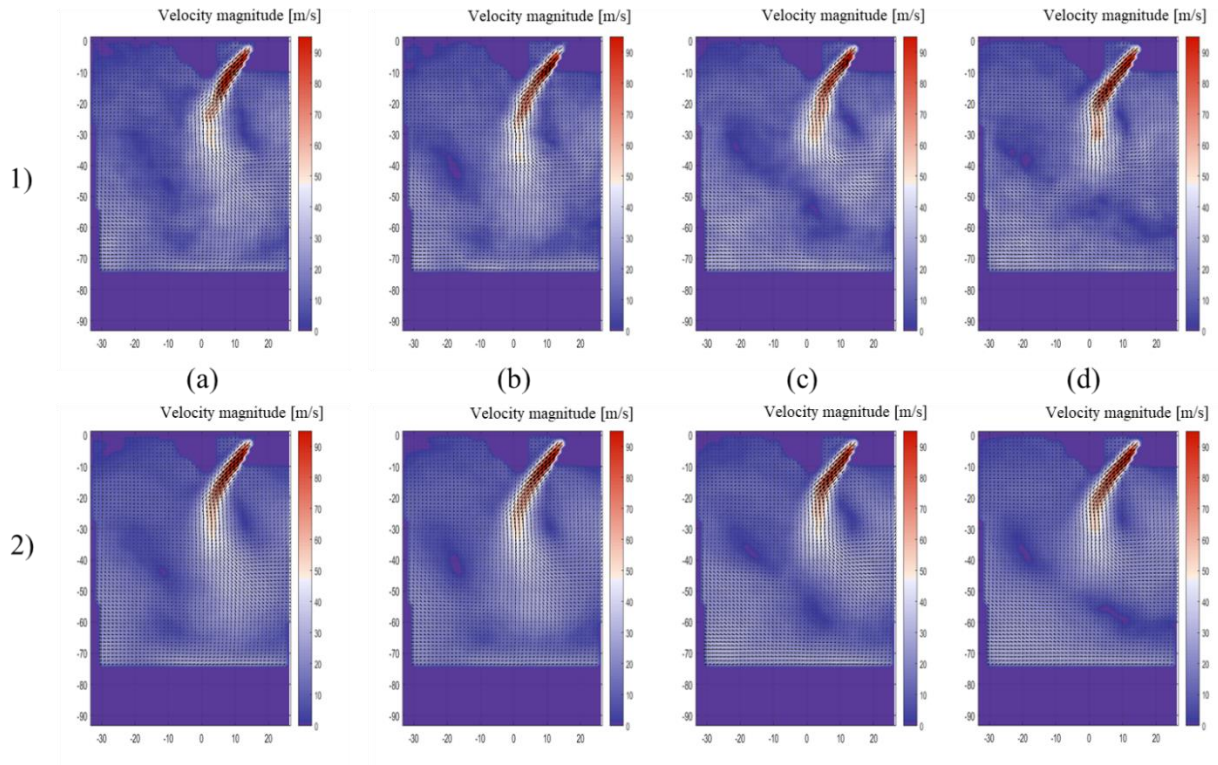


Figure 17 Comparison between conditional averaging method applied to 1) a set of 50 (1th to 50th) cycles among the whole 240 and 2) the whole 240 cycles. a) Subset 1, b) Subset 2, c) Subset 3 and d) Subset 4

Although the method shows the most substantial and meaningful results during the intake phase, its application to other crank angles along the whole cycle confirms its capability to qualitatively describe the CCV, as shown in Figure 12.

3.5 POD Triple Decomposition

Unsteady turbulent flows involve many degrees of freedom and a wide range of time and space scales. Usually, the ensemble average method is applied to separate a mean field part from a fluctuating contribution. Statistical information about the in-cylinder flow field can be obtained from the mean field, while the fluctuating part can provide overall information about CCV. To obtain more information, the fluctuating part can be furtherly decomposed. POD decomposition uses the ability of POD to provide a low-dimensional approximate description of high-dimensional processes to perform a deeper analysis of the fluctuating part. POD triple decomposition, proposed by Roudnitzky et al. [56], aims at decomposing the turbulent flow into three parts: the time-averaged mean part, the coherent part, and the incoherent part. The coherent part is described as a low-frequency contribution around the mean one, while the incoherent part is responsible for turbulent high-frequency perturbations.

The formulation of the POD filtering methodology is recalled.

The instantaneous flow field $u_i(X, t)$ (X and t are the space and time variables, respectively), is defined as:

$$u_i(X, t) = \langle U_i(X) \rangle + \tilde{u}_i(X, t) \quad [3.12]$$

With

$$\tilde{u}_i(X, t) = \hat{u}_i(X, t) + u'_i(X, t) \quad [3.13]$$

Where $\langle U_i \rangle$ is the mean cycle average part, \tilde{u}_i is the fluctuating velocity part, which is decomposed into a coherent part, \hat{u}_i , and an incoherent part, u'_i .

After performing a POD on the full N_{tot} available data, N_{tot} modes are obtained. The first step consists in separating the mean flow and the fluctuating velocity field.

$$\langle U_i(X, t) \rangle = \sum_{n=1}^M a^{(n)}(t) \phi_i^{(n)}(X) \quad [3.14]$$

$$\tilde{u}_i(X, t) = \sum_{n=M+1}^{N_{tot}} a^{(n)}(t) \phi_i^{(n)}(X) \quad [3.15]$$

where M is the number of the POD mode separating the mean flow from the fluctuating part.

The second step is the determination of the POD number N separating the contribution of both coherent and incoherent turbulent velocity fields. Each part of the instantaneous velocity field can then be reconstructed from Eq. 3.16 and Eq. 3.17 respectively:

$$\hat{u}_i(X, t) = \sum_{n=M+1}^N a^{(n)}(t) \phi_i^{(n)}(X) \quad [3.16]$$

$$u'_i(X, t) = \sum_{n=N+1}^{N_{tot}} a^{(n)}(t) \phi_i^{(n)}(X) \quad [3.17]$$

The main difficulty relies on the determination of the cutoff numbers, especially the number N .

To determine the cutoff number N , Roudnitzky et al. suggest in [56] to analyze the POD coefficients associated with the most energetic modes along the cycle. In particular, they find a high repeatability in the POD coefficients of the first 3 POD modes, as shown in Figure 18.

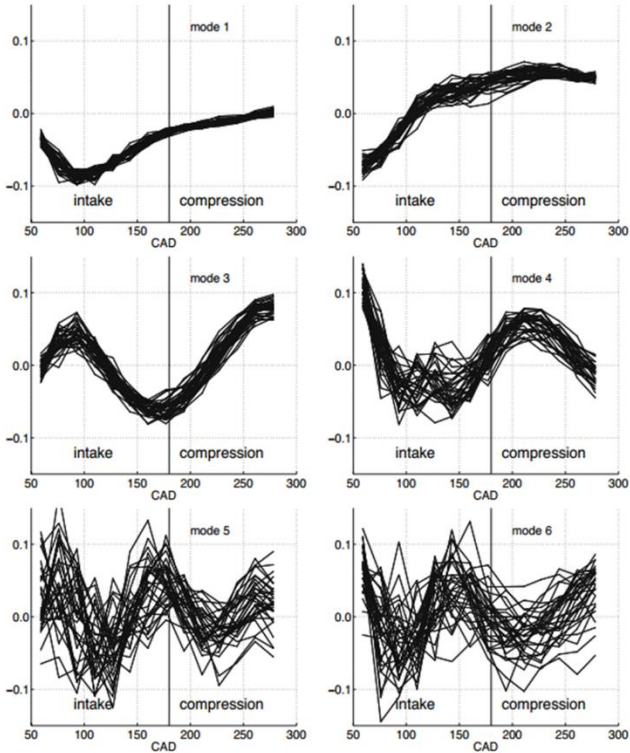


Figure 18 POD coefficient for the first 6 modes on the intake and compression stroke from Roudnitzky [56]

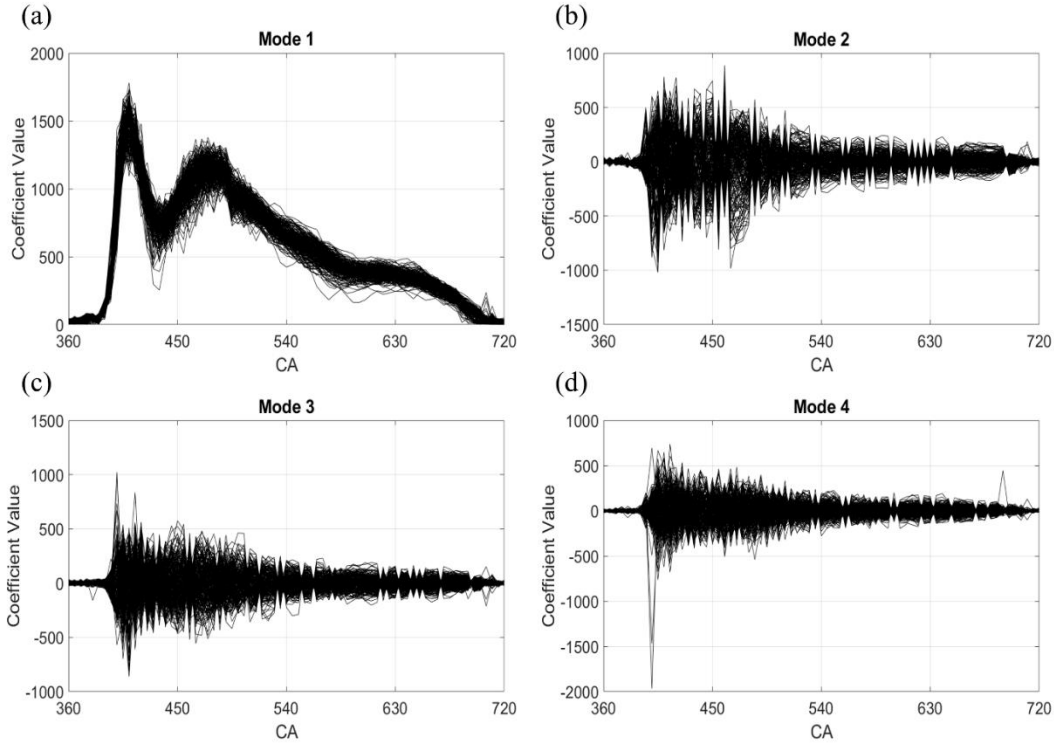


Figure 19 POD coefficient for the first 4 modes for CA position 475 on the intake and compression stroke

Given such evidence, they fix the M value to 3, despite the general agreement in the literature that the first POD mode is sufficient to represent the mean flow field. Since the repeatability of the coefficients is an objective and effective method to determine the POD modes associated with the average flow, this criterion is here applied to the TCC-III dataset. Results are shown in Figure 19. In agreement with the literature, just the first POD mode seems to be sufficient to represent the average flow field.

For a better understanding of the physical meaning of the flow field's mean part, calculated as in Eq. 3.14, it is important to note that the mean part is different from the average flow field, despite looking very similar. The mean part reconstructed from each cycle is time dependent, therefore the POD coefficient is relative to a specific time (in our case, the specific cycle). The POD coefficients of the mean part of the turbulence show repeatability in terms of pattern. However, the intensity of the coefficient relative to each cycle is an indicator of the energy associated with the mean flow motion for the corresponding cycle.

Roudnitzky et al. state that it is difficult to define an objective criterion to identify the cutoff number between coherent and incoherent turbulence. The method proposed by Roudnitzky et al. is based on the assumption that homogeneous isotropic turbulent flows follow Gaussian properties. The individuation of the cutoff number is then performed, analyzing the skewness S and flatness T coefficients on the velocity fluctuation u'_i , defined as:

$$S_{u_i'}(t^{k_d}) = \frac{\langle u_i'^3 \rangle}{\langle u_i'^2 \rangle^{\frac{3}{2}}} \quad [3.18]$$

$$T_{u_i'}(t^{k_d}) = \frac{\langle u_i'^2 \rangle}{\langle u_i'^2 \rangle^2} \quad [3.19]$$

The flatness coefficient T is known as the kurtosis coefficient. Although these coefficients are well known quantities, a brief review of their physical meaning is given here. The skewness is the third standardized central moment of a distribution. If the value of skewness is positive, then the distribution is skewed to the right, and the tails of the distribution are heavier on the right [73]. In this application, a value equal to 0 is expected while approaching the incoherent turbulence, since the distribution of fluctuations is symmetrical around a mean value. The flatness T , called kurtosis, is a measure of the tailedness of the probability distribution of a real-valued random variable [74]. It is a descriptor of the shape of a probability distribution. The kurtosis of a normal distribution is 3. Kurtosis values other than 3 are indicators for a distribution different from the standard one. For example, if the value is higher than 3 the distribution is called leptokurtic. In Figure 20, some examples of leptokurtic distributions are reported.

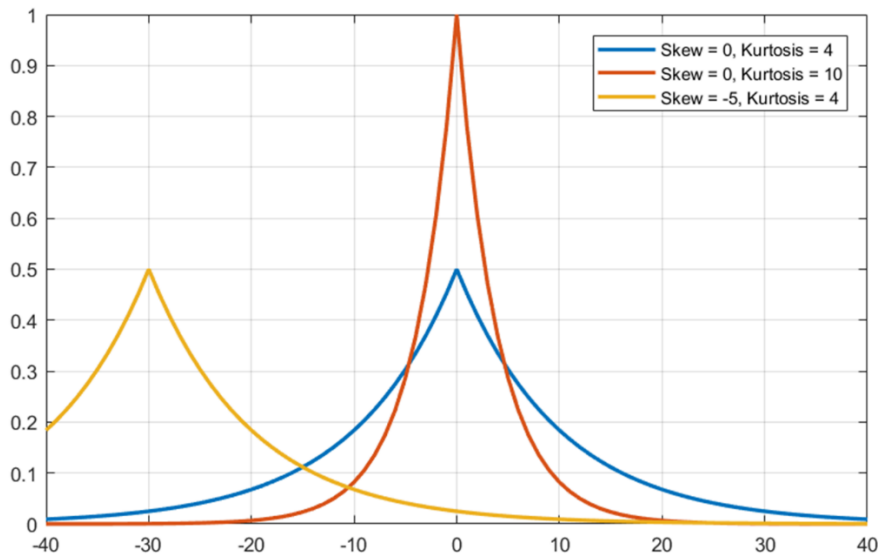


Figure 20 Examples of leptokurtic distributions

On the assumption of Gaussian distribution, the expected Kurtosis number is 3.

These coefficients are spatially averaged:

$$\overline{S_{u'_i}} = \sum_{k=1}^{n_x} \sum_{j=1}^{n_y} S_{u'_i}(x_k, y_j) / (n_x \times n_y) \quad [3.20]$$

$$\overline{T_{u'_i}} = \sum_{k=1}^{n_x} \sum_{j=1}^{n_y} T_{u'_i}(x_k, y_j) / (n_x \times n_y) \quad [3.21]$$

The method proposed by Roudnitzky et al. is applied to the analyzed dataset. Resulting skewness and flatness coefficients for the 475CA in two consecutive snapshots are shown in Figure 21 (a) and (b), while RMS values for skewness and flatness are shown in Figure 21 (c) and (d).

While the skewness coefficient quickly approaches zero, meaning that the distribution of velocities is symmetrical around a mean value, the flatness coefficient does not stabilize around a value of 3.

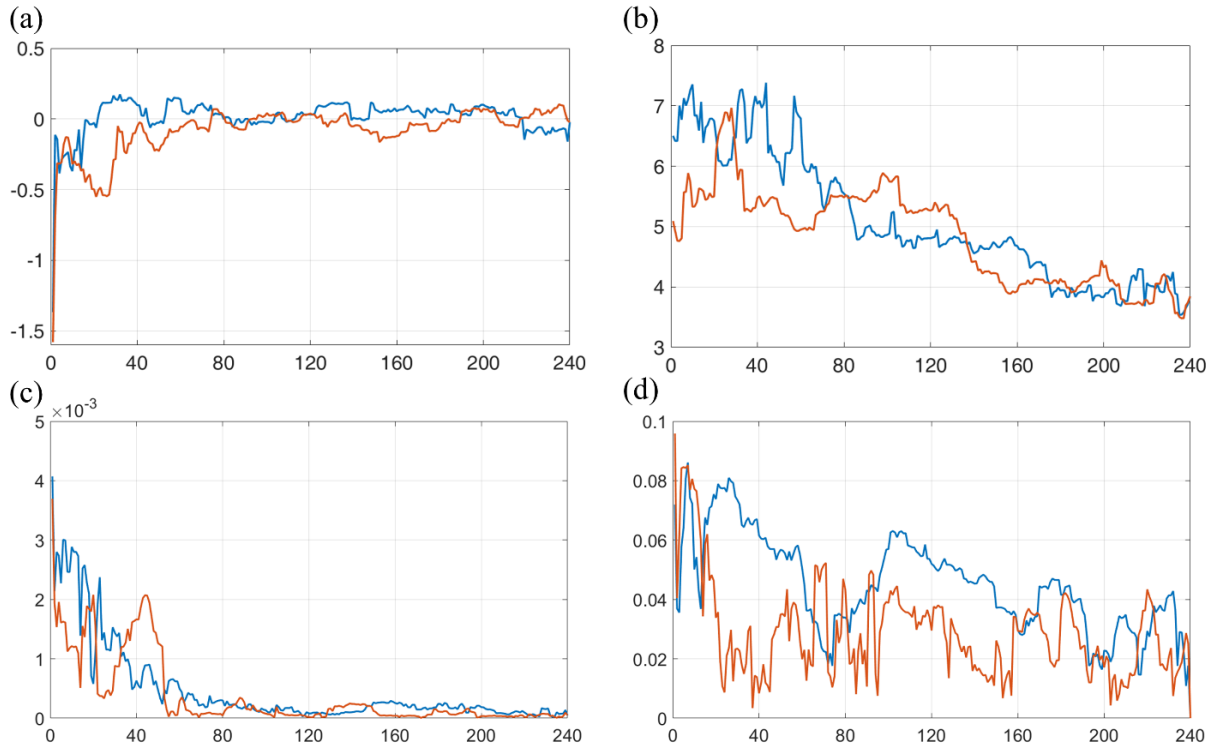


Figure 21 For CA positions 475 on two consecutive snapshots for all the 240 POD modes (a) Skewness coefficients (b) Flatness coefficients (Kurtosis) (c) RMS of Skewness coefficients (d) RMS of Flatness coefficients

For a better understanding of the meaning of the coefficients, the velocity distributions are shown in Figure 22. In Figure 22 (a) the distribution of the cutoff number 1 is shown. As expected, being representative of the mean flow, the distribution is not centered around any mean value. Figure 22 (b)

reports the velocity distribution of 475CA for cutoff number 160, with skewness around 0 and flatness around 4. The distribution is averaged around 0, but slightly leptokurtic.

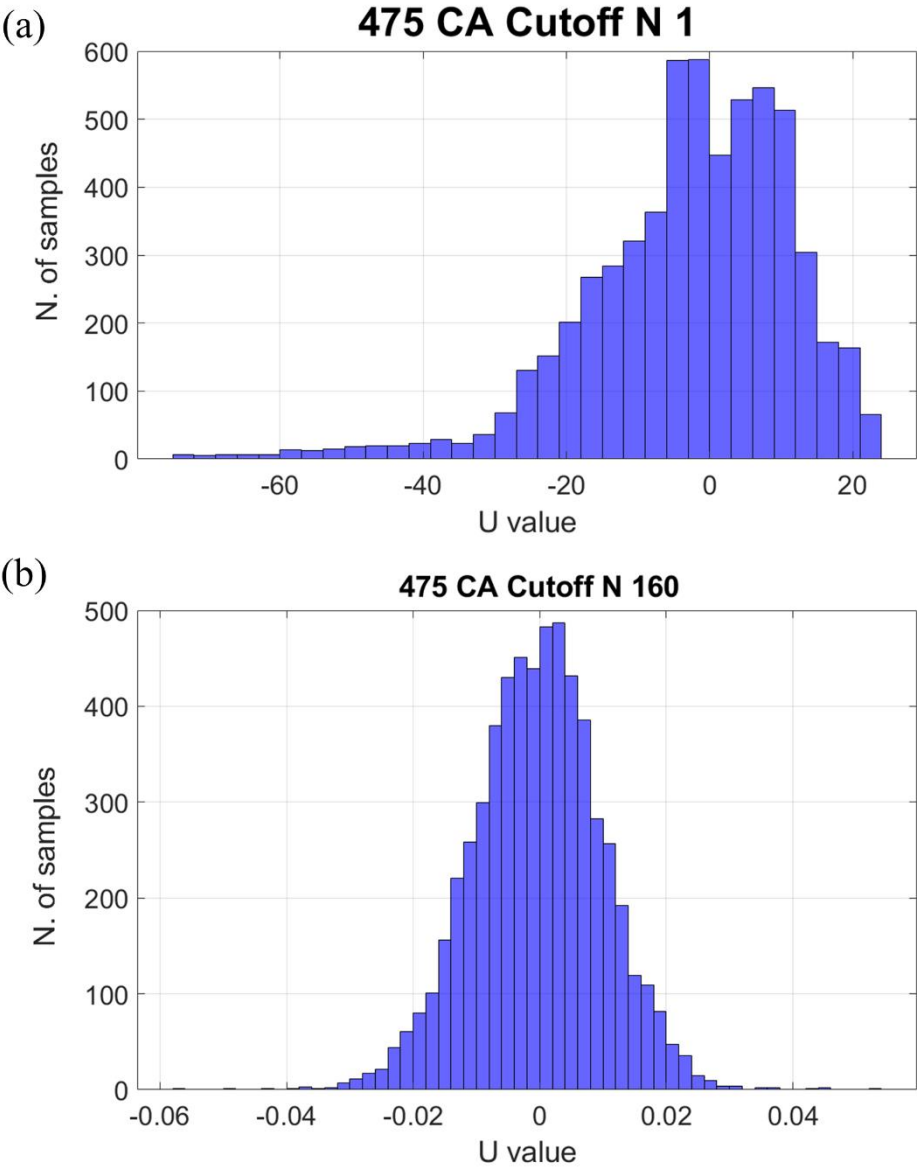


Figure 22 Velocity distributions for reconstructed flow from (a) POD mode 1 and (b) POD mode 160

Roudnitzky suggests, as a method to select the cutoff number, the convergence of skewness and flatness coefficients to 0 and 3, respectively. Results for 245 CA, 475CA, 540CA and 630CA are reported in Figure 23.

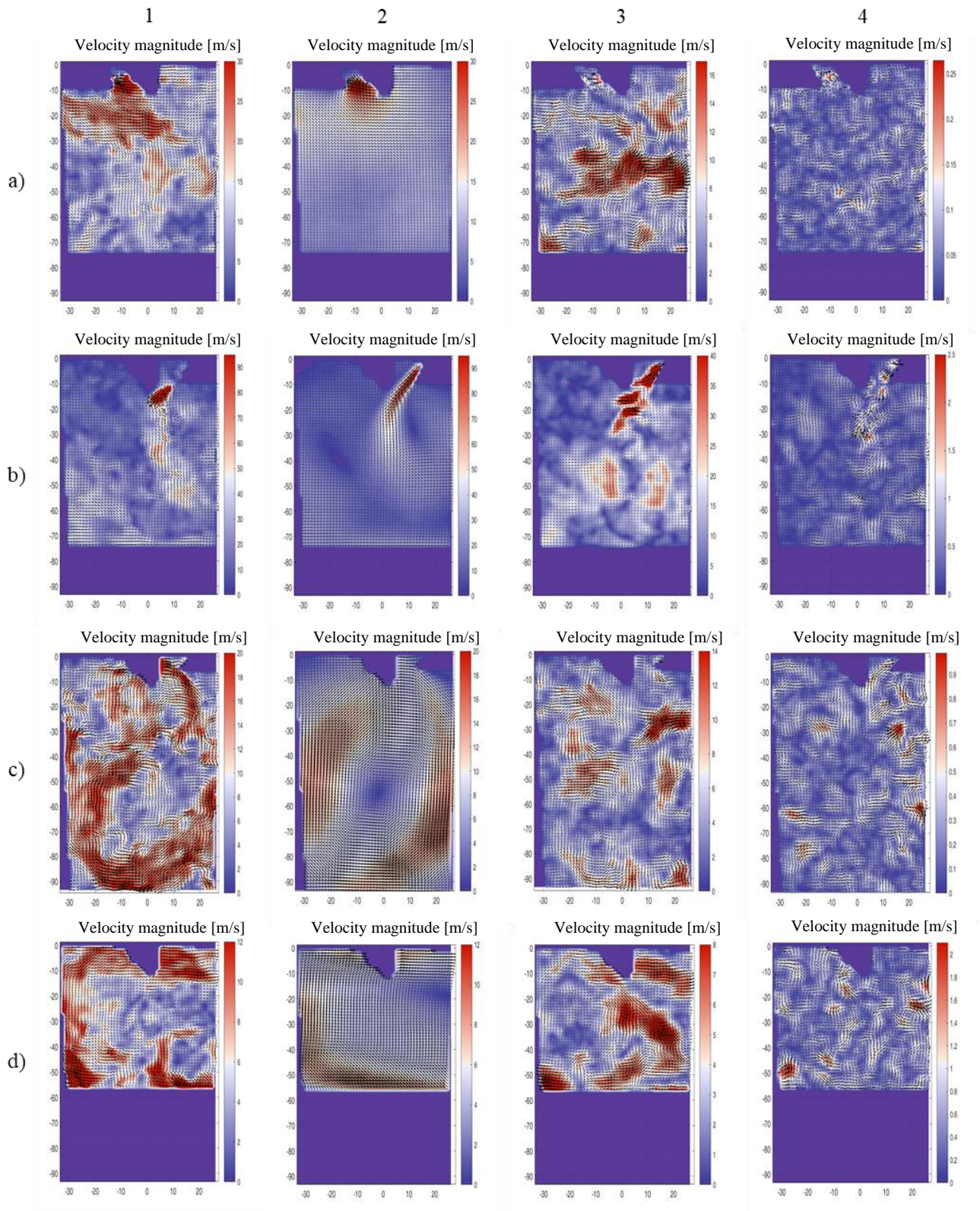


Figure 23 POD triple decomposition for CA position (a) 245, (b) 475, (c) 540, (d) 630, (1) Instantaneous flow field, (2) Mean flow field, (3) Coherent flow field, (4) Incoherent flow field

As visible in Figure 21 (a) and (c), a convergence for the skewness coefficient can be detected. It is harder to objectively define a convergence for the flatness coefficient, as shown in Figure 21 (b) and (d). Figure 24 shows two different choices for the 475 CA cutoff numbers. The difference is on the convergence criterion applied to both skewness and flatness. The difficulty in determining an objective cutoff number has an impact on the analysis. The differences in incoherent turbulent fields in Figure 24 (b) and (d) are not negligible. The incoherent field in Figure 24 (d) seems to better represent the incoherent background turbulence, but no objective method can be identified to demonstrate it.

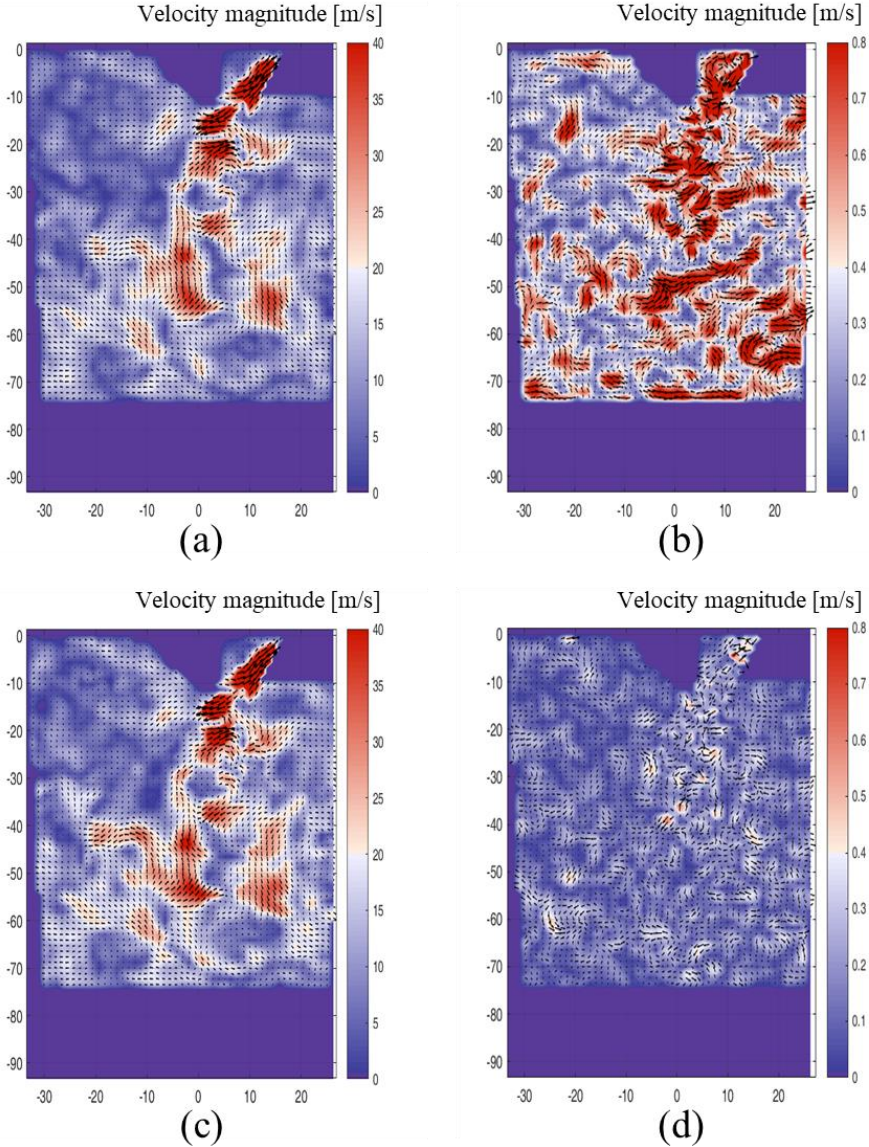


Figure 24 Coherent and Incoherent reconstructed flow fields from two different criteria of convergence

In the opinion of the author, such lack of objectiveness is the most critical aspect of this method. Roudnitzky et al. suggest calculating RMS of the coefficients on the coherent and incoherent part for

the analysis of the cyclic variations along the whole cycle. However, the RMS calculated on the two different incoherent fields leads to different results. To perform the analysis, arbitrary assumptions on the convergence criterion of the flatness coefficient must then be introduced.

3.6 POD Quadruple Decomposition

Similarly to the triple POD decomposition, the quadruple one proposed by Qin et al. is based on the idea that the turbulent flow field can be decomposed in separated classes. The number of such classes is now four:

$$\begin{aligned} u(x, t) &= u^{mean}(x, t) + u^{fluctuation}(x, t) \\ &= u^{mean}(x, t) + u^{coherent}(x, t) + u^{transition}(x, t) + u^{turbulent}(x, t) \end{aligned} \quad [3.22]$$

where, as already reported in Section 3.2, u^{mean} represents the mean flow motion and contains most of the kinetic energy of the flow field. As shown in Eq. 3.23-3.26, the definition of each part of the decomposed flow field is analogous to the triple decomposition. Therefore, the same considerations made in Section 3.6 apply for the mean flow field.

$$u^{mean}(X, t) = \sum_{n=1}^M a^{(n)}(t) \phi_i^{(n)}(X) \quad [3.23]$$

$$u^{coherent}(X, t) = \sum_{n=M+1}^C a^{(n)}(t) \phi_i^{(n)}(X) \quad [3.24]$$

$$u^{transition}(X, t) = \sum_{n=C+1}^{Tr} a^{(n)}(t) \phi_i^{(n)}(X) \quad [3.25]$$

$$u^{turbulent}(X, t) = \sum_{n=Tr+1}^N a^{(n)}(t) \phi_i^{(n)}(X) \quad [3.26]$$

The coherent part $u^{coherent}$ contains the large-scale vortices and plays a critical role in the cycle-to-cycle variations. The transition part is identified as a passage in the energy cascade between the large-

scale vortices in the coherent turbulence and the smallest ones in the incoherent background turbulence. $u^{turbulent}$ represents the small-scale structures in the flow field, which are homogeneous and isotropic.

As in the triple decomposition, the difficulty is to detect the cutoff modes to objectively identify each part of the turbulent flow field. The method proposed by Qin et al. is based on the definition of correlation coefficients among the reconstructed flow fields.

$$R = \overline{R(u(k_1, k_2, cycle_i), u(k_3, k_4, cycle_j))} \\ = \left(\frac{u^{(k_1, k_2)}(x, t, cycle_i) \cdot u^{(k_3, k_4)}(x, t, cycle_j)}{|u^{(k_1, k_2)}(x, t, cycle_i)| \cdot |u^{(k_3, k_4)}(x, t, cycle_j)|} \right) \quad [3.27]$$

where $u^{(k_1, k_2)}(x, t, cycle_i)$ denotes the reconstructed velocity field of the i^{th} cycle using POD modes from number k_1 to number k_2 :

$$u^{(k_1, k_2)}(x, t) = \sum_{n=k_1}^{k_2} a^{(n)}(t) \phi_i^{(n)}(X) \quad [3.28]$$

To recognize the mean part, Qin et al. calculate the correlation coefficient among different cycles. A value of the correlation coefficient close to 1 represents a close relationship between two different modes.

$$R_1 = \overline{R((k_1, N, cycle_i), (k_1, N, cycle_j))} \quad [3.29]$$

k_1 coefficient is maintained constant between the two cycles and it changes from 1 to N. Neglecting the first mode in the flow reconstruction implies a drop in the correlation coefficient, meaning that the first POD mode, as expected, is again a reasonable representation of the mean flow. This is shown in Figure 21.

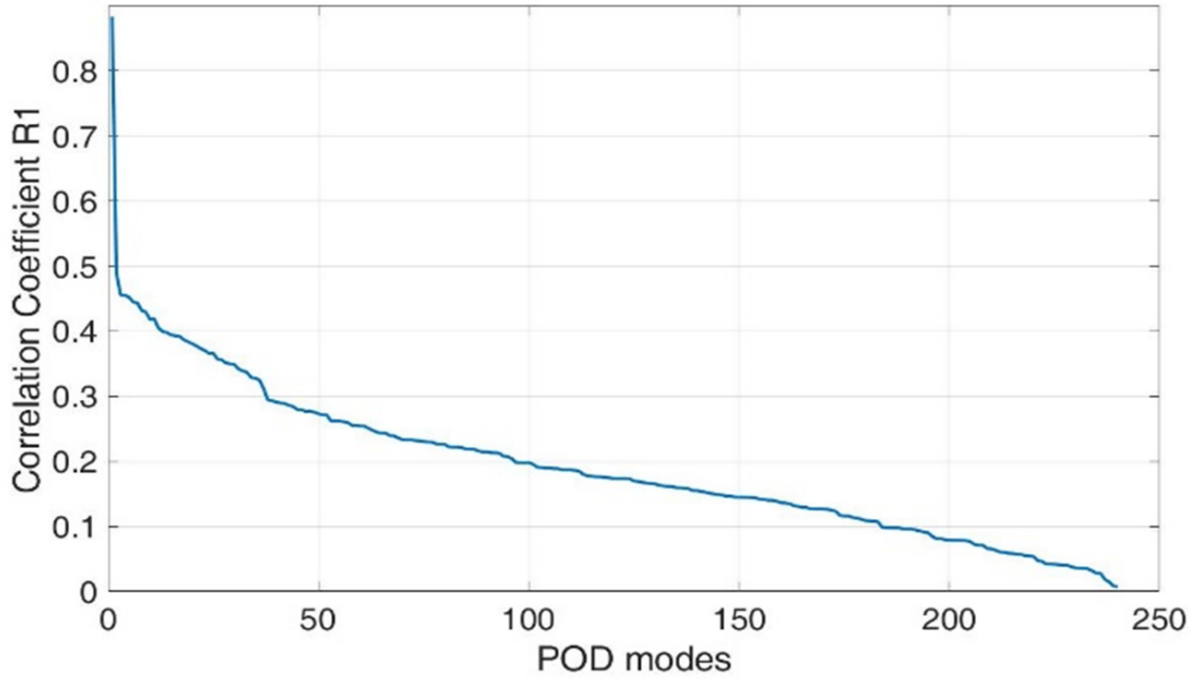


Figure 25 Correlation coefficient R_1 for the definition of the mean part

For the coherent and the turbulent parts, the reconstruction process is performed separately moving both in the forward and backward direction. The forward direction starts from $M+1$, while the backward direction starts from $N-1$.

$$R_2 = \overline{R((M+1, k_2, cycle_i), (M+1, k_2+1, cycle_j))} \quad [3.30]$$

$$R_3 = \overline{R((k_1, N, cycle_i), (k_1-1, N, cycle_j))} \quad [3.31]$$

The average of the correlation coefficients for 475CA is reported in Figure 26.

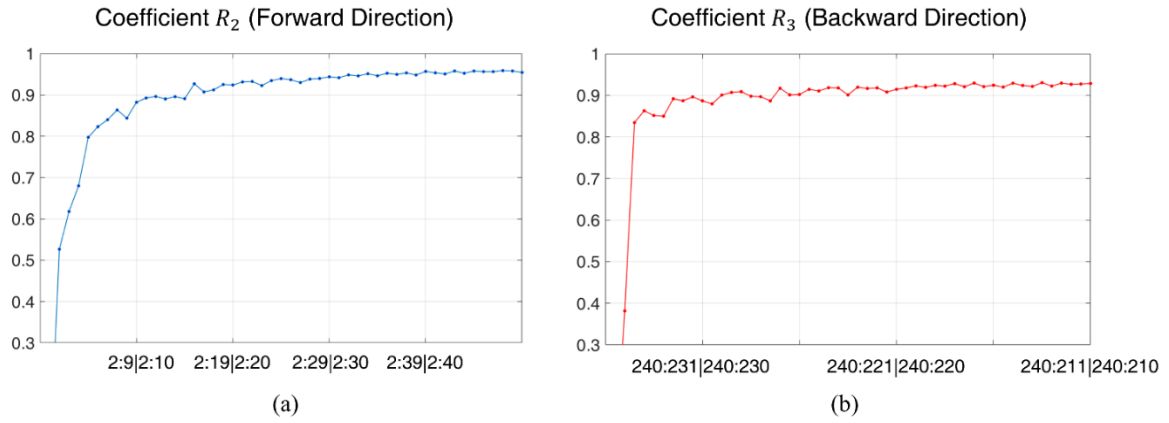


Figure 26 Correlation coefficients R_2 (a) and R_3 (b) for CA position 475

Qin et al. consider 95% as the threshold to define the cutoff number. Wang uses a slope of the relevance index lower than 0.1 [75]. If the addition of a POD mode to the flow reconstruction does not modify significantly the resulting field, i.e. until the correlation coefficient is close to 1, the energetic contribution of that POD mode is negligible. Therefore, the cutoff number can be identified for the coherent part of the turbulence. The same considerations cannot be used for the backward direction. A threshold equal to 95% is never reached, regardless the choice of the starting mode.

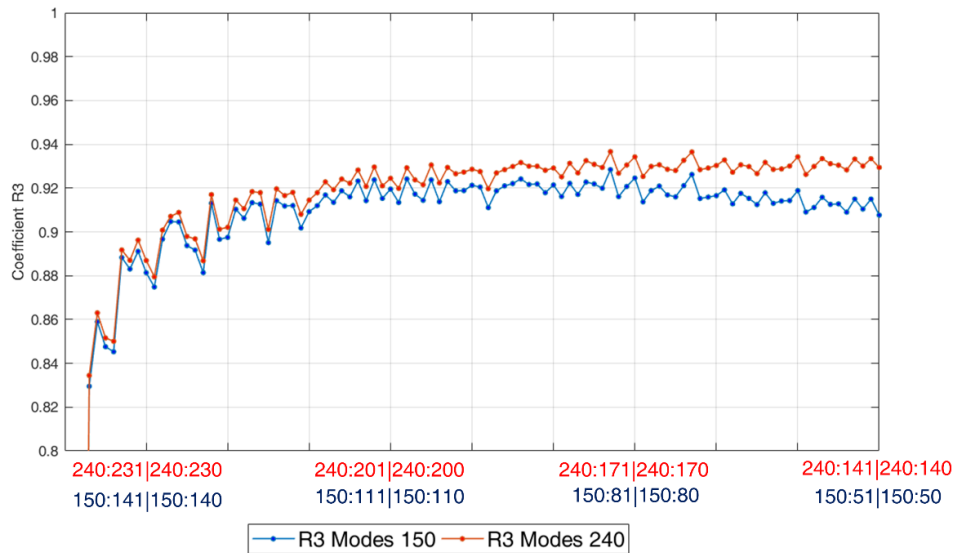


Figure 27 Correlation coefficient R_3 obtained backward from mode 240 and from mode 150

Figure 27 shows the evolution of the correlation coefficients for two starting modes, namely mode 240 and mode 150. The trends are very similar in shape and both do not reach the threshold of 95%. This

seems to suggest that the choice of 95% as a threshold is not an a priori indicator for the identification of the homogeneous incoherent flow field and the use of correlation coefficients can be misleading. Results of the application of the method are shown in Figure 28.

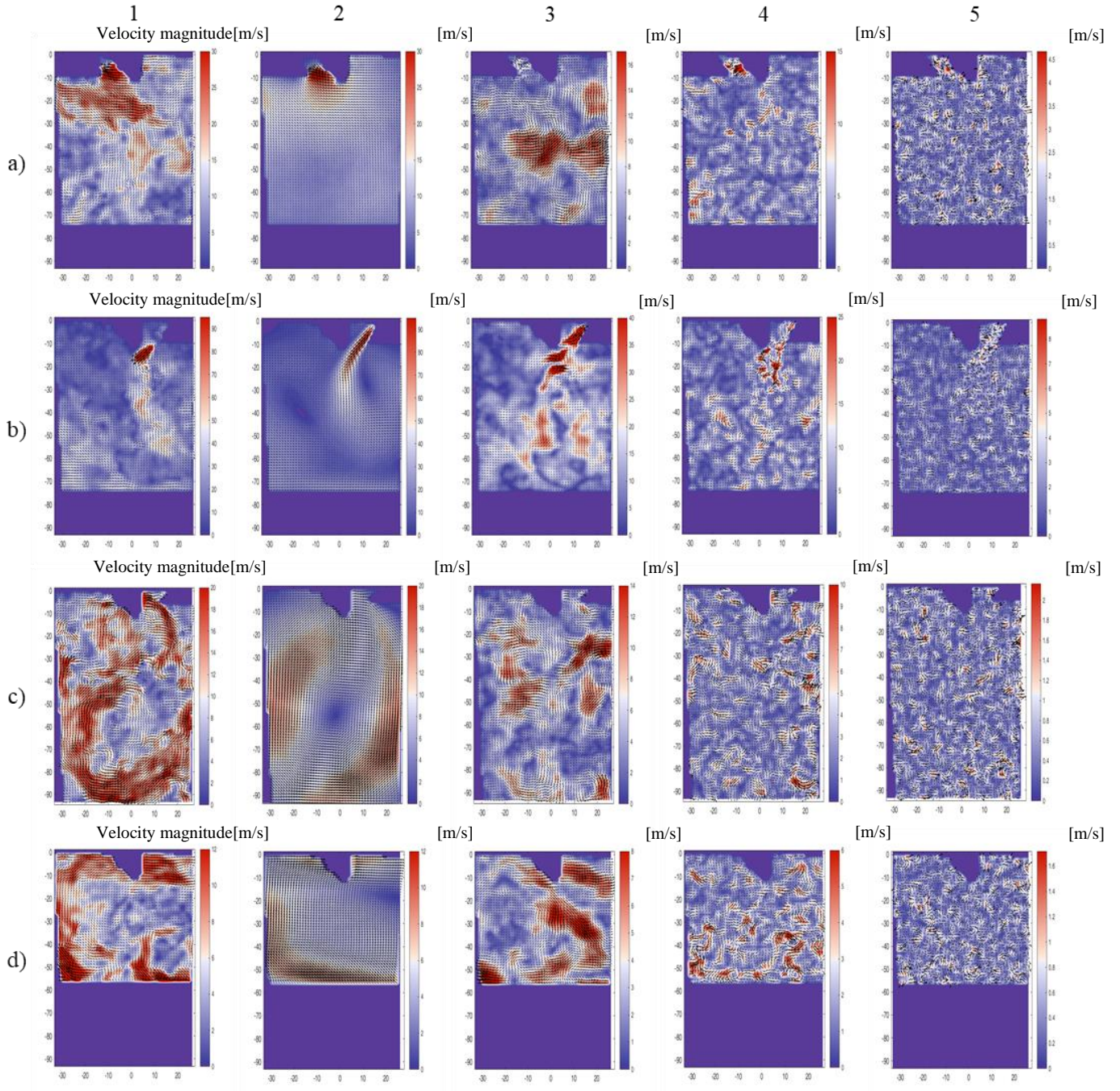


Figure 28 Qin's POD quadruple decomposition for CA position (1) 245, (2) 475, (3) 540, (4) 630, (a) Instantaneous flow field, (b) Mean flow field, (c) Coherent flow field, (d) Transition part, (e) Incoherent flow field

The decomposition introduced by Qin et al., based on correlation coefficients, reduces the selection of the cutoff length to energy-based considerations. This method gives a different definition of the coherent flow field compared to Roudnitzky's triple decomposition. While Roudnitzky's coherent part is reaching the anisotropy of the flow field, Qin's coherent part just considers the most energetic modes, regardless of the isotropy. The less energetic anisotropic modes are included in the transition part of the turbulence, while it is the opinion of the author that any anisotropic mode should be included in the coherent part of the turbulence, since it is responsible for the variations. Once applied to the available experimental dataset of the TCC-III engine, only few modes are identified in the incoherent part of the turbulence. Most of the less energetic modes, even those where the isotropy is well recognizable, are associated with the transition part. It is then difficult to state what is the contribution to the CCV of the transition part.

3.7 Alternative POD Decomposition

The coherent part of the turbulence is composed of high energetic anisotropic vortices. By applying any of the previous decomposition methods, as visible in Figure 23 and Figure 28, it is possible to recognize that incoherent turbulence is composed of homogeneously distributed vortices with decreasing dimension. Consequently, the energy associated with each reconstructed flow field is progressively decreasing.

To overcome the difficulties in defining the cutoff number for the coherent part of the turbulence, a technique is developed and proposed that is based on the Kolmogorov's hypothesis for homogeneous turbulence. As already mentioned in Section 2.1, Pope in [63] gave a formulation of Kolmogorov's hypothesis on a N -point distribution in physical space (x) at a fixed time t , which is analogous to the reconstructed velocity field that we are considering. On a simple domain G within the turbulent flow, and let $x^{(0)}, x^{(1)}, \dots, x^{(n)}$ be a specified set of points within G , new coordinates and velocity differences are defined by:

$$y \equiv x - x^{(0)} \quad [3.32]$$

$$v(y) \equiv U(x, t) - U(x^{(0)}, t) \quad [3.33]$$

And the joint PDF of v at the N points $y^{(0)}, y^{(1)}, \dots, y^{(n)}$ is denoted by f_N . Kolmogorov's definition of local homogeneity states that the turbulence is locally homogeneous in the domain G if, for every fixed N and $y^{(n)}$ ($n = 1, 2, \dots, N$), the N -point PDF f_N is independent of $x^{(0)}$ and $U(x^{(0)}, t)$. Analyzing the reconstructed flow field on the modes, the author believes that the key to objectively recognize the cutoff mode for the separation between the coherent turbulence and the background turbulence is the

homogeneity on the FOV domain. To quantify the homogeneity on the dominion recognized by the FOV, an analysis on the velocity distribution along all the FOV is performed.

At least 30 control points are individuated all over the non-zero values of the FOV. In accordance with Kolmogorov’s hypothesis, the PDF of the velocity components on 100 grid values around each control point is evaluated in terms of mean velocity and standard deviation. A value is obtained for each control point on every POD mode. The variance of the values among all the subsections is analyzed for each mode. Results are shown in Figure 29.

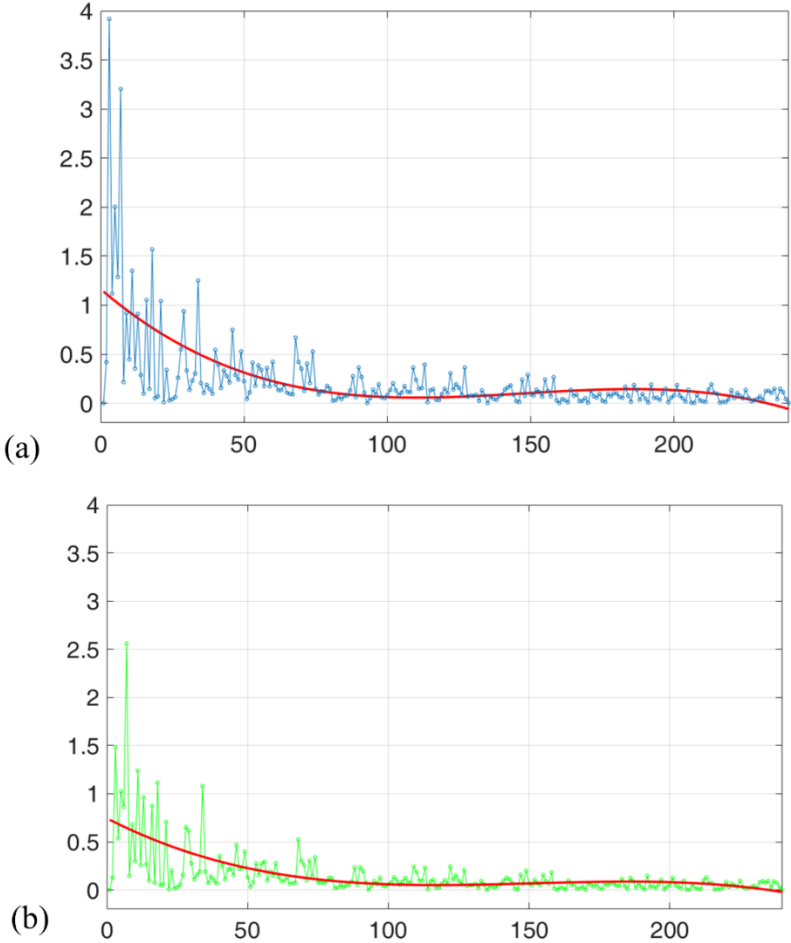


Figure 29 Variance of Mean velocity (a) and standard deviation (b) on the grid for CA position 540

The minimum number of points is 30 for every CA position to preserve the same level of accuracy and statistical significance independently of the piston position. The number of points for the analysis (30) and the number of the grid points (100) around them for the statistical evaluation of the flow conditions are chosen as a trade-off to work properly for every analyzed CA position. In the chosen dataset, the CA position highly affects the number of points of the flow field. At TDC, just 4% of the total FOV has

non-zero values. Consequently, the 100 velocity values around every of the 30 selected points may overlap, but Kolmogorov’s hypothesis is not contradicted. At BDC, the number of 100 values could be increased without overlapping, but this number is sufficient to guarantee the statistical significance of each sample. The distribution of the control points on the FOV for different CA positions is shown in Figure 30. In the opinion of the author, the chosen values should even fit on grids with different resolutions, but further analyses should be performed to confirm it.

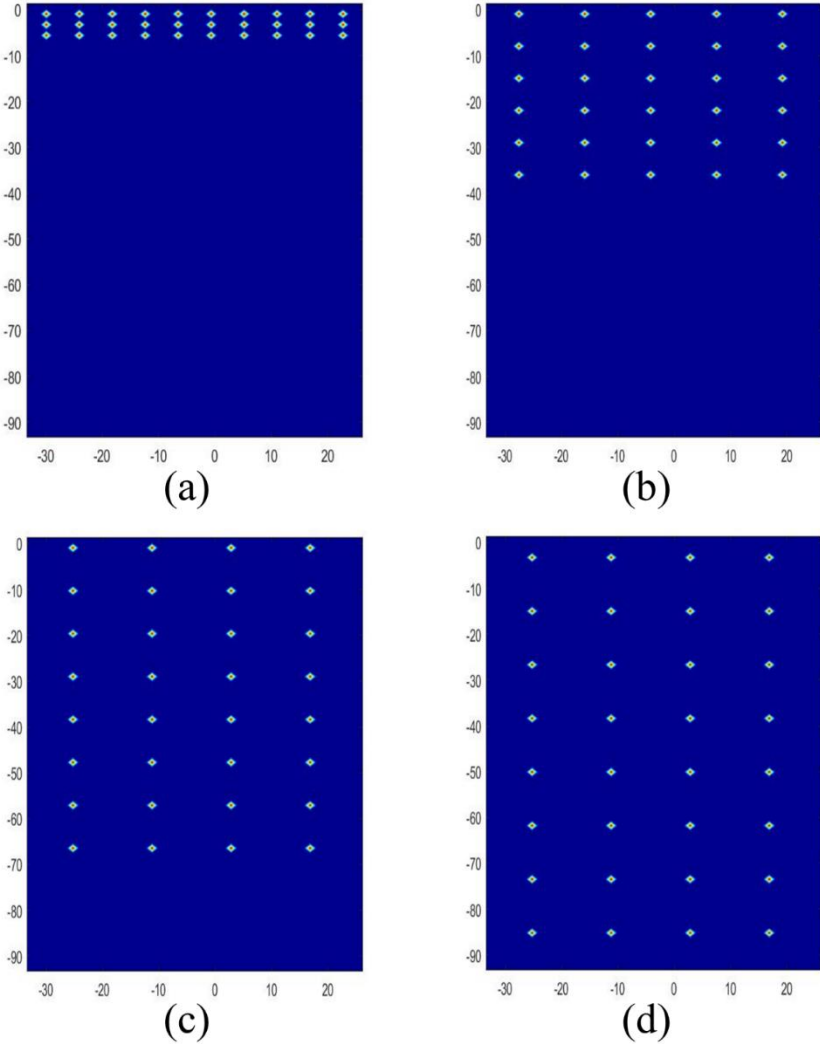


Figure 30 Representation of the distribution of the control point on the grid on different CA position (a) TDC, (b) 70 CA ATDC, (c) 475 CA position, (d) BDC

The variance of both mean velocity and skewness on the subsections has high values in the first 50 modes and rapidly decreases in the last modes. Combining these results, it is possible to define a cutoff mode for the coherent turbulence. The cutoff mode for the coherent turbulence is identified as the point

where the slope of the function interpolating the variance of both mean and standard deviation converge around zero.

As for the transition part of the turbulence, it must be considered as a tool to better identify the energy cascade in the analyzed modes. As already discussed in Session 3.6, Qin's method is based on a purely energetic approach, which might be insufficient to completely identify the coherent part of the turbulence. The coherent part should indeed take into account the anisotropy in the flow field, even if it arises from less energetic modes. For this reason, the author deliberately avoids proposing a method to objectively define the cutoff mode for the transition mode. Conversely, objective information about the incoherent part of the flow field is given, implementing a method to evaluate the size of the main turbulent structures in the reconstructed flow field. Such method uses 2D Fast Fourier transform (FFT) to perform a low-pass filtering on the space-frequency domain of the FOV. This technique allows recognition of the dimension of the dominant flow structures in each reconstructed POD mode. The obtained quantitative result can be used as a tool to objectively identify the turbulent structures themselves. The space-frequency domain is identified as the FOV of the PIV grid. Considering each component of the velocity flow field as a function:

$$u(k_1, k_2) \quad [3.34]$$

where $0 < k_1 < N_1 - 1$ and $0 < k_2 < N_2 - 1$. It is possible to define its two-dimensional discrete Fourier transform as a complex function $U(k_1, k_2)$:

$$U(n_1, n_2) = \sum_{k_2=0}^{N_2-1} \sum_{k_1=0}^{N_1-1} \exp\left(\frac{2\pi i k_2 n_2}{N_2}\right) \exp\left(\frac{(2\pi i k_1 n_1)}{N_1}\right) h(k_1, k_2) \quad [3.35]$$

From Eq. 3.35, it can be noted that the 2D FFT can be computed by performing 1D FFT sequentially on each index of the original function, symbolically:

$$\begin{aligned} U(n_1, n_2) &= \text{FFT_on_index_1}(\text{FFT_on_index_2}[u(k_1, k_2)]) \\ &= \text{FFT_on_index_2}(\text{FFT_on_index_1}[u(k_1, k_2)]) \quad [3.36] \end{aligned}$$

A spatial filtering procedure is performed recursively for each mode. An accurate description of the spatial filtering procedure can be found in [10]. First, the 2D FFT is performed on the spatial-frequency

domain, treating each velocity component separately. In each dimension, the spatial-frequency domain extends to the Nyquist limit:

$$k_{Nyq} = \frac{1}{2\Delta l} = 1mm^{-1} \quad [3.37]$$

Where Δl is the PIV grid spacing.

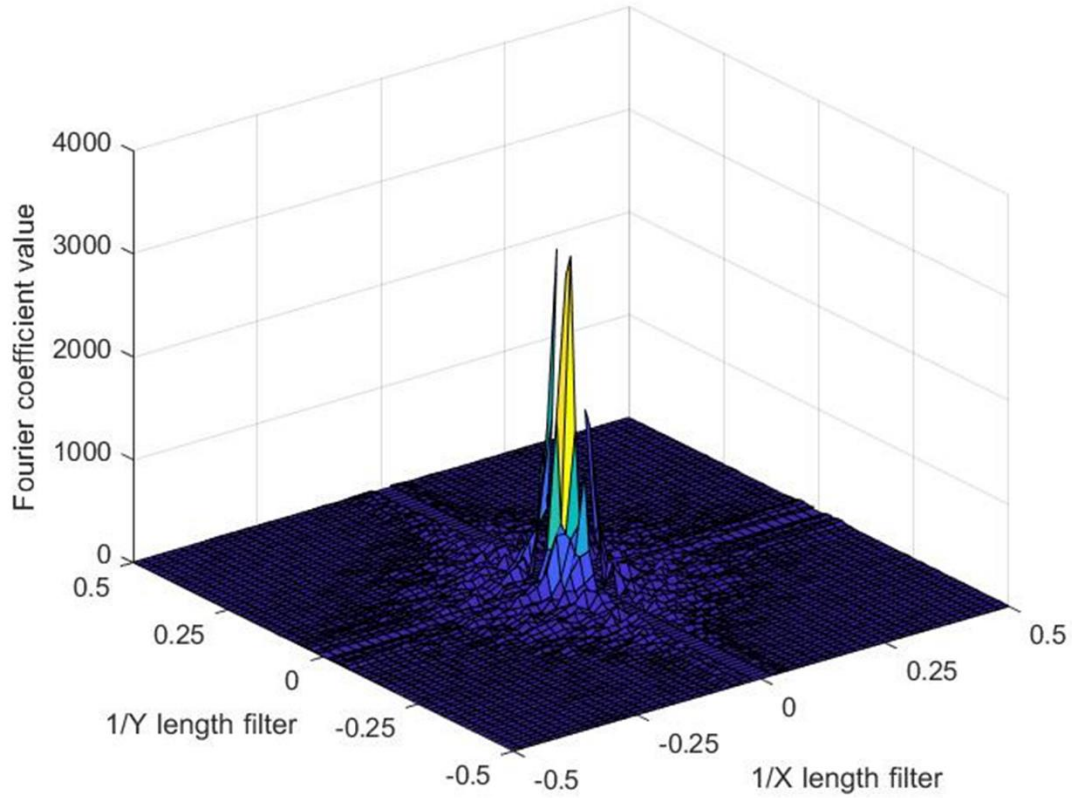


Figure 31 Fourier coefficient for the FOV space-frequency domain. On X and Y axis the length filter, on Z the module of the Fourier coefficient

Figure 31 shows Fourier coefficients associated with the correspondent spatial cutoff frequency. Then, a low pass filtering is performed by setting to zero all the Fourier coefficients above the desired spatial frequency cutoff. The characteristic length scale L_{co} corresponding to the spatial-frequency cutoff k_{co} is:

$$L_{co} = \frac{1}{k_{co}} \quad [3.38]$$

The inverse Fourier transform to real space domain is performed on the modified Fourier coefficients and a filtered flow field is reconstructed for each component of the velocity field. A computation of the total kinetic energy of the flow field is performed to define the cutoff frequency corresponding to the most energetic flow structure. Since the kinetic energy is proportional to the squared velocity, the total kinetic energy for the reconstructed flow is computed as follows:

$$k_i \approx \sum_{k_2=0}^{N_2} \sum_{k_1=0}^{N_1} u(k_1, k_2)^2 + v(k_1, k_2)^2 \quad [3.39]$$

The same method is used for the computation of the reconstructed flow field from the inverse Fourier transform. The cutoff frequency is defined at the point where the total kinetic energy of the filtered flow field is equal to 10%.

$$k_{filtered}(k_{co}) = 0.1 \cdot k_i \quad [3.40]$$

where k_{co} is the cutoff length filter. The 10 % value is obtained through a quantitative evaluation. Figure 32 shows the reconstructed flow for the second POD mode at 475 CA and the low-filtered reconstructed flow field for the cutoff length selected.

Velocity magnitude [m/s]

Velocity magnitude [m/s]

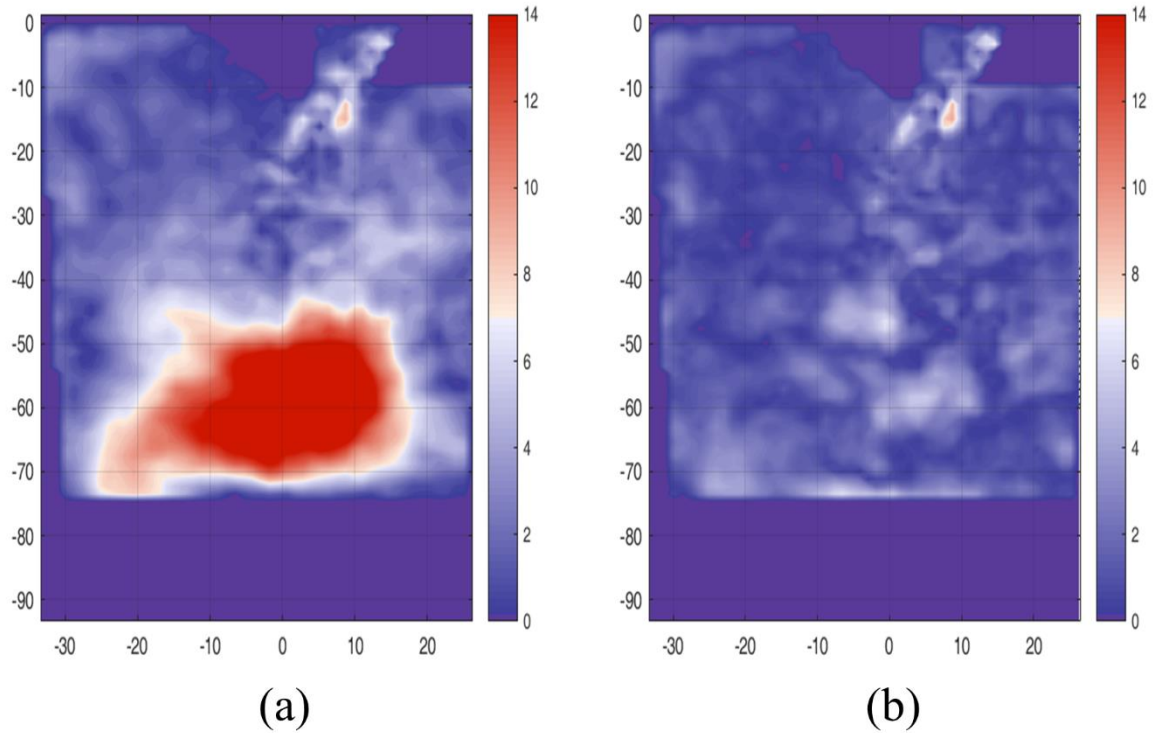


Figure 32 Flow reconstruction of the second POD mode (a) and the low-pass filtered reconstructed flow (b) for the flow frequency 25 mm on CA position 475

The kinetic energy is deeply correlated to the mass. Considering similar velocity values, the increase in density during the compression stroke implies a higher kinetic energy if compared to the expansion stroke. In our method, though, the kinetic energy is applied to the same CA position for each mode. Therefore, the mass involved is constant, and it is not necessary to consider it in the computation.

A distribution of the cutoff length dimension is shown in Figure 33. The characteristic length reaches the value of 3 mm in the less energetic modes. A comparison with a reconstructed flow field of the last mode, shown in Figure 34, confirms the coherence of the model.

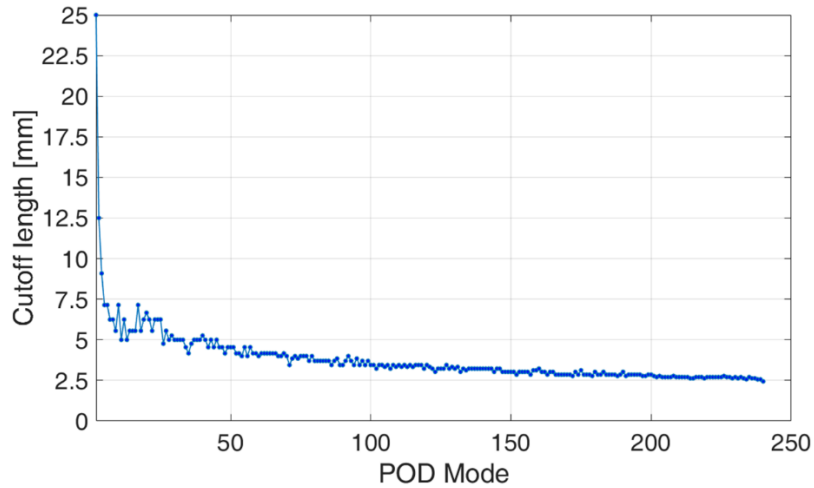


Figure 33 Cutoff length defined with FFT filtering procedure on CA position 540

The characteristic length for each reconstructed flow field from POD modes represents an objective datum for the analysis of the turbulent flow field. It is still difficult to select a cutoff mode to separate the transition turbulence from the incoherent background turbulence. The length of the main turbulent structures can be used to separate the different contributions. This technique is connected to the size of the grid. In our case the smallest vortices are identified with a characteristic length of 3 mm. This value agrees with the PIV grid size, which is 1.15 mm. This means that the chosen cutoff size is nearly three times the grid spacing, and this has been taken as a criterion to define the incoherent turbulence.

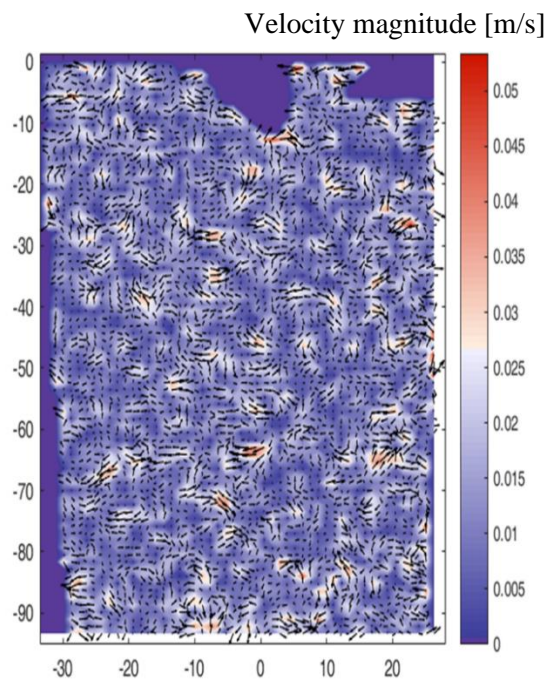


Figure 34 Flow reconstruction of the last POD mode

Figure 35 shows the distribution of the energy among each defined part of the turbulent flow for four CA positions using the two quadruple methods. Since the mean part is the same, the distribution differs only for the fluctuating part of the turbulence. Despite trends are similar, the newly proposed decomposition shows some substantial difference. At the 245 CA position, for example, a higher energy is associated with the coherent part. This part of the turbulence is associated with CCV because of its relatively high energetic content. The RMS calculated for the CA position, in Figure 36, shows diffused variations all over the FOV. On the contrary, the RMS calculated on the CA position 630 shows a lower module, in accordance with the lower energetic level associated with the coherent part defined by the new decomposition method. The results of the new POD quadruple decomposition are shown in Figure 37.

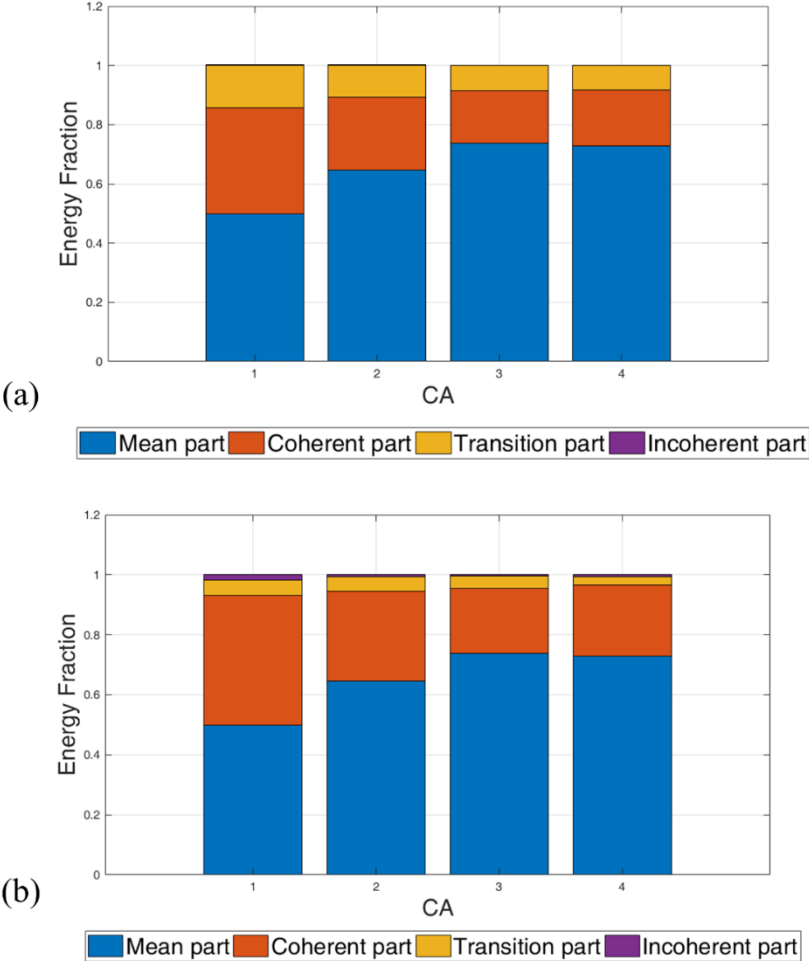


Figure 35 Spectrum of the energy for each part of the turbulent field for (a) Qin's quadruple decomposition, (b) newly proposed quadruple decomposition

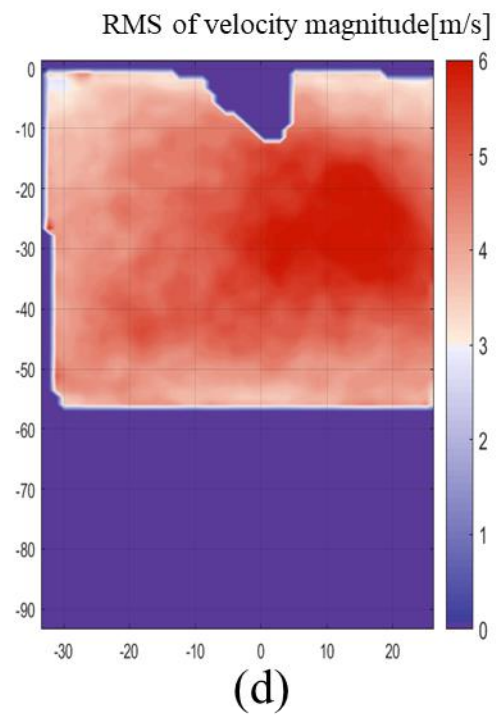
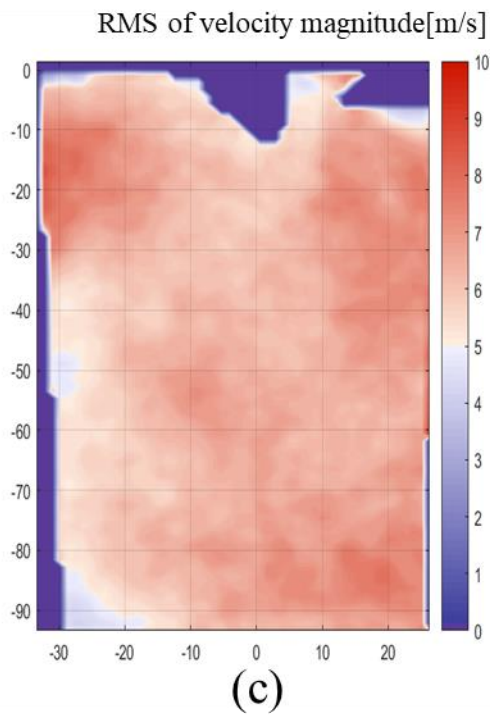
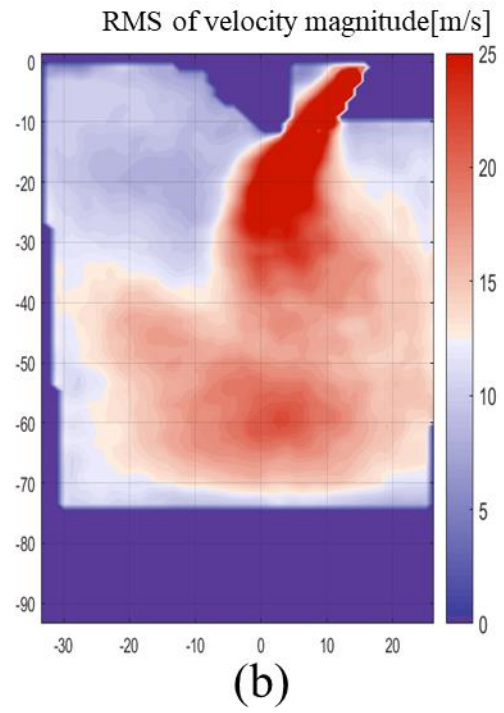
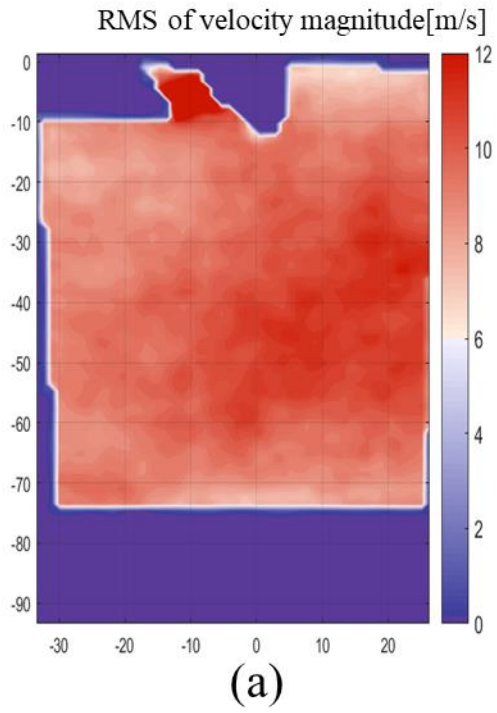


Figure 36 RMS calculated for CA position (a) 245, (b) 475, (c) 540, (d) 630

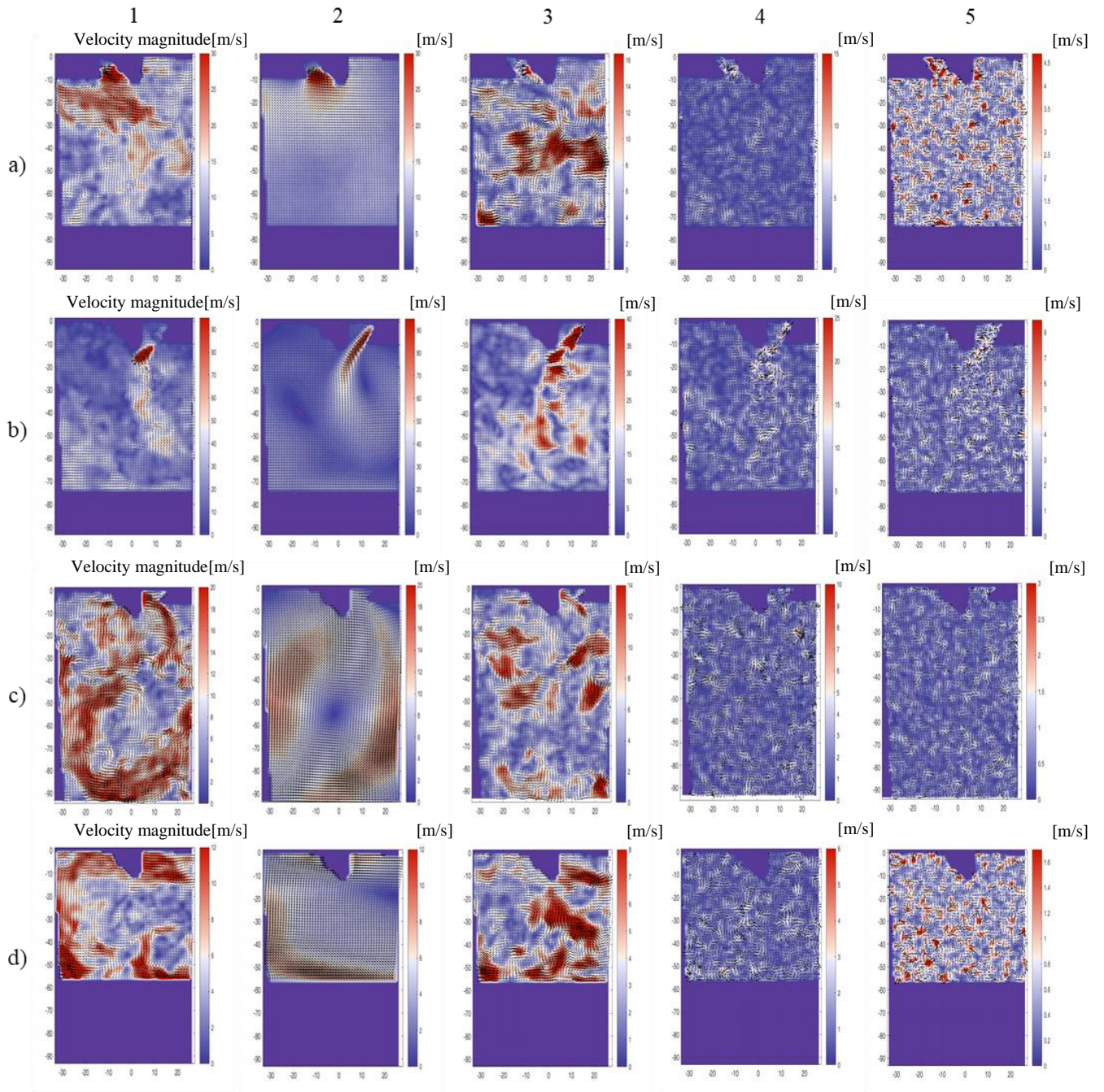


Figure 37 Proposed POD decomposition method for CA position (1) 245, (2) 475, (3) 540, (4) 630, (a) Instantaneous flow field, (b) Mean flow field, (c) Coherent flow field, (d) Transition part, (e) Incoherent flow field. The analyzed cycles and the scale are the same of Figure 28 Qin's POD quadruple decomposition for CA position (1) 245, (2) 475, (3) 540, (4) 630, (a) Instant flow field, (b) Mean flow field, (c) Coherent flow field, (d) Transition part, (e) Incoherent flow field to make the results comparable.

The application of the new quadruple method to the CA closest to TDC, as for example in Figure 38, gives a null or negligible contribution of the transition part to the total energy.

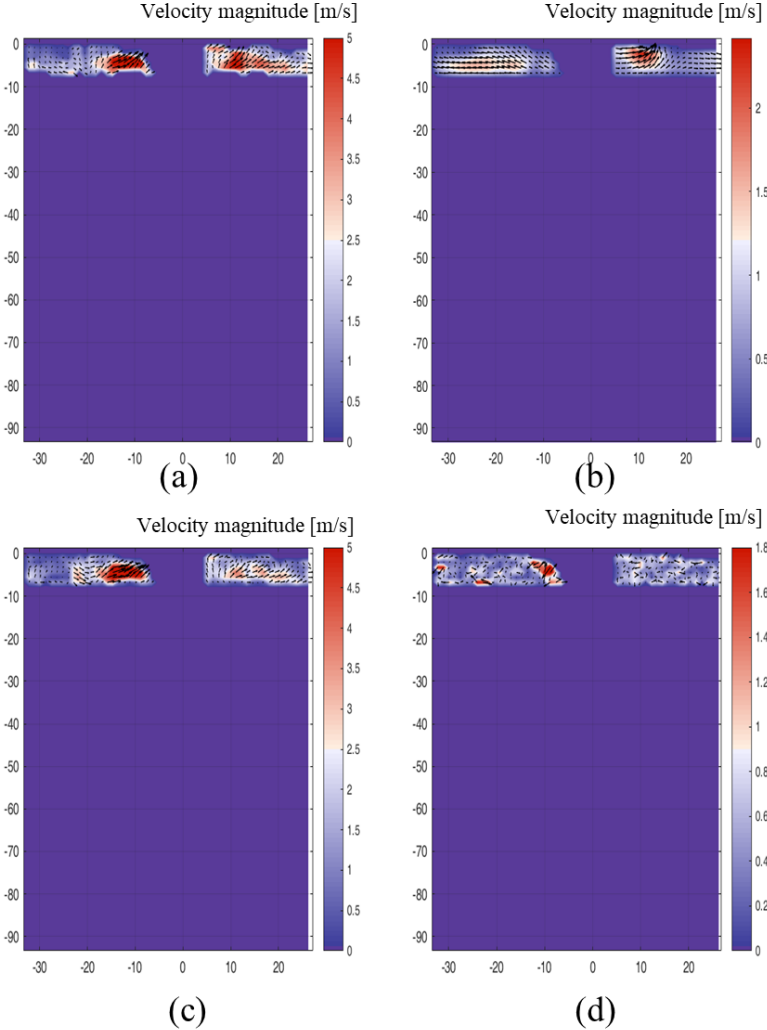


Figure 38 For CA position 360 CA, Instantaneous Flow field (a), Mean part (b), Coherent part (c) and incoherent part (d) of the turbulence

This happens because the vortices of the incoherent turbulent part are below the chosen threshold of 3 times the cell dimension, since they are very low energetic turbulent structures. The reason can be found both in the limited room available for the fluid at TDC and in the energetic distribution among all the modes. As reported in Section 3.1 and shown in Figure 38, 360 CA position is critical to analyze because of the distribution of the velocity on a limited portion of the FOV. Very little information can be extracted. It can be concluded that a transition part of the turbulence, defined as the most energetic part of the incoherent part of turbulence, might not always be recognized. Furthermore, the author believes that combining the transition part with the incoherent part of turbulence does not affect the level of accuracy that can be reached with the proposed analysis. The spatial filtering method gives objective

results to make considerations on the incoherent part of the flow field. To allow a fair comparison, results for the same cycle are shown for all the methods. Figure 39 shows the potential of the method in understanding CCV. Figure 39 (a) shows two different yet apparently similar cycles. The coherent parts resulting from the proposed decomposition method, shown in Figure 39 (b), are extremely different, especially in terms of penetration of the tumble motion.

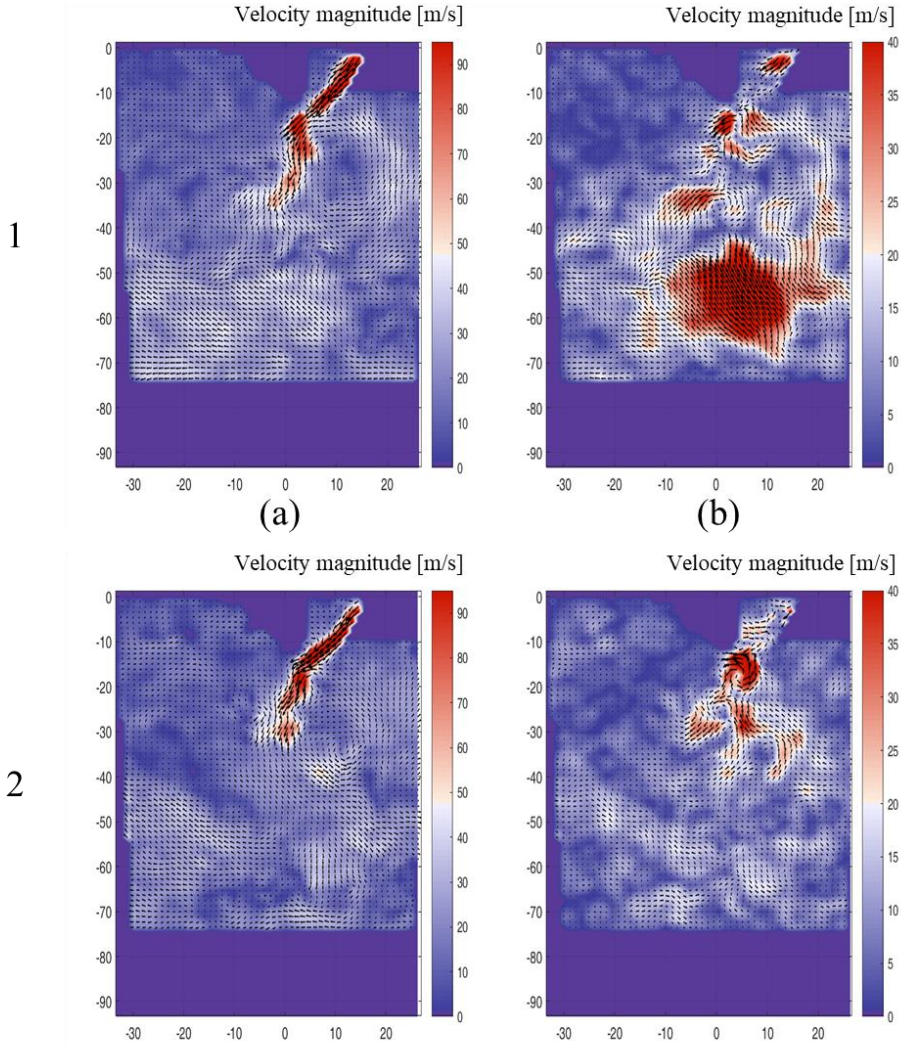


Figure 39 a) Instantaneous flow field and b) Coherent part of the turbulence for cycles 1) 114 and 2) 144

For a quantitative analysis of the contribution of every part of turbulence relative to the two considered cycles, a normalization of the energy content of every single part of turbulence is performed. The energy spectrum resulting from the POD analysis is associated with the POD modes. The flow reconstruction is deeply correlated with the value of the POD coefficients. To account for this contribution, the author adopts the same considerations on the kinetic energy as those for the FFT analysis. The kinetic energy

associated with each flow field reconstructed from POD modes is computed as in Eq. 3.39. The energy fraction associated with each reconstructed flow is estimated as:

$$e_i = \frac{k_i}{\sum_{j=1}^{N_{tot}} k_j} \quad [3.41]$$

where N_{tot} is the total number of modes and k_i is the kinetic energy associated with the i^{th} mode. Considering the contribution of every reconstructed flow field to each part of turbulence coming from the POD decomposition, an energy spectrum is obtained, and it is reported in Figure 40.

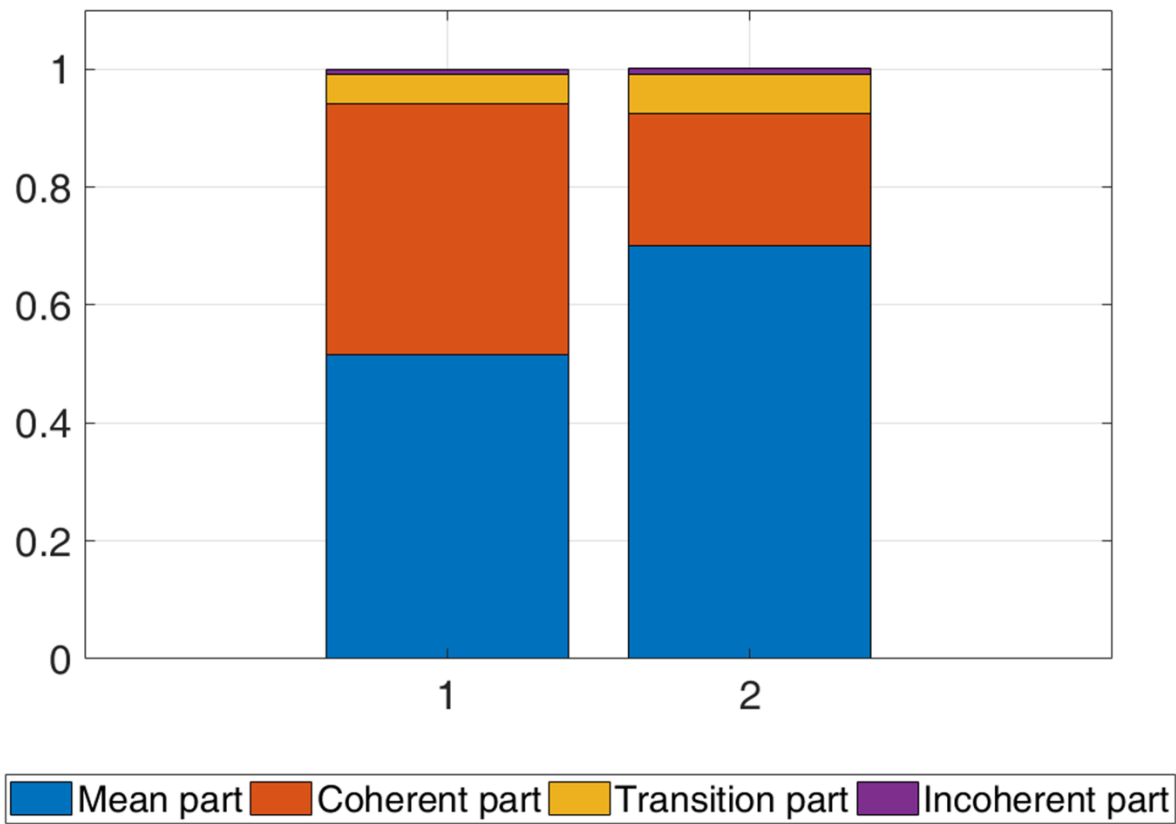


Figure 40 Energy spectrum for CA position 475 for (1) cycle 114 and (2) cycle 140

The energy associated with the coherent part for cycle 114 is consistently higher than the one in cycle 144, confirming the visual representation shown in Figure 39. The energy associated with the mean part, i.e. the tumble motion, is higher in cycle 144. Consequently, less variability is found in this cycle. This technique will be applied in Section 5.3.2 to an LES dataset.

3.8 Discussion

The purpose of the work presented in this Section was a critical investigation on methods of analysis based on POD, focusing on their potential and limitations for the analysis of CCV in ICEs.

POD is a well-established and powerful mathematical technique, whose effectiveness in understanding engine CCV has been long debated. As a purely mathematical method, a physical interpretation is not always straightforward. The application of the phase-dependent POD analysis, described in Section 3.3, allows a quantitative evaluation of the energy distribution among the turbulent structures by means of the POD coefficients. From a visual standpoint, a graphical representation of POD modes can give an idea of the most energetic turbulent structures, but little information can be derived. The analysis can even produce misleading results if it is not critically evaluated, as shown in Figure 8.

The conditional averaging method, described in Section 3.3, uses POD as an objective tool to obtain a qualitative representation of CCV. The method is easy to set up and its application to the TCC-III dataset is useful for analyzing CCV onset during the intake phase. Despite the general effectiveness of the method, it should be adopted with care, especially for low populated datasets, where the statistical significance of the obtained subsets might be poor. This is, for example, the typical case of LES CFD analyses, for which each subset might be composed by an insufficient number of samples, which would affect the statistical significance of the analysis. In the specific case of the PIV dataset of the TCC-III engine, the method provides its most useful information during the intake phase. Qualitative information on CCV can be obtained also at other CA positions, as shown in Figure 5, but it is harder to identify the origin of the variance from the POD modes.

The POD triple decomposition, described in Section 3.4, pioneers the concept of decomposing the turbulent field in separate parts based on the POD modes. In the opinion of the author, the method to identify the mean part of the turbulent flow field is objective and effective. The assumptions about the velocity distribution made for the identification of the coherent part of the turbulence are again correct, while an objective criterion for the choice of the cutoff number between the coherent and incoherent turbulence is not identified.

The POD quadruple decomposition proposed by Qin et al., described in Section 3.5, extends the triple one by including a transition part in the decomposition of the turbulent field. From a physical standpoint, such extension should improve the understanding of the energy cascade from coherent turbulence to background incoherent turbulence. A different method for the selection of the cutoff modes is also proposed, based on correlation coefficients. In the application to the TCC-III dataset, the author found that this technique is purely energy-based and does not take into account the anisotropy of the flow field.

As a result, a relevant part of the energy of the anisotropic flow field is associated with the transition part. Results of the application of the correlation coefficient for the individuation of the cutoff number between the transition and the incoherent part of the turbulence is again hard to objectify.

From the considerations above, it appears evident that all the analyzed methods are useful tools for researchers to perform qualitative and quantitative descriptions of CCV. Yet, they are characterized by a certain lack of objectiveness in their application, as highlighted in the manuscript.

A new POD decomposition method is proposed by the author. This method is based in part on Kolmogorov's hypothesis, for the identification of the transition part of turbulence, and on FFT filtering, for the incoherent part of turbulence. The purpose of the method is to reach a higher level of objectiveness, thus overcoming the limitations described earlier. Attention is paid to the recognition of the anisotropy of the flow field. Since the coherent part of the turbulence is associated with CCV, the author believes that any anisotropy should be associated with the coherent part of the turbulence. To allow comparisons with the previously described quadruple decomposition, a transition part of the turbulence is identified as the most energetic part of the incoherent turbulence. Considering the information given by the FFT spatial filtering on the incoherent part of the turbulence, it is possible to neglect a so-called "transition" part of turbulence, without affecting the level of accuracy that can be reached with the proposed method.

The proposed POD quadruple decomposition will be applied later on a LES dataset to assess its potential in evaluating the quality of the simulated data in comparison with the experimental ones.

Chapter 4

LES investigation: subgrid models and quality criteria

In recent years, LES has been strongly spotlighted as a powerful tool for ICEs, in particular for the analysis of CCV. When targeting CCV, many consecutive cycles must be simulated and then statistically analyzed. Therefore, high performance computing systems are required to conduct LES analyses for CCV [76] of complex geometries such as ICEs. Thus, it is fundamental to find the best trade-off between accuracy and LES computing cost. It is well known that calculation accuracy and efficiency are, to some extent, competing instances [77, 78]. Therefore, a study of LES quality indices and their impact of simulation accuracy provides a reference for the relationship between calculation efficiency and its predictability. Severe research efforts for LES quality indices in relatively simple geometries and/or flow conditions such as channel flows have been carried out for a long time. Further studies [34, 79, 80] were conducted to investigate the effect of numerical schemes and grid density on modeling and numerical errors. Many researches have also been carried out to develop LES quality indices [35, 78, 80, 81]. Davidson [82] investigated a two-point correlation method on channel flow, stating that two-point correlation method is one of the best measurement techniques to estimate LES quality. However, its drawback is that it is hardly applicable to ICEs. In recent years, Di Mare et al. [36] carried out an extensive application of LES quality indices on ICEs. In this study, Di Mare et al. investigated the possibility of using 5 types of single-grid estimators and a two-grid estimator on different grid densities. However, a limitation of this study is that it was performed without any validation versus experimental data. A further study was carried out by Ko et al. [83], who compared the LES quality with PIV data. In this section, three subgrid-scale models are tested on the TCC-III engine, namely the static Smagorinsky, the dynamic Smagorinsky and the dynamic structure model. LES quality indicators are applied to the three datasets[48].

The section is structured as follows: first the numerical setup is described. Then results from LES quality indicators are briefly introduced. Finally, results for the three models are shown and discussed.

4.1 Numerical setup

The LES investigation of the TCC-III engine is performed using the STAR-CD v4.22 finite volume method (FVM) code licensed by Siemens PLM. The computational domain is shown in Figure 41. The entire domain is meshed using cells of mainly hexahedral shape. The grid size of the intake and exhaust plenums is 6 mm and that of the ports is 1.5 mm. The in-cylinder grid size is 1mm. The near valve regions are refined to 0.4 mm and the grid size around the spark plug is 0.6 mm. The near-wall region is covered by a single layer of prismatic cells aligned to the walls, whose height is purposely chosen to

rely on wall functions. Such choice is considered as a trade-off between simulation accuracy and computational cost of the simulations. The number of cells in the cylinder is approximately 1.15 million at bottom dead center (BDC) and 0.2 million cells at top dead center (TDC). The number of cells in each of the intake and exhaust plenums is 0.5 million cells. The Arbitrary Lagrangian-Eulerian (ALE) formulation and Arbitrary Sliding Interface (ASI) are employed to deal with moving-boundary problems and mesh motion. Pressure Implicit with Splitting of Operator (PISO) algorithm and second-order accurate differencing schemes, namely a monotone advection and reconstruction scheme (MARS), are used for temporal and spatial discretization schemes. Since the experiments were performed on four different section planes at different testing days, it is unreasonable to directly adopt the boundary conditions from the experimental data. Therefore, the 1D code GT-Power is used to obtain unified boundary conditions.

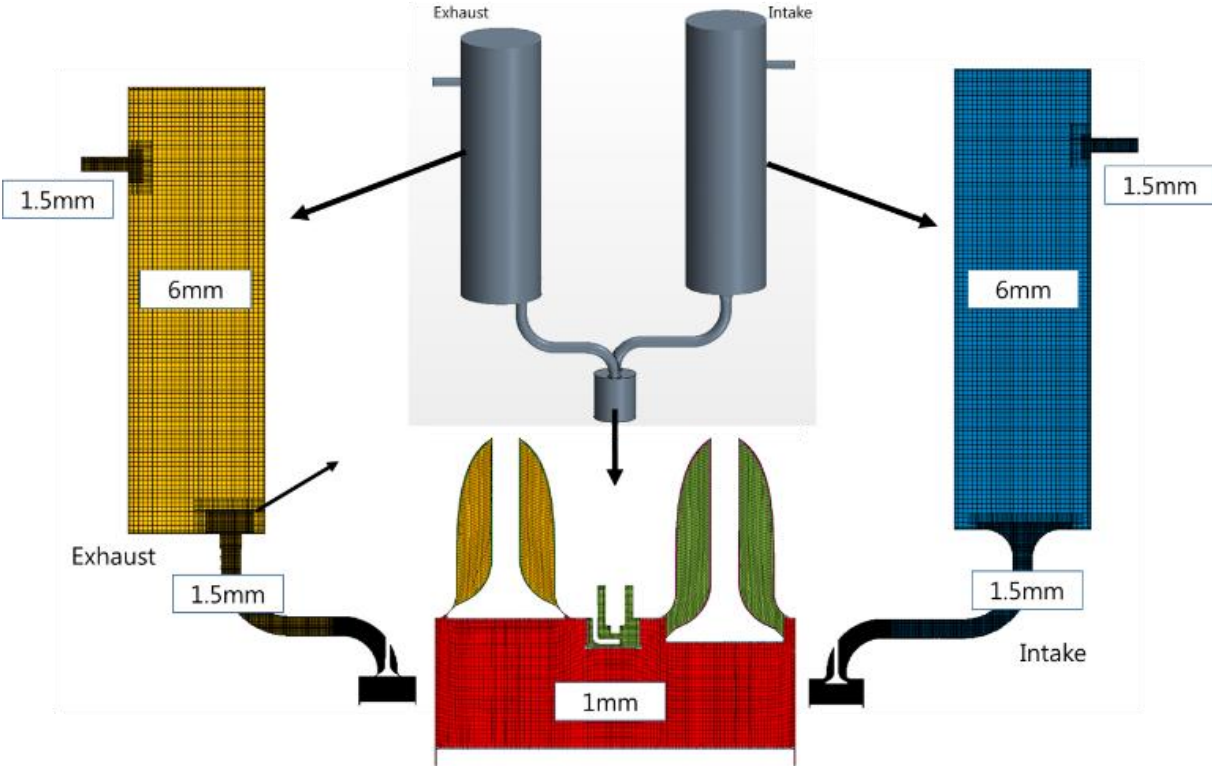


Figure 41 Details of the computational domain for the three datasets

LES simulations are initialized from a preliminary RANS simulation. Then, fifty-one LES cycles are carried out for each of the three subgrid models. The first LES cycle for each dataset is then discarded to avoid any residual impact of the initial conditions.

4.2 LES Quality Indices

In LES, only a fraction of the total amount of turbulent kinetic energy is resolved. In engine simulations, according to the meshing strategy, the mesh size and topology may be not only space, but also time-dependent. In such simulations, the ratio of the resolved turbulent kinetic energy to the total one is also affected by this dependency. In case of implicit filtering, where the cell width is proportional to the filter width, the numerical errors cannot be separated from the modeling errors: the cell width describes the smallest resolvable turbulent scales, and this is directly linked to the subgrid-scale model. In fact, as already mentioned in Eq [2.15] in Section 2.4.1, in Smagorinsky's model the turbulent viscosity is calculated by:

$$\nu_r = l_s^2 \bar{S} = (C_s \Delta)^2 \bar{S} \quad [4.1]$$

As stated in the literature, a progressive refinement of the computational mesh would make the LES approach the limit of the DNS. In this sense, an LES cannot be considered grid-independent as long as it does not resolve the Kolmogorov scales.

In this context, to separate the contribution of the discretization of the computational domain from the modeling error of the subgrid-scale model, the same computational domain has been used and for each dataset.

Among the many possible LES quality indices available in the literature, two relatively simple single-grid estimators were employed. One is the ratio of resolved turbulent kinetic energy to total turbulent kinetic energy, which is the most well-known LES quality index proposed by Pope [78] as follows:

$$IQ_k(x, t) = \frac{k_{res}(x, t)}{k_{res}(x, t) + k_{SGS}(x, t)} \quad [4.2]$$

This quality index should be at least 0.8 to consider the quality of the LES calculation good: this would mean that the mesh resolution is high enough to resolve structures that contain at least 80% of the turbulent kinetic energy. Since the simulation is not stationary, this quality index should be considered as phase-averaged quantity. This indicator will be hereafter referred to as estimator 1.

The other index [34] is based on the fraction of the SGS viscosity and total viscosity as follows.

$$IQ_v = \frac{\nu_t}{\nu + \nu_t} \quad [4.3]$$

This index basically quantifies the “degree of modeling” in LES. This indicator will be hereafter referred to as estimator 2.

4.3 Results

In order to get the best possible comparison among the simulated datasets and the PIV experimental results, the results from the simulations are interpolated on the same PIV grid.

Comparing the averaged fields of experimental velocity PIV and the three sets of 50 LES cycles, a good agreement is generally visible regardless the choice of the sub-grid model.

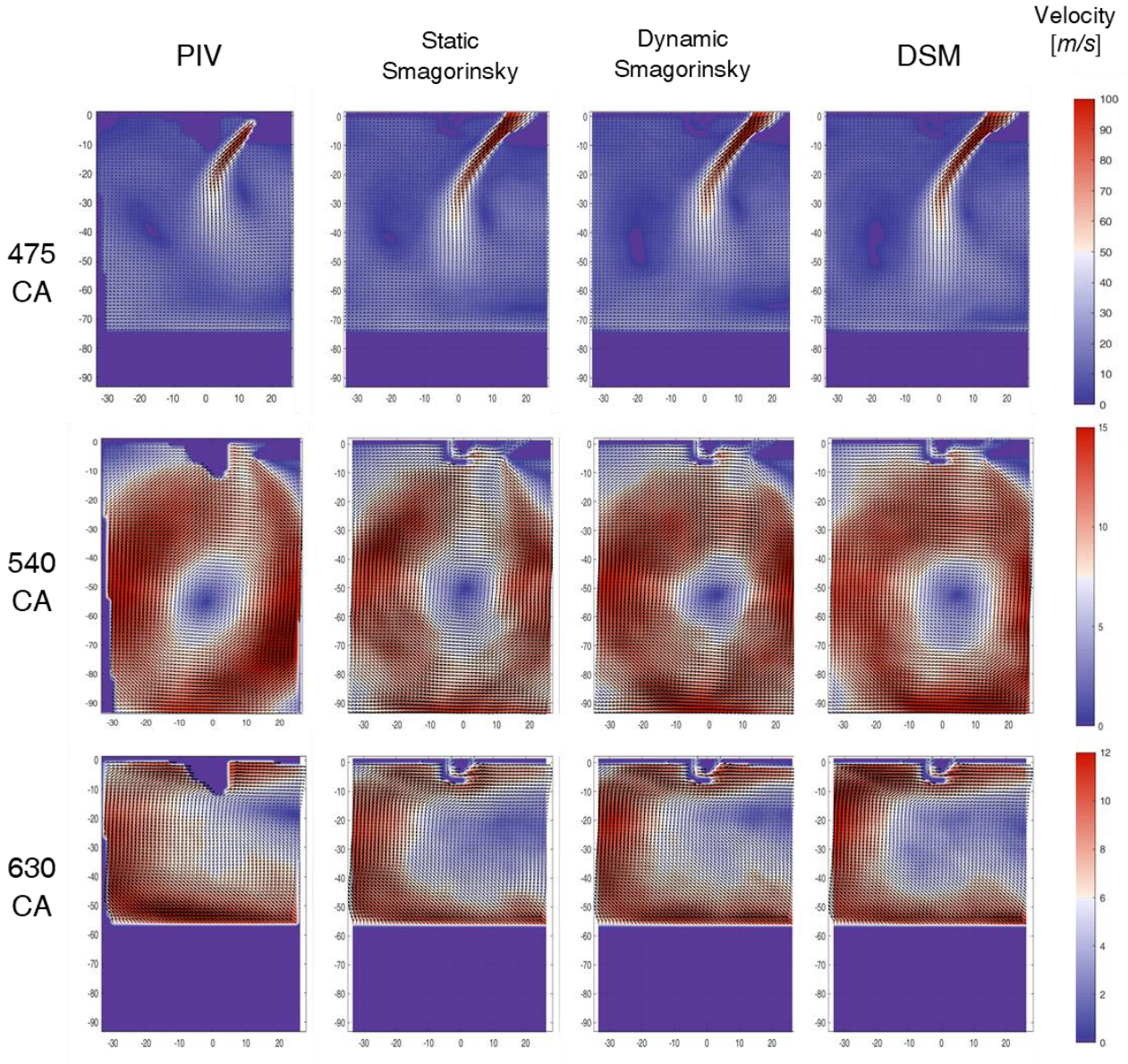


Figure 42 Velocity field comparison on the XZ section plane for the three subgrid scale models and for the PIV experimental results

In order to validate the LES results, the ensemble average of the 50 cycles for each dataset and the 240 cycle from the PIV experimental data is shown in Figure 42

XZ section plane for the three subgrid scale models and for the PIV experimental results. Three CA position are considered significant for the analysis, i.e. 475 CA (nearly mid-intake stroke), 540 CA (intake BDC position) and 630 CA (mid-compression stroke). The three CA position show the evolution of the opposite rotation of the generated tumble vortex (clockwise rotation in Figure 42) with respect to the conventional direction for tumble flow in SI engines (counter-clockwise in Figure 42 convention): this is motivated by the non-canted intake valves/ports in conjunction with reduced flow velocities. A slightly better agreement is shown between the Dynamic Smagorinsky model and the experimental data. All the three models capture the main turbulent structures, but both DSM and Static Smagorinsky models show a deeper penetration of the inflow jet and a lower circulation motion. Conversely, the Dynamic Smagorinsky model, although again slightly overestimating the air jet penetration, shows a bending motion close to the experimental one. Comparing the other analyzed Crank Angle positions, no relevant differences among the cases are highlighted: a general good agreement is shown by all the three models, even though Dynamic Smagorinsky seems to be the most aligned with experimental data. A confirmation of the slightly better behavior of the Dynamic Smagorinsky model comes from the analysis of the so-called “alignment parameter”, defined as:

$$\frac{\vec{A} \cdot \vec{B}}{\|\vec{A}\| \|\vec{B}\|} = \frac{\|\vec{A}\| \|\vec{B}\| \cos(\alpha)}{\|\vec{A}\| \|\vec{B}\|} = \cos(\alpha) \in [-1,1] \quad [4.4]$$

This parameter quantifies the local deviation of the simulated vector field compared to the experimental one, assumed as a reference. If the alignment parameter is equal to 1, PIV and experimental data have the same direction; otherwise, if the alignment parameter is equal to -1, the directions are opposite. Observing the mean values of the alignment parameters in Table 4 and its distribution in the cylinder in Figure 43, the slightly better behavior of the Dynamic Smagorinsky model is evident.

	Static Smagorinsky	Dynamic Smagorinsky	DSM
245 CA	0.611	0.831	0.808
475 CA	0.869	0.876	0.839
540 CA	0.956	0.962	0.939
630 CA	0.948	0.982	0.967

Table 4 Averaged Alignment parameter for the three SGS models in the XZ section.

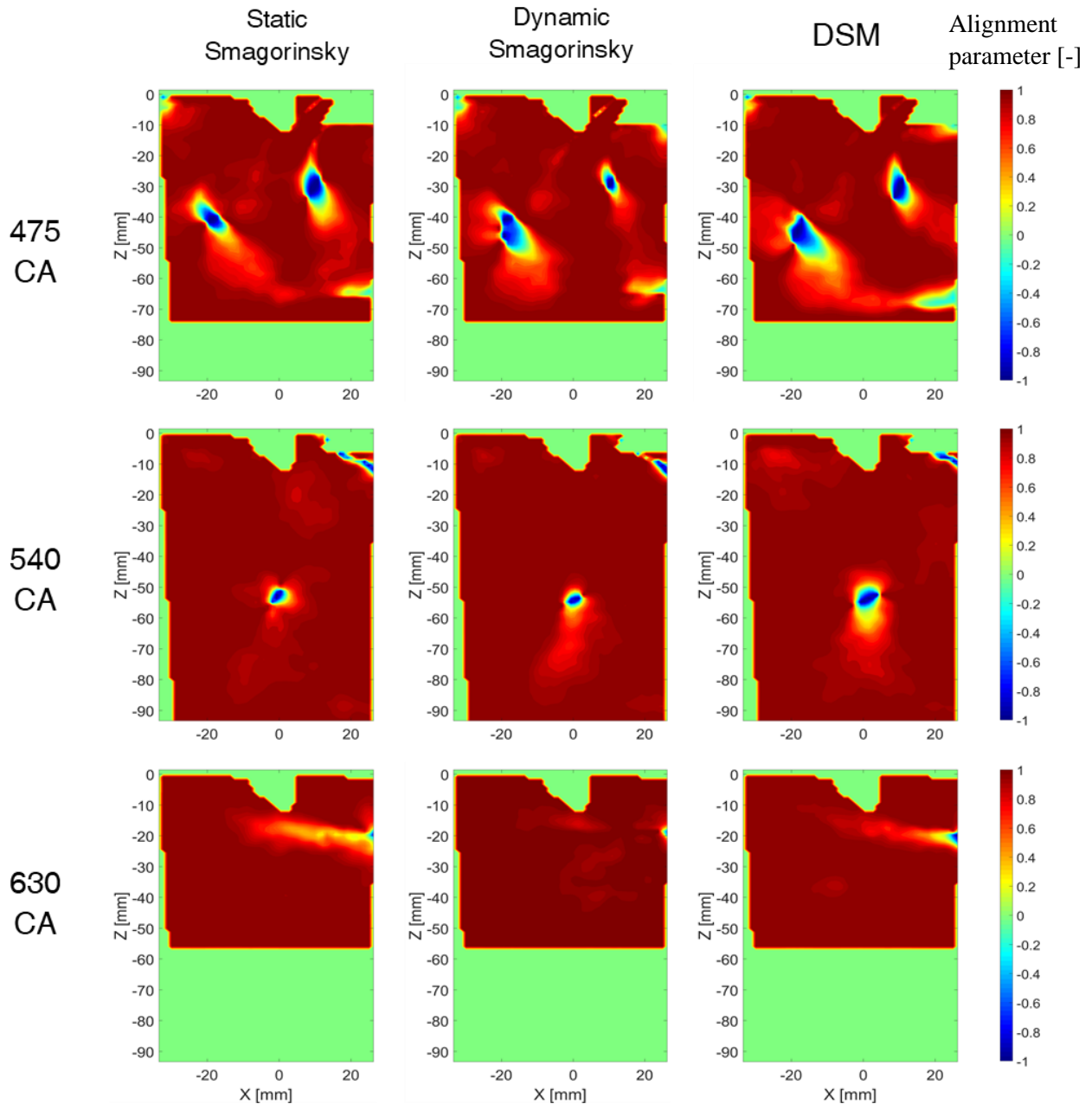


Figure 43 Alignment parameter representation on XZ plane at 475, 540 and 630 CA

Figure 44 and Figure 45 show the comparison among the LES quality estimators. Referring to the definition of the chosen quality estimators, a high level of energy resolution means that a high fraction of the turbulence is directly resolved instead of being modeled by the subgrid scale model. This makes the simulation conceptually comparable to a DNS approach. Conversely, the second estimator shows the relation between the effective viscosity and the one introduced by the subgrid scale: a low value of the estimator indicates a low influence of the viscosity introduced by the SGS model, therefore a higher rate of resolved turbulence and a better correspondence between the effective and the molecular viscosity. All the three models show lower values for the estimator 1 in the zone between the exhaust

valve and the spark plug, where the flow is characterized by the highest velocity gradients. A comparison between the LES quality estimators of Static and Dynamic Smagorinsky models confirms the better quality of this latter, showing both higher levels of energy resolution and lower levels of SGS viscosity over all the cylinder.

The Dynamic Smagorinsky SGS model shows the best alignment with the experimental results, and this is reflected by the analysis of the estimators, which highlights the Dynamic Smagorinsky as the most accurate closure model, as the averaged values reported in Table 5 indicate.

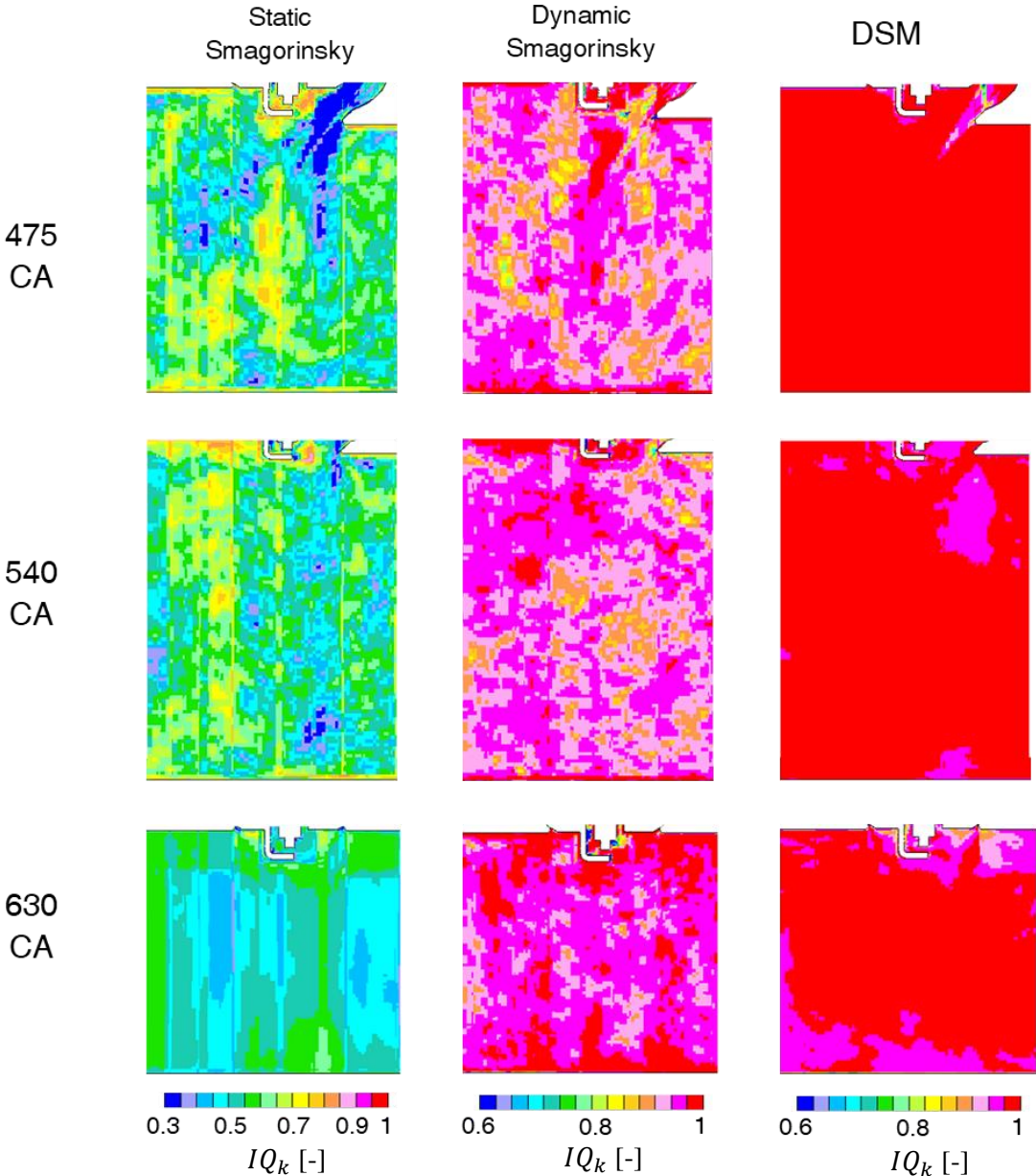


Figure 44 Estimator 1 of Static Smagorinsky, Dynamic Smagorinsky and DSM models at four different CA positions on section plane XZ. Please note that the scale for the Static Smagorinsky case is different.

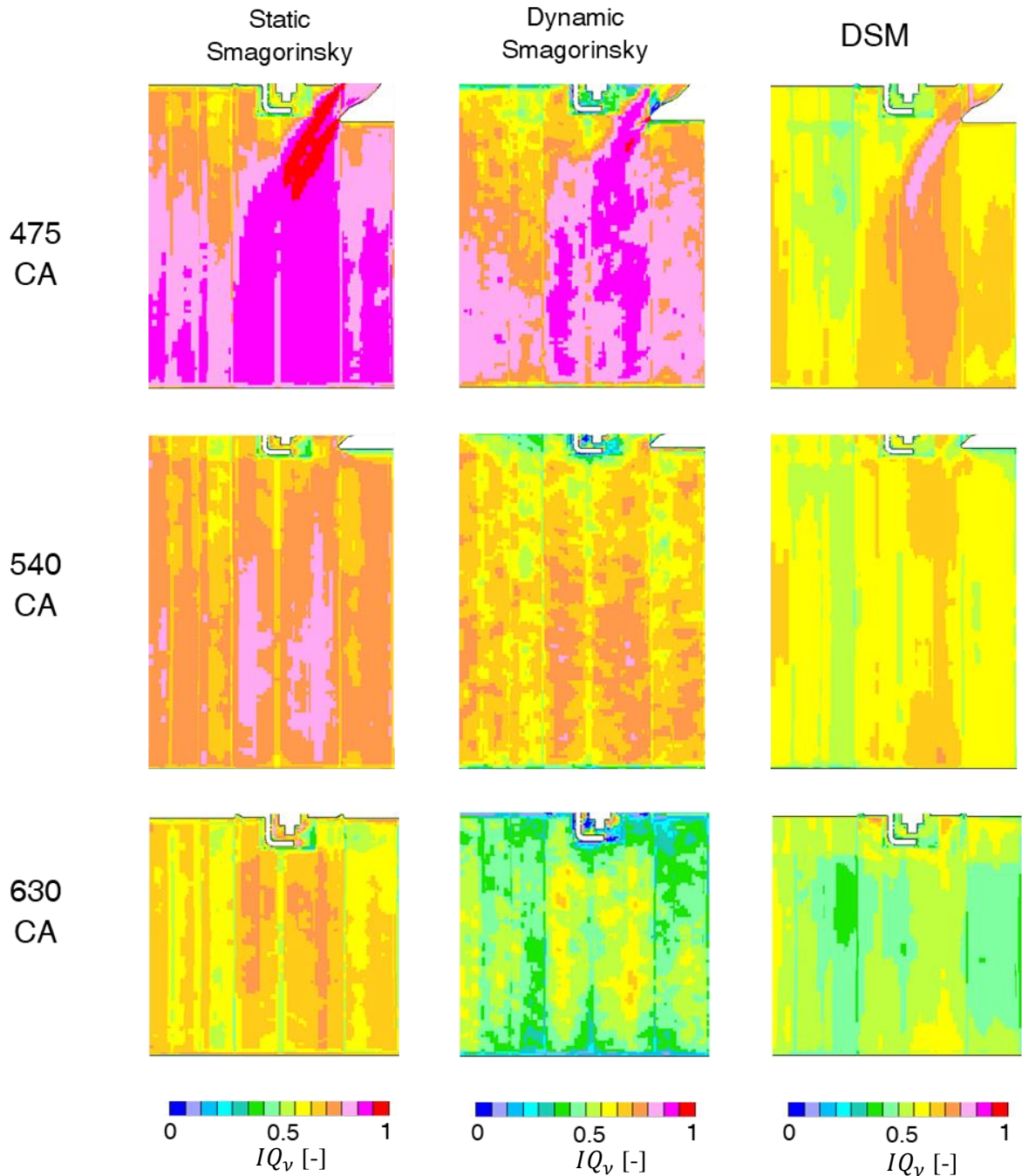


Figure 45 Estimator 2 of Static Smagorinsky, Dynamic Smagorinsky and DSM models at four different CA positions on section plane XZ.

Even though a higher level of estimator 1 generally corresponds to a lower level of estimator 2, the anti-correlation that could be expected is not recognizable. This becomes more evident by looking at the values of the estimators over the entire domain, reported in Figure 46, where no trend is identified. Such evidence primarily indicates that, despite the estimators in the cylinder are well within the suggested range, the LES quality all over the domain is not necessarily as high: Figure 47 shows that a critical zone for the LES quality is represented, for example, by the intake port, as it will be commented later.

Another warning suggested by this analysis is that the two investigated quality estimators cannot be independently considered. Finally, estimators cannot be used as a standalone parameter to define the overall quality of a LES simulation and comparison with available experimental measurements should always be performed. A clear example comes from the simulated cycles using the DSM model: despite showing very high LES quality indices, agreement with PIV data is slightly worse than that of the Dynamic Smagorinsky model.

	Static Smagorinsky		Dynamic Smagorinsky		DSM	
	Estimator 1	Estimator 2	Estimator 1	Estimator 2	Estimator 1	Estimator 2
245 CA	0.53	0.72	0.94	0.50	0.94	0.53
475 CA	0.50	0.74	0.93	0.56	0.91	0.59
540 CA	0.57	0.63	0.93	0.49	0.95	0.52
630 CA	0.61	0.57	0.95	0.42	0.95	0.50

Table 5 Estimators value averaged on 50 cycle for analyzed Crank Angles: highlighted in green the best and in red the worst values.

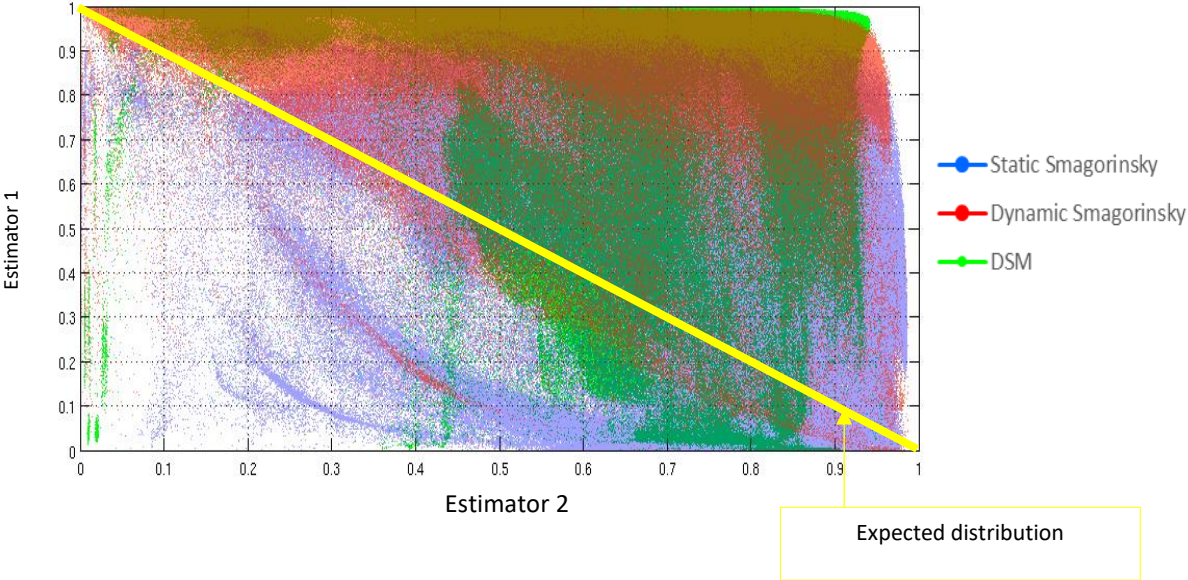


Figure 46 Scatter plot of estimator values on the whole domain for each SGS model

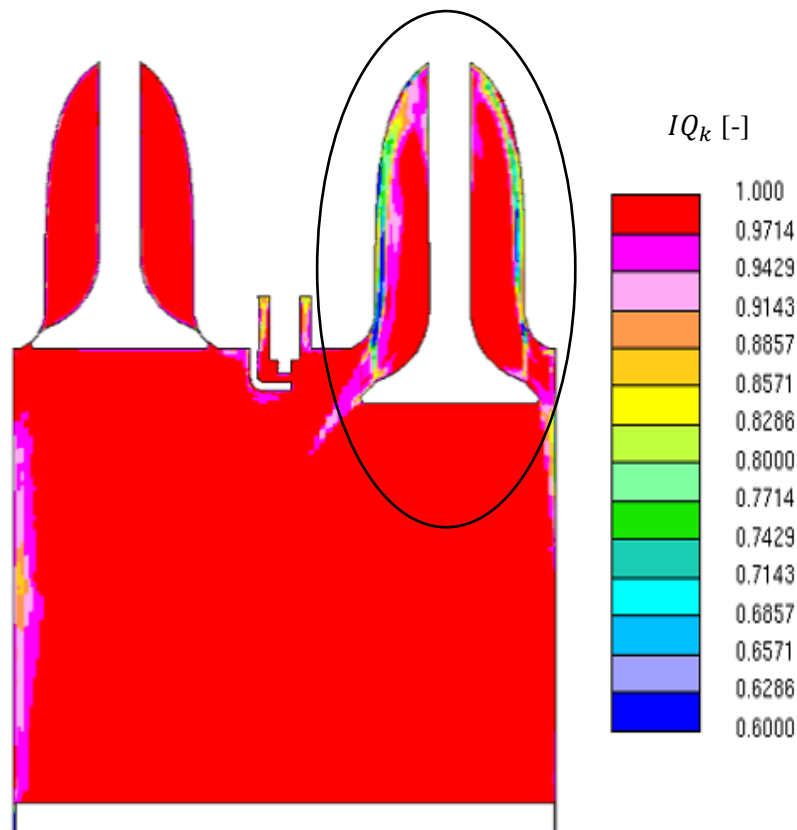


Figure 47 Estimator 1 on XZ plane for DSM model at 475 CA: values in the intake port area are lower than the in-cylinder ones.

The POD analysis confirms the findings of the previous analysis. The representation of the energy fraction for the first and the second POD modes, shown in Figure 48, gives an idea of the quality of the simulations over the intake and compression strokes. As mentioned in Section 3.3, the first POD mode represents the average flow field, while the second POD mode is the most intense contributor to the coherent structure responsible for the deviation from the average. Once again, the three SGS models seem to be equivalent, but the Dynamic Smagorinsky is slightly more accurate on both the first and the second POD modes. However, a lower variability for the less energetic modes can be noticed for all the SGS models during the intake stroke (from 440 to 480 CA). This confirms the higher penetration seen for all the SGS models in the 475 CA snapshot in Figure 42.

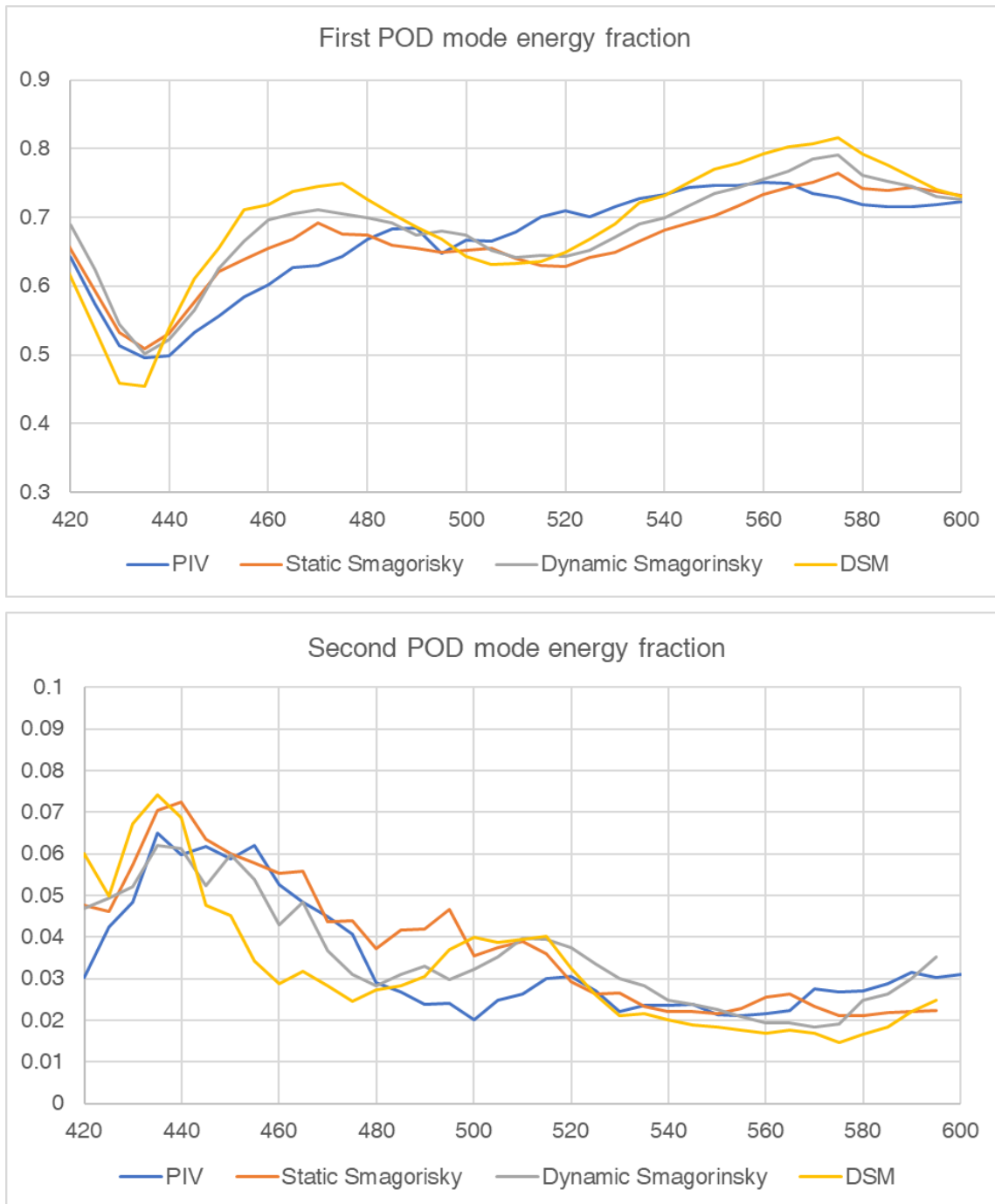


Figure 48 Energy fraction for the first and the second POD modes over the intake and compression stroke

The findings of the work presented in this section are summarized.

A ranking can be established among the SGS models in terms of mean LES quality indices, whose averaged values are reported in Table 3. According to the simulated cycles, both Dynamic Smagorinsky

and DSM models show high performance, while the lowest values are obtained for the static Smagorinsky model.

Despite a ranking in LES quality indices can be clearly established, all the SGS models seem to adequately represent the average flow field evolution. Similarly, all the models show an underestimation of the variability during the intake stroke. Since the LES estimators shows that the quality inside the cylinder is good enough, at least for Dynamic Smagorinsky and DSM, the main reason could be an under-resolution in the intake port. This is confirmed by the same LES estimator shown in Figure 47. To some extent, this observation seems to suggest that SGS closure plays a secondary role with reference to spatial resolution and near wall discretization. The synergistic use of LES quality indices, similarity indices with available experiments, average field observations and POD provides a deep insight into the CFD simulation outcomes and allow the researchers to find the best trade-off between computational cost and predictive capabilities of the LES simulations.

Chapter 5

LES Analysis using the Overset Mesh technique

The analysis presented in Section 4 shows that improvement could be made on the mesh, especially in the valve curtain zone and in the intake port. The meshing strategy plays a central role in the computational efficiency, in the management of the moving components of the engine and in the accuracy of results. In this section, the aim of improving the computational quality of the simulation was pursued in two ways: on one side, a computational scheme with a higher order was used; on the other side, the mesh quality has been enhanced with the adoption of the Overset mesh approach. The overset mesh approach, usually referred to also as Chimera grid or Composite grid, was rarely applied to the simulation of ICEs, mainly because of the difficulty in adapting the technique to the specific complexities of ICE flows. The work in this section demonstrates the feasibility and the effectiveness of the overset mesh technique application to ICEs thanks to a purposely designed meshing approach. 50 LES cycles were performed on the TCC-III engine in motored condition. Results are analyzed in terms of tumble center trajectory and using POD to objectively characterize the spatial and temporal evolution of turbulent flow field in ICEs. Furthermore, the POD quadruple decomposition introduced in Section 3.7 was extensively applied [84].

5.1 Overset Mesh

In the overset grid technique, the computational domain is covered by several grids (sub-domains) which overlap with each other in an arbitrary manner. Moving components (i.e. piston and valves in an ICE) are usually associated to individual sub-domains and they have dedicated grids. The combination of a background grid and each overlapping subdomain composes the computational domain, assembled by removing redundant cells. In the specific ICE application, it seems reasonable to assign the cylinder and the ports (together with the plenums in the specific case of the TCC-III engine) to the background static mesh. The valves and the piston, which are the moving components, are handled by dedicated grids [85]. Figure 49 shows the mesh topology of each component, i.e. background, valves, and piston on the TCC-III.

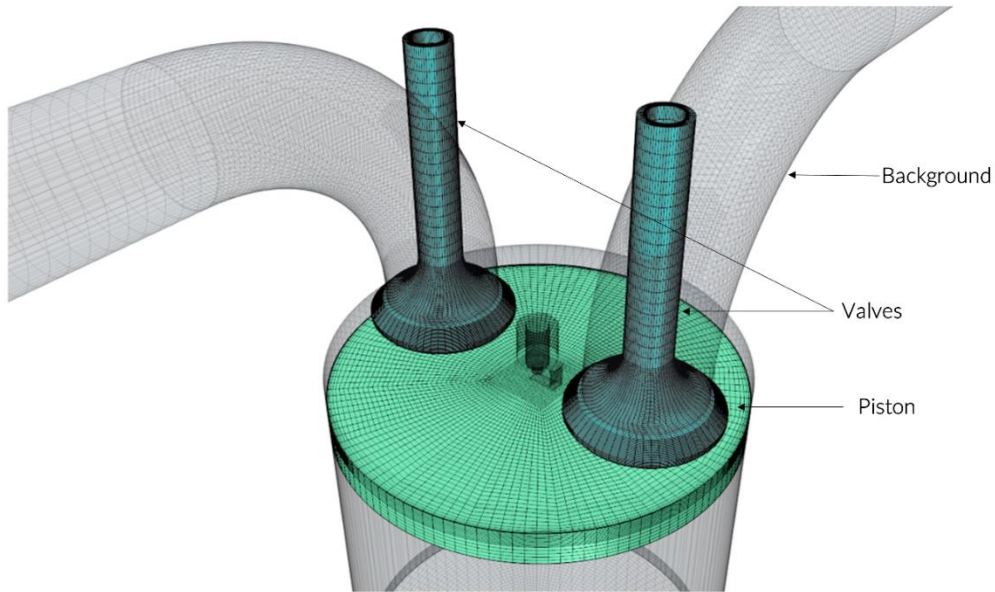


Figure 49 TCC assembled mesh: in transparency the background mesh of cylinder and ports; the valves mesh and the piston mesh for the overset technique

Two major steps are used to establish inter-grid communication:

- Hole cutting, that involves the identification of the cells outside of the computational domain
- Identification of interpolation stencils used to construct the interpolation formulas for grid coupling

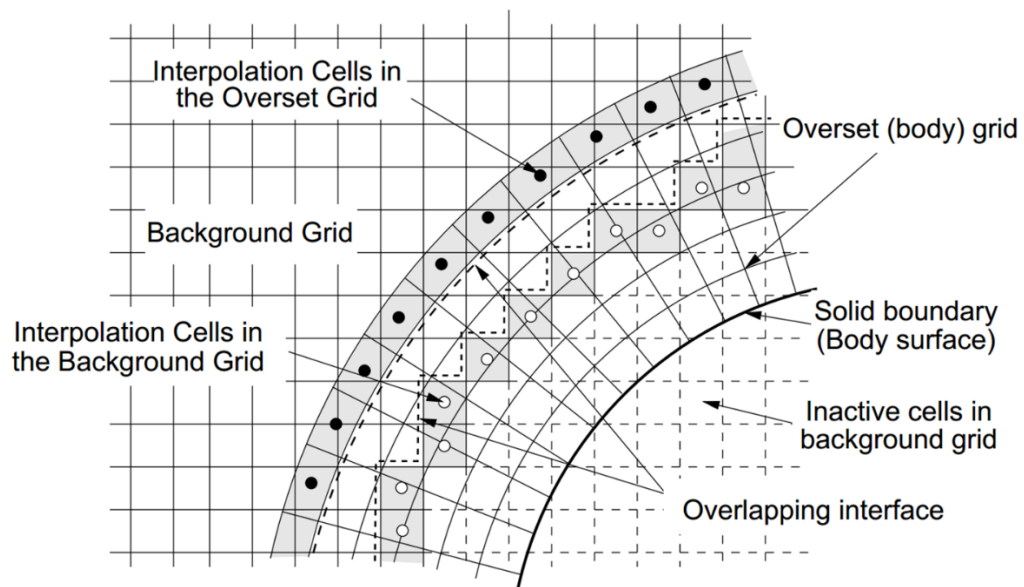


Figure 50 Detailed view of an overlapping zone for the overset technique, as reported in [85]

Figure 50 shows a detailed view of the overlapping zone for the overset mesh technique.

The cells in the overlapping zone can assume different roles: inactive, active, acceptor, donor. Active cells are part of the computational domain. All the boundary cells are identified as Active (e.g. the wall boundary identifying the valve surface). The cells lying along the outer boundary of the sub-domain region, identified as overlap boundary, are recognized as interpolation cells. Among these, the Donor cells are active cells whose values are used for the interpolation of the fluid dynamic variables with the Acceptor cells, which, conversely, are inactive. Finally, Inactive cells are not part of the computational domain, therefore no equations are solved for these last. For the specific ICE meshing strategy here adopted, in the closed valve position the mesh at the valve curtain is deactivated by means of the so-called “zero gap” submodel. Whenever the number of overlapping cells between the background mesh and any sub-domain mesh is less than an arbitrary value (in our case equal to 2), the cells become inactive. Figure 51 shows the cell sets of the background, the valve and the piston mesh.

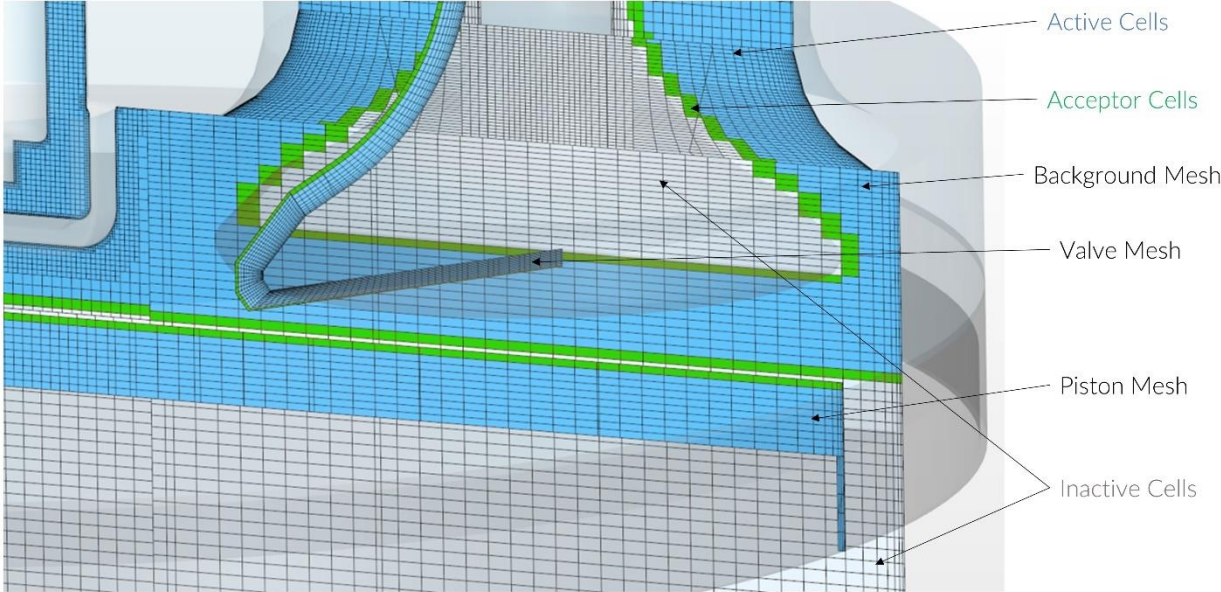


Figure 51 A multi-section view of the computational domain, with the identification of the Active, Inactive and Acceptor cells. Donor cells are not identified, they belong to the Active cells

For each acceptor cell, donor cells are found according to the chosen interpolation option. In this work a linear interpolation was used. Shape functions spanning a tetrahedron defined by centroids of the donor

cells are used in the interpolation of the fluid-dynamic quantities. Inactive cells are excluded from the computational domain. The solution is calculated on each grid in the overlapping zone. For each interpolation point in the grid, donor cells are selected and an interpolation stencil is established. After all donors are determined, an interpolation formula for each interpolation point can be constructed which, regardless of the shape function used, has the following form:

$$\phi_{P_i} = \sum_{k=1}^{N_D} \alpha_{w_k} \phi_{D_k} \quad [5.1]$$

expressing the interpolated function value at node P_i , ϕ_{P_i} , in terms of the function values at donor points D_k , ϕ_{D_k} , with α_{w_k} being the interpolation weights. Unfortunately, this process of interpolation is not conservative, and a strategy must be adopted to enforce mass conservation. Therefore, source term correction and flux correction are introduced in the pressure correction equation. Further information can be found in [85].

5.2 Numerical setup

5.2.1 Mesh

As stated earlier, the mesh was carefully designed to optimize the computational stability and speed of both the overset interpolation and the CFD solver. Following a trial and error process during which different grid topologies were analyzed (namely predominantly hexahedral, polyhedral and mixed grids), the best computational stability was found with structured meshes at the overlapping regions, where cell faces at the interfaces share the same orientation. Hybrid structured/hexahedral meshes for each of the overset sub-domains were therefore created and assembled: most of the background grid was generated using a flow-oriented so-called “butterfly” mesh, visible in Figure 49, obtained through the extrusion of a manually built 2D patch. The remaining sections of the ports were meshed with a predominantly hexahedral grid. The valves and the piston required a dedicated mesh: the same butterfly mesh topology of the cylinder was used for the piston, while an axisymmetric structured mesh was built for both the valves and the valve seats.

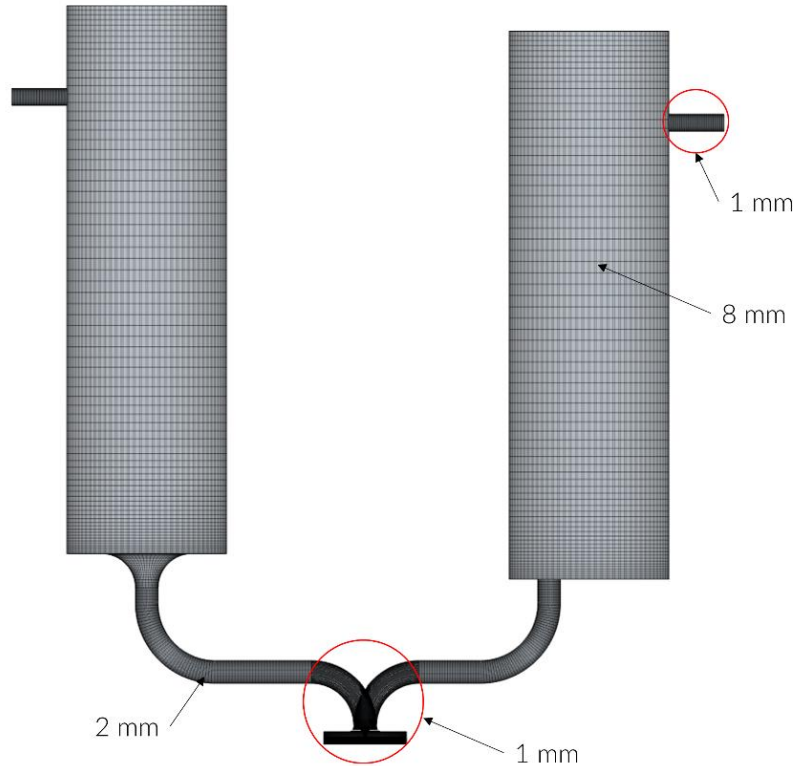


Figure 52 TCC-III computational domain with a particular focus on the average mesh characteristic dimension for each zone

The final overall number of cells is approximately 1.8 million, but the active cells at BDC are nearly 1.2 million. The average cell size in the cylinder is 1 mm, varying from a minimum of 0.1 mm near the liner to a maximum of 1.15 mm in the bulk volume. The mean value of the in-cylinder cell dimension is comparable to the mesh analyzed in Section 4. However, the mesh in the cylinder was refined in the region close to the TDC to reduce numerical diffusivity and minimize possible mass conservation errors, typical of the overset approach. The in-cylinder number of cells is approximately 0.8 million at BDC and 0.3 million at TDC. The use of a butterfly mesh reduced the number of cells in the plenums. The number of cells in each of the intake and exhaust plenums is 0.4 million. Compared to the mesh shown in Section 4, both intake and exhaust ports were refined in the proximity of the valves. The remaining sections of the ports were slightly coarsened to limit the computational cost, but the structured butterfly mesh is expected to optimize the quality of the volume discretization. Figure 52 shows the whole computational domain and the characteristic mesh size of each zone. As stated before, the mesh was purposely built to reduce the computational time while increasing stability of the solution in the extremely small gaps at valve opening and closing events. The required level of accuracy imposed the adoption of a highly refined mesh in the valve curtain zone. This also fulfilled the necessity of a finer

mesh in this zone highlighted in Section 4. Figure 53 shows a detailed view of the mesh topology in the cylinder and in the valve curtain zones.

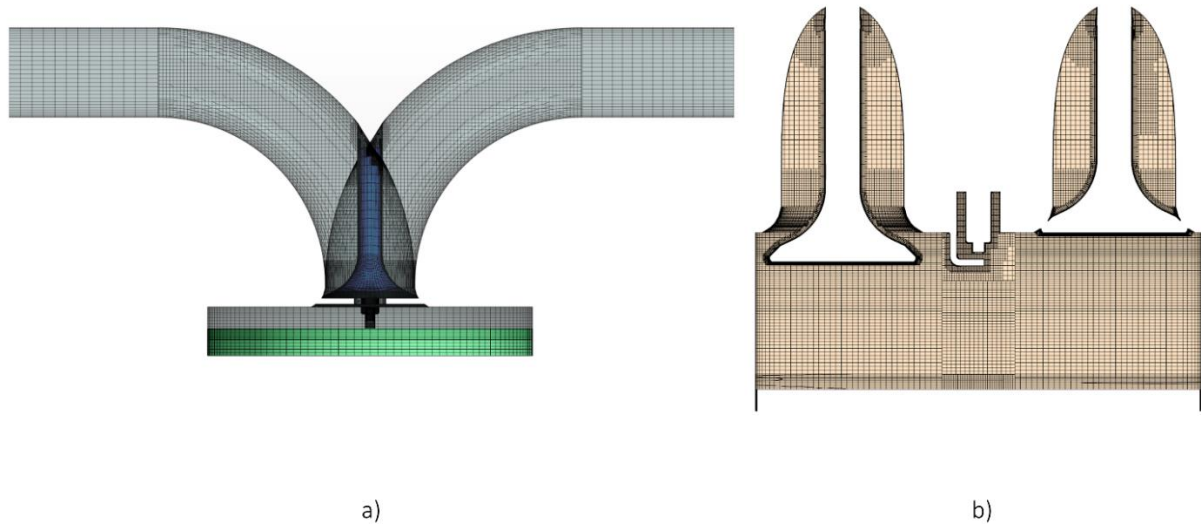


Figure 53 Detailed view of the in-cylinder mesh. The zero gap is active in a) and in the intake valve in b) and the cells at the valve curtain are deactivated. The exhaust valve in b) is open and the mesh topology of the valve curtain is shown.

5.2.2 Boundary layer mesh approach

The main advantage of the overset mesh technique is the strict control of the mesh at the boundaries, which is not subject to morphing or remeshing. One of the most critical events are the opening and closing of the valves, where high velocity and pressure gradients arise in presence of small gaps. To ensure sufficient cell quality and stability of the simulations, a minimum gap at the valve opening is imposed below which the cylinder domain is disconnected from the ports. In the present analysis, such gap is kept equal to 0.1 mm. Local refinements at the valve curtains are introduced in order to provide sufficient resolution at the early opening at late closing stages. The literature agrees on the link between the accuracy of the results and the level of the refinement of the mesh in the valve curtain zone. For example, in [86] Buhl et al. investigate different port modeling strategies, highlighting the importance of an accurate mesh to properly match cycle-to-cycle variations. Furthermore, Barbato et al. [87] showed how using a low-Reynolds approach, resulting in a better and more structured mesh in the valve curtain zone, substantially improved the quality of the CFD representation of the in-cylinder tumble formation. In Figure 54 three different configurations of the mesh during the valve opening are shown.

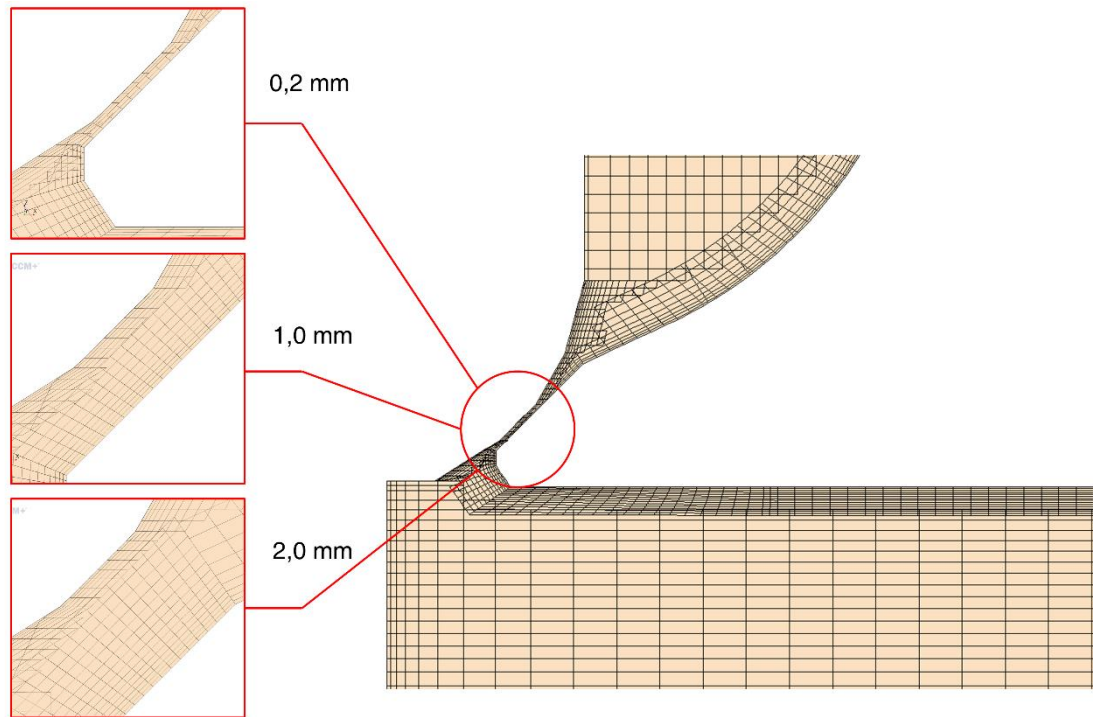


Figure 54 Detailed view of the mesh at the valve curtain during the opening phase

5.2.3 Computational Setup

In this study, 50 perturbed LES cycles were run using the 3D-CFD code STAR-CCM+ v13.02, licensed by SIEMENS PLM. Three RANS cycles with the same mesh setup used for LES were run to initialize the flow field. 5 LES cycles were then run using the RANS fields as initial conditions. 5 batteries of 11 cycles each were finally generated perturbing the initial conditions via the addition of a synthetic turbulent spectrum. The first LES full cycle of each sequence was discarded and 10 consecutive cycles from each perturbation constitute therefore the database presented in the following paragraphs. The discretization in time is performed using an implicit unsteady model (2nd order). The timestep was defined according to the Courant constraints and refined to improve the convergence of the overset mesh approach around the valve openings, which are critical phases of the cycle for the overset simulation due to the management of the zero-gap zones. Starting from the findings of Section 4, the chosen subgrid model is the Dynamic Smagorinsky one. The spatial differencing scheme is a hybrid 3rd order/central-differencing scheme called MUSCL. It uses a Normalized-Variable Diagram (NVD) value ζ to ensure the boundedness of the scheme by switching to a first-order scheme in regions of non-smooth flows. When smooth local flow conditions are detected, the scheme is constructed as a blend between a MUSCL 3rd-order upwind and the 2nd-order central-differencing reconstruction schemes.

The Ideal Gas equation of state is employed to compute density and its derivatives as a function of temperature and pressure. Sutherland's law is used for the Dynamic Viscosity. A calibrated 1D model of the TCC-III engine using GT-Power was used for time-dependent periodic boundary conditions. The use of cycle-independent boundary conditions is deemed to have a negligible impact on the ability to simulate cycle variability in the cylinder because of the presence of the two big plenums in the intake and exhaust line.

5.3 Results

The same three CA positions are shown, i.e. 475, 540 and 630 CA. The simulation correctly reproduces the flow field topology, both qualitatively and quantitatively. The intake jet in Figure 55 a), has a slightly higher penetration, but the intake jet bending is accurately captured, as well as the vortex center. The same can be observed for the tumble center in Figure 55 b). In Figure 55 c) LES shows a higher recirculation. By analyzing the alignment parameter, in Figure 56, a high level of alignment can be observed over the whole FOV in all the considered CAs. The only misalignments are located in the vortex centers, where velocities are almost null. Figure 57 shows an analysis of the LES quality estimators, described in Section 4.2. Comparing these results to the dynamic Smagorinsky ones in Figure 44 and Figure 45, a better quality of the LES can be denoted. In particular, the energy resolution reaches very high values over the whole domain. A similar result was obtained in Section 4 with the DSM SGS model. This is concurrently due to a higher order of the spatial differencing scheme and an improved quality of the overall spatial discretization. The viscosity ratio still shows relatively high values in presence of high gradients (475 CA), but, in this case too, the overall values are better than the ones obtained in the previous analysis.

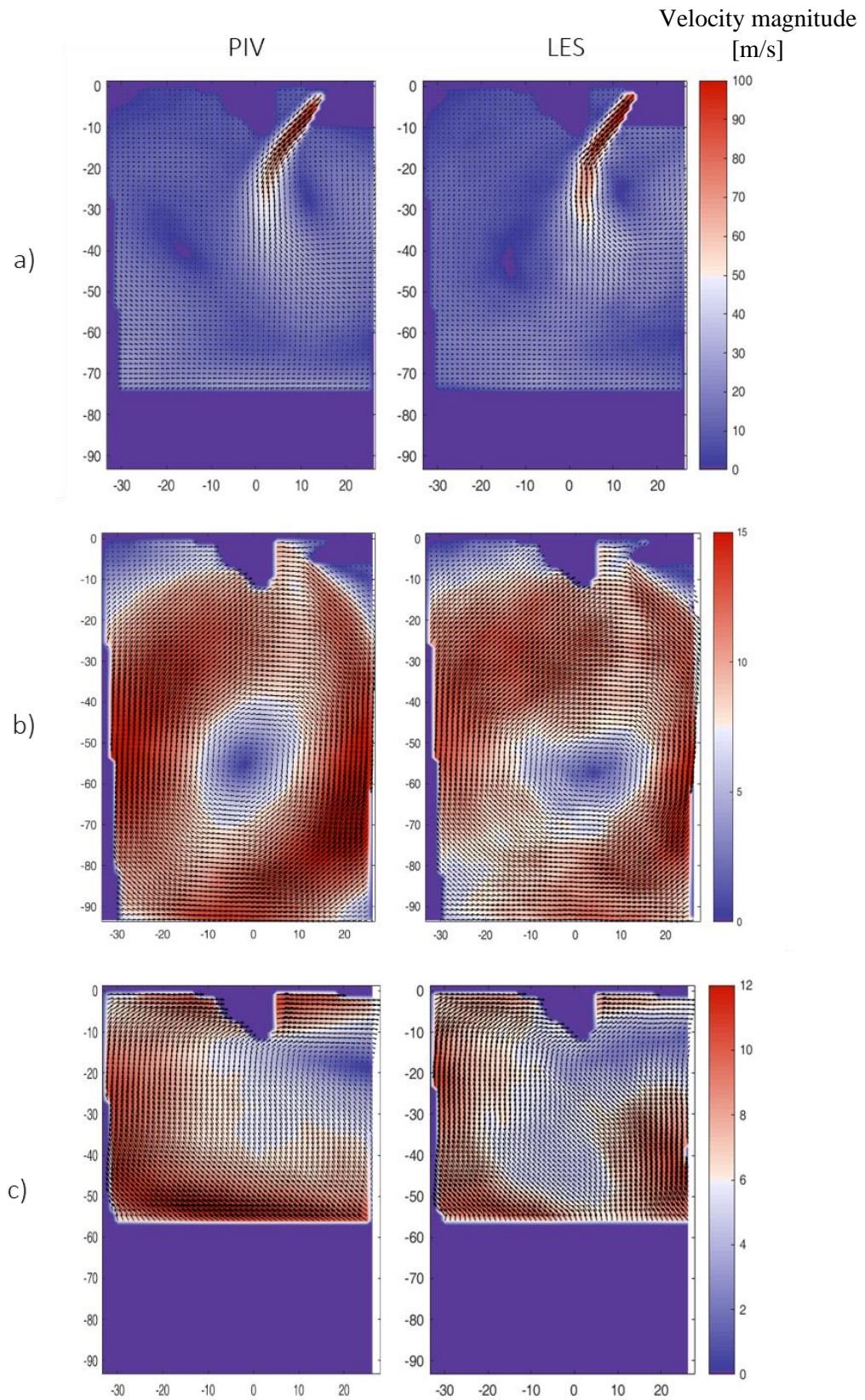


Figure 55 Ensemble average of the velocity field over the XZ plane at CA position (a) 475, (b) 540 and (c) 630 for experimental PIV and calculated LES

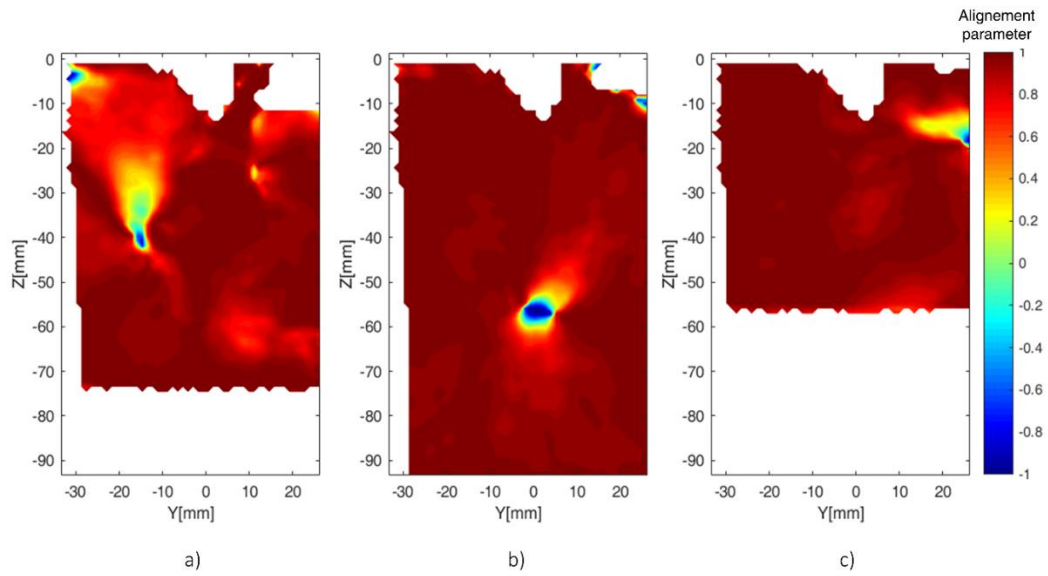


Figure 56 Alignment parameter for CA position (a) 475, (b) 540 and (c) 630

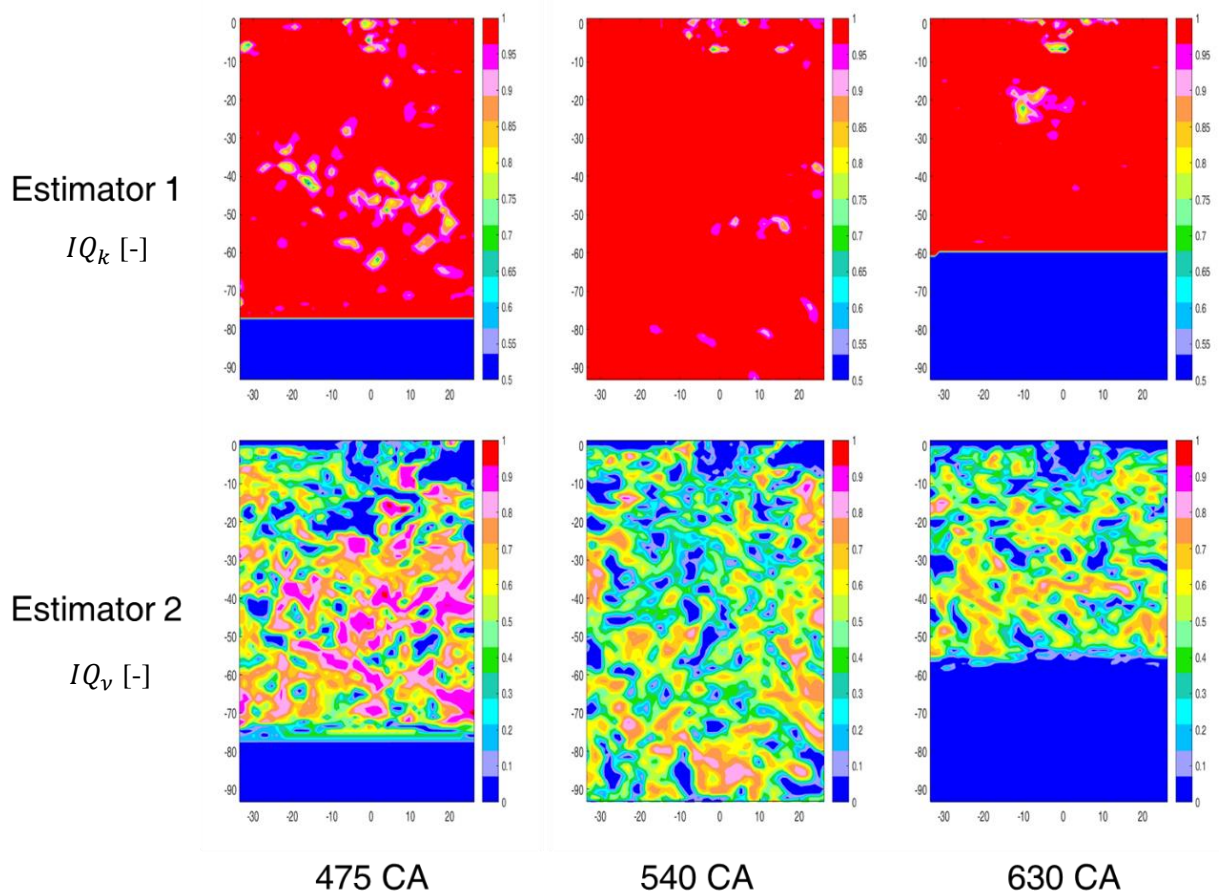


Figure 57 Estimators 1 and 2 on the analyzed CA position 475, 540 and 630

Figure 58 shows the comparison of the root mean square deviation (RMSd) of the velocity fields. Even though the distribution of the deviation is not perfectly equal (see the left zone of the FOV), the quantitative estimation is analogous. To justify the high variability in the curtain zone of the PIV a look has to be taken to the experimental snapshots. For example, Figure 59 shows two snapshots for cycles with superimposable traces of in cylinder pressure and intake port, visible in Figure 60. The velocity values in the proximity of the valve are extremely different. It is reasonable to think that the velocity at the valve curtain in the immediate proximity of the valve during the mid-intake stroke should be very high in each cycle. In cycle 178, in Figure 59 a), in the valve curtain zone the expected high velocities are visible. In cycle 240, however, in Figure 59 b), the velocity in that area is extremely low while a sudden recover is visible above. On one side, this could suggest the presence of strong recirculation vortices that split the intake flow over the section plane. On the other side, a highly swirling motion could be present in the intake port, causing a bending in the intake jet flow, which does not strike the section plane. However, as it will be shown later on, both these phenomena are simulated. The effects on the intake jet are visible only at the early stages of the intake stroke, and they do not affect the valve curtain velocity at the peak of the mass flow rate. The CFD data extrapolated on the PIV grid show repeatability of the velocity in the proximity of the valve curtain, therefore the RMSd value is low, because low variability is detected. The reason of such discrepancy is still to be clarified. The difficulty in capturing the experimental data in the valve curtain zone must not be underestimated, and it is possible that the few cycles responsible for the high variability in the RMSd value could be affected by local uncertainties.

Despite the underestimation in the valve curtain zone, the RMSd value of the intake jet bending and penetration is both quantitatively and qualitatively accurate. Such similarity between experimental and simulated data demonstrates LES capability of capturing the CCV.

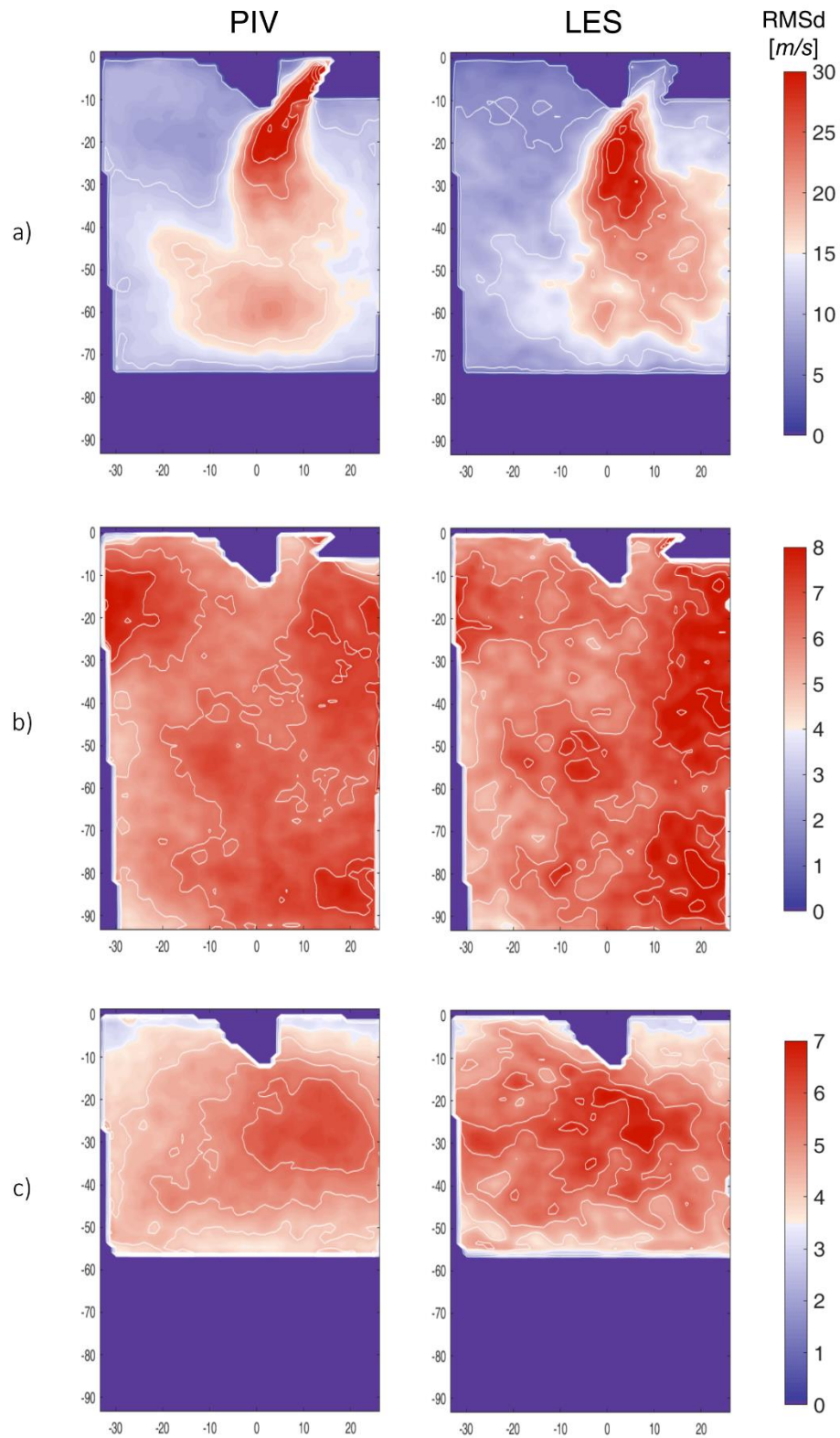


Figure 58 RMSd of the velocity on the XZ plane at the CA positions (a) 475, (b) 540, (c) 630 for experimental PIV and LES

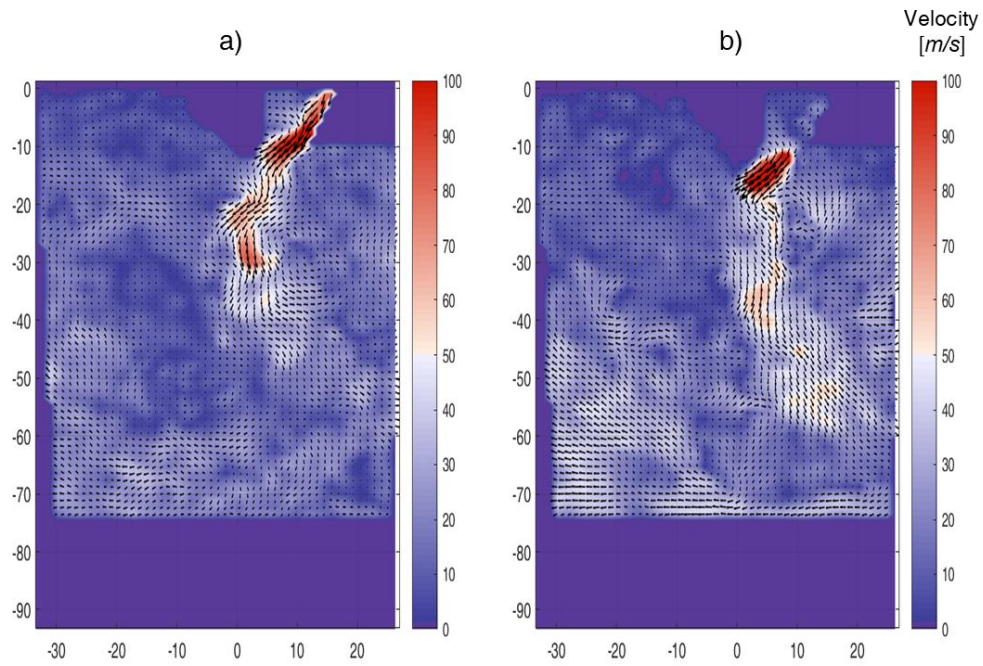


Figure 59 Snapshots at 475 CA for PIV cycle (a) 178 and (b) 240

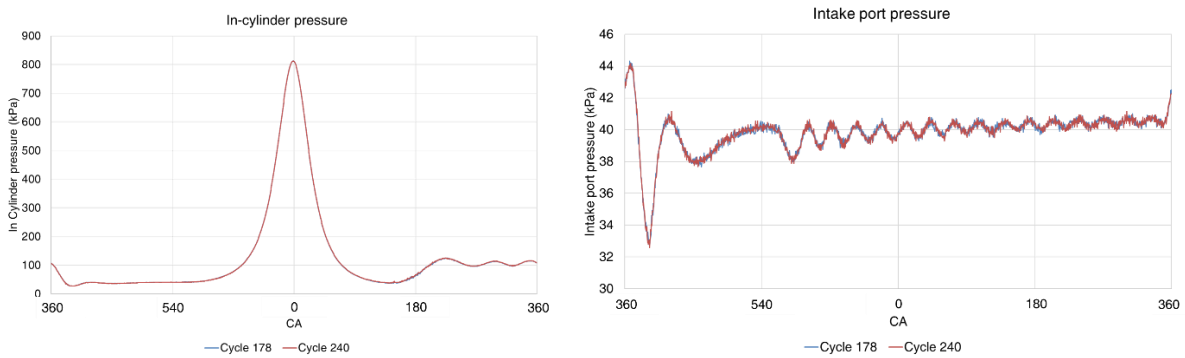


Figure 60 In cylinder and intake port pressure traces from PIV cycles 178 and 240

The mass conservation error was verified a posteriori. The most critical phase of the cycle for the mass conservation is the compression phase, where the cylinder is a closed volume with pressure rising. The maximum oscillation of the in-cylinder mass during the compression phase, is equivalent to 0.2%. The maximum amplitude of the oscillation takes place exactly at the TDC. Despite the oscillation during the

compression phase, the in-cylinder mass per simulated cycle is conserved. Figure 61 shows the conservation error over one cycle.

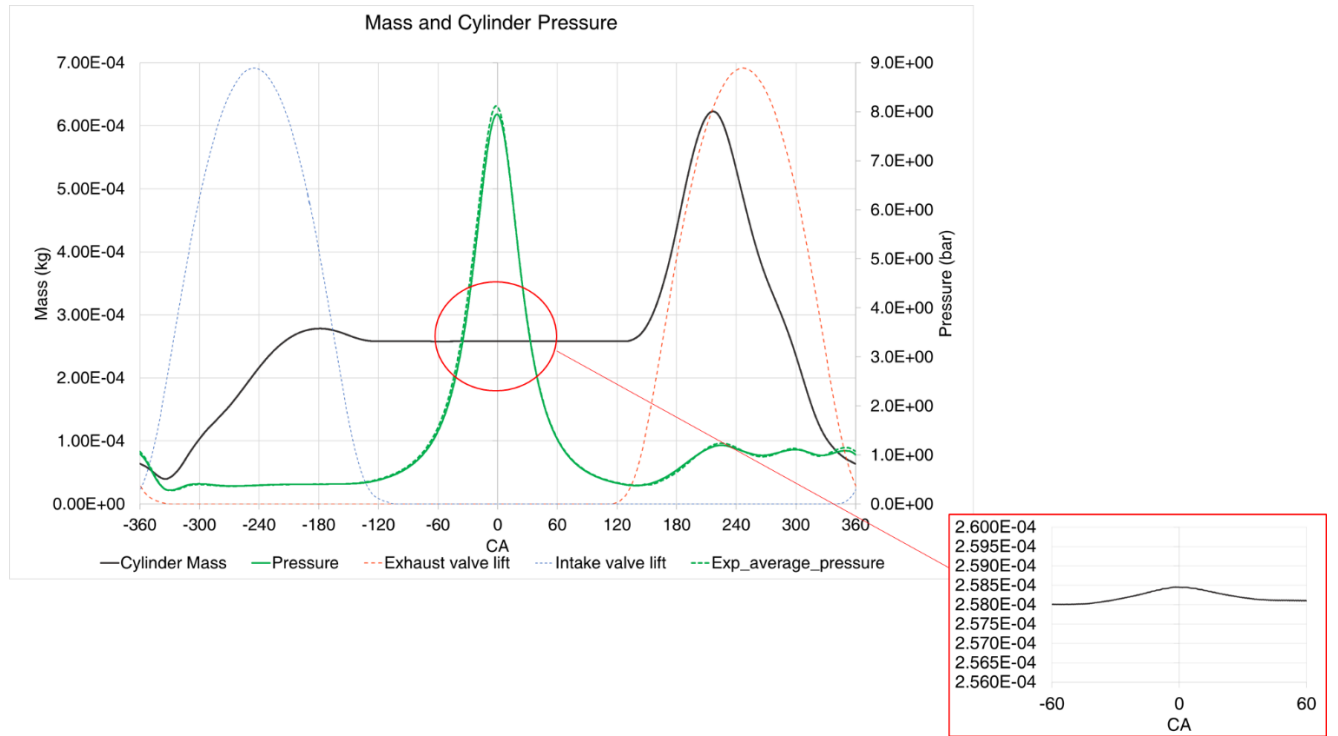


Figure 61 Mass and pressure of one LES cycle, with a detailed view of the mass conservation error at TDC

5.3.1 Tumble Center

A quantitative evaluation of the accuracy of the analysis over the whole intake stroke can be obtained by the analysis of the tumble center position. An algorithm to identify the center of recirculation vortices in a flow was developed by Graftieaux et al. [53] and applied to ICes by Stansfield et al. [88]. For each grid point, Eq. 5.2 is applied. The algorithm calculates the sine of the angle between the positional vector of each of the surrounding eight grid points, \bar{M} , and the corresponding velocity vector, \bar{U} , as shown in Figure 62. The vortex center identification is performed where the value of R reaches unity.

$$Vortex\ identifier\ R(n) = \frac{1}{N} \sum_s \frac{(\bar{M} \wedge \bar{U}) \cdot \hat{z}}{\|\bar{M}\| \|\bar{U}\|} = \frac{1}{N} \sum_s \sin(\theta) \quad [5.2]$$

Where:

- R dimensionless scalar
- n grid point
- S 2D area surrounding n

- N number of points inside S
- Λ cross product
- \bar{M} radius vector
- \bar{U} velocity vector
- \hat{z} unit vector normal to the measurement plane
- θ angle between \bar{U} and \bar{M}

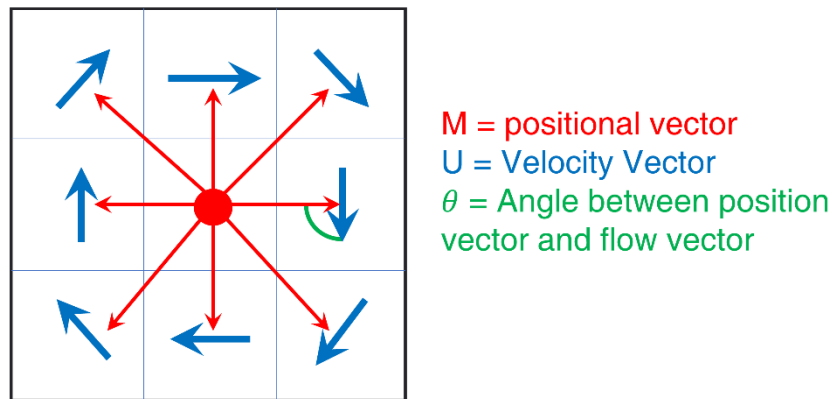


Figure 62 Visual explanation of the method for the vortex center identification

The author chose to perform a two-level comparison: first, to highlight the trend of the evolution of the tumble center, the position of the tumble center of the average flow field is shown. Secondly, the standard deviation of the position on 50 cycles is shown for the tumble center corresponding to each CA position.

The results of the method application are shown in Figure 63. Each pointer identifies the mean position of the tumble center for the CA position corresponding to the associated color, with 5 CA resolution as from PIV dataset. The ellipse surrounding each pointer represents the standard deviation of the X and Z position of the tumble center over all the cycles, as shown in Figure 64.

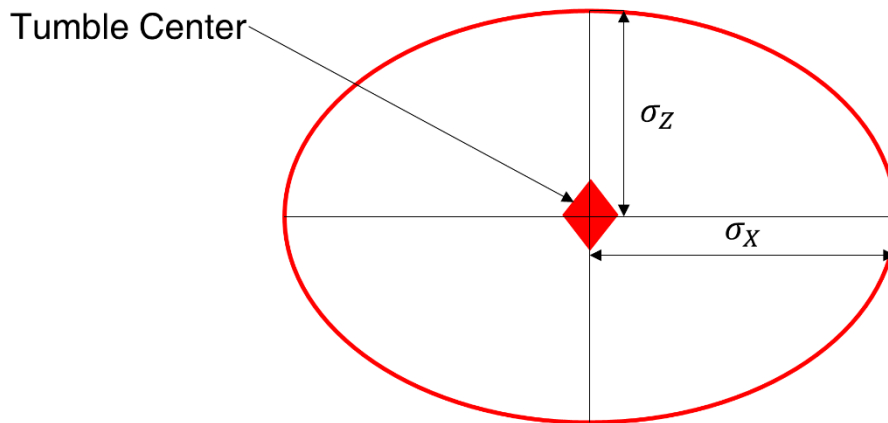


Figure 63 Tumble center and X and Z standard deviation representations

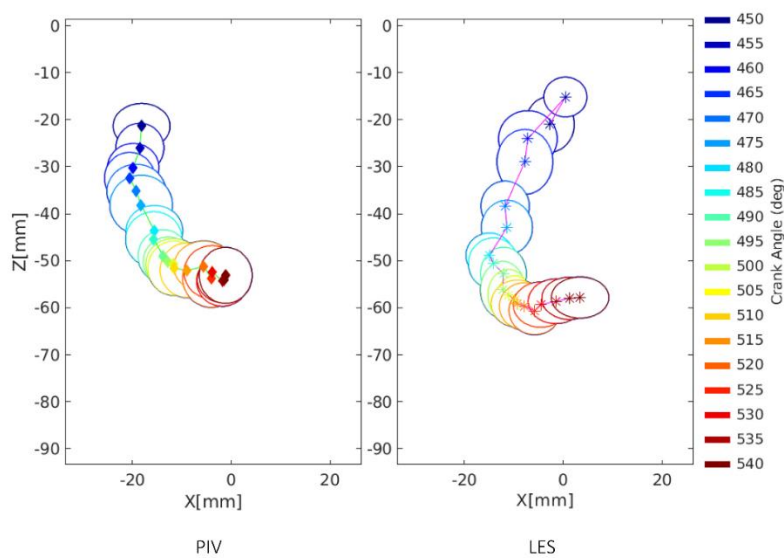


Figure 64 Tumble center identification for PIV and LES from 450 CA to 540 CA

The evolution of the tumble center over the whole intake stroke allows a better understanding of the evolution of the flow topology. The main tumble vortex in LES simulation shows a misalignment with the PIV in the very early stages, recovering around 470CA. In the proximity of the BDC the tumble center is slightly lower than the experimental counterpart, varying more along the X dimension. With these exceptions, the flow field evolution is well captured both in terms of pattern and variability of the X and Z position.

5.3.2 POD results

The POD analysis was conducted over both the full 240 experimental cycles and the 50 simulated cycles. Theoretically, the energy associated with each snapshot is split among all the modes, from the most to the least energetic. Dividing the energy in 240 cycles or in 50 cycles may affect the comparison between experimental and calculated results. However, negligible differences between the energy spectra can be spotted in the most energetic modes, as shown in Figure 65.

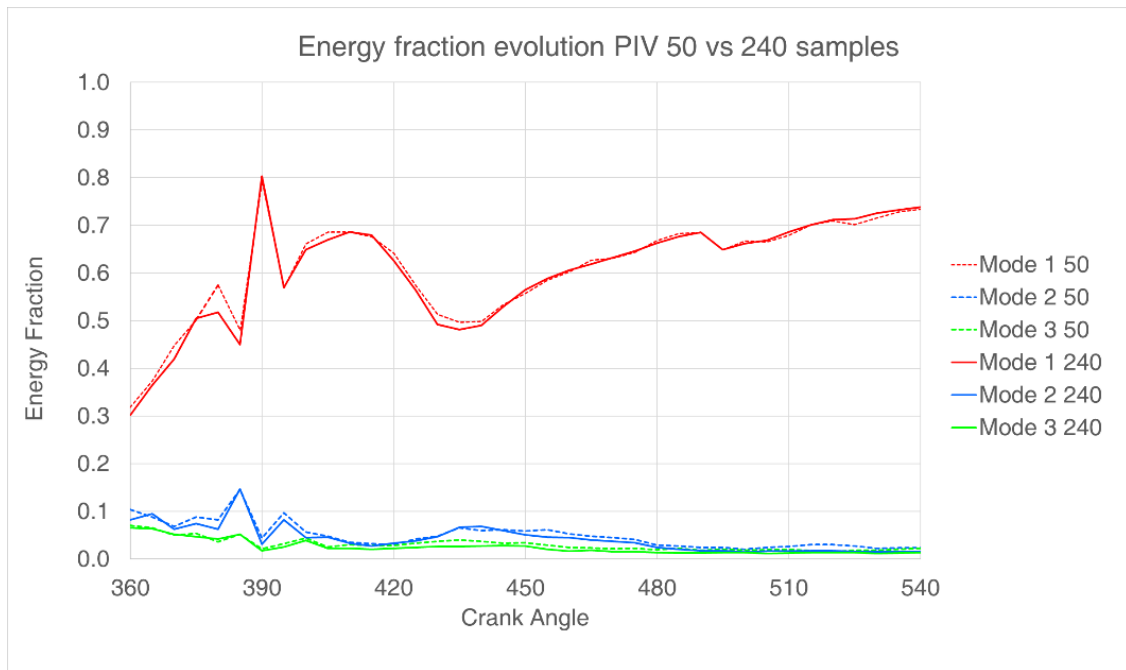


Figure 65 Energy spectrum comparison for POD modes 1,2 and 3 between 240 and 50 PIV cycles

The main differences can be found in the less energetic modes, where energy is more fractionized. Performing the POD analysis on just 50 experimental cycles would have introduced a degree of arbitrariness. For such reason, all 240 measured cycles were used. A phase independent POD analysis was applied. Figure 66 shows the comparison among the most energetic modes of both PIV and calculated cycles. Both trends and individual magnitudes show a good agreement. The comparison with the same analysis performed on the Dynamic Smagorinsky dataset from Section 4, in Figure 67, shows an improvement, especially in the first part of the stroke for both Mode 1 and 2. This is mainly due to the valve curtain refinement, whose effects are particularly effective in the first part of the intake stroke.

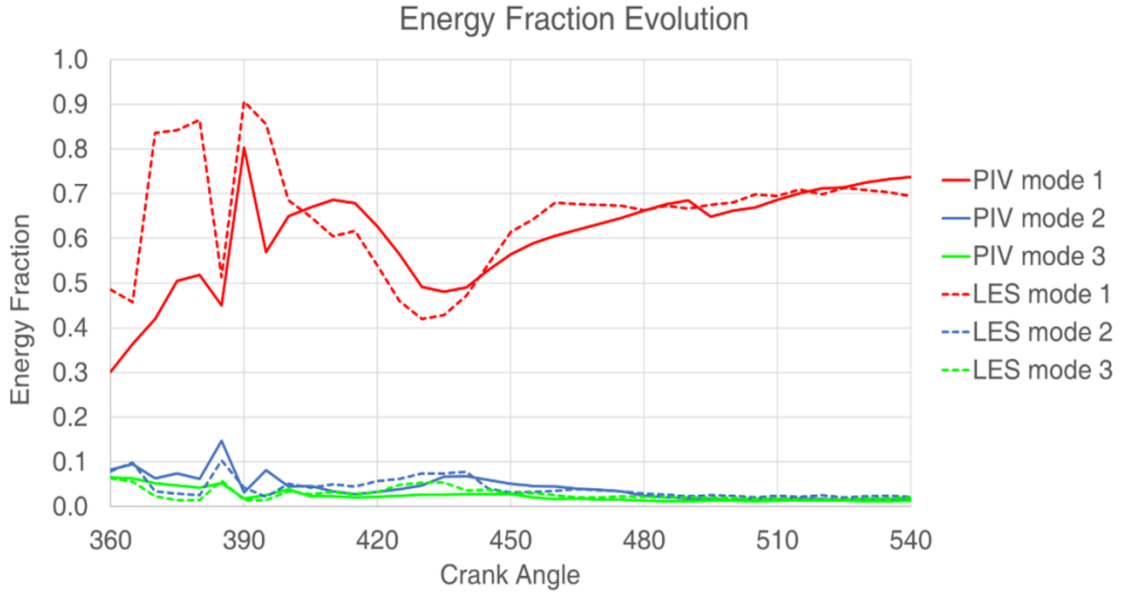


Figure 66 POD energy fraction comparison between LES and PIV for mode 1, 2 and 3

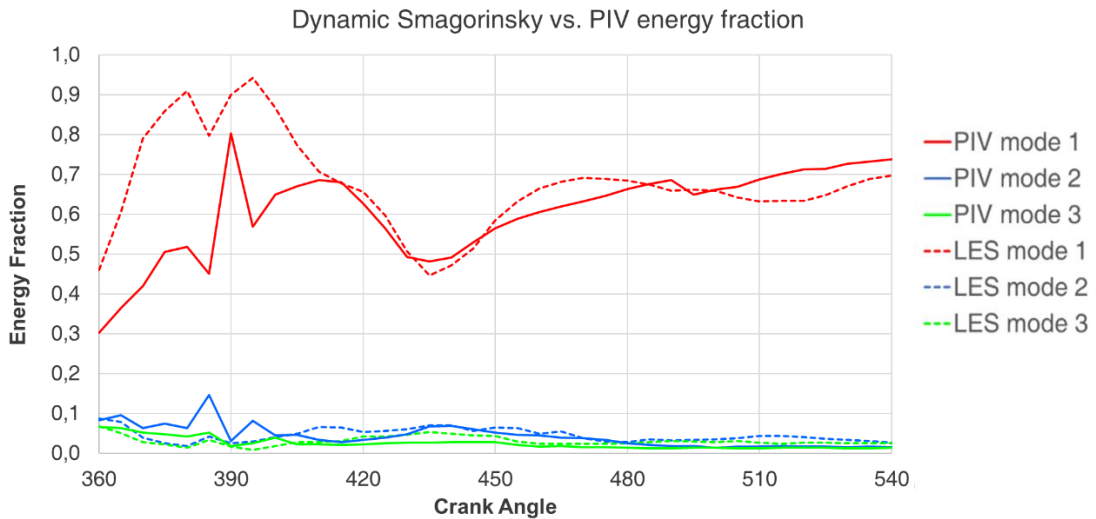


Figure 67 POD energy fraction comparison between LES Dynamic Smagorinsky from Section 4 and PIV

The quantitative result shown in Figure 66 can be qualitatively confirmed by comparing the POD modes, as shown in Figure 68. Even though the energy seems to be differently distributed among modes 2 and 3, the topology of the turbulent structure described by the modes is very similar. Mode 2, in Figure 68 (2), is the one showing the greatest differences, especially in the lower left zone of the FOV. The second mode is a representation of the second highest energetic turbulent structure, and it can be noticed that this difference is strictly related to the one noticed in the RMSd in Figure 58 (b).

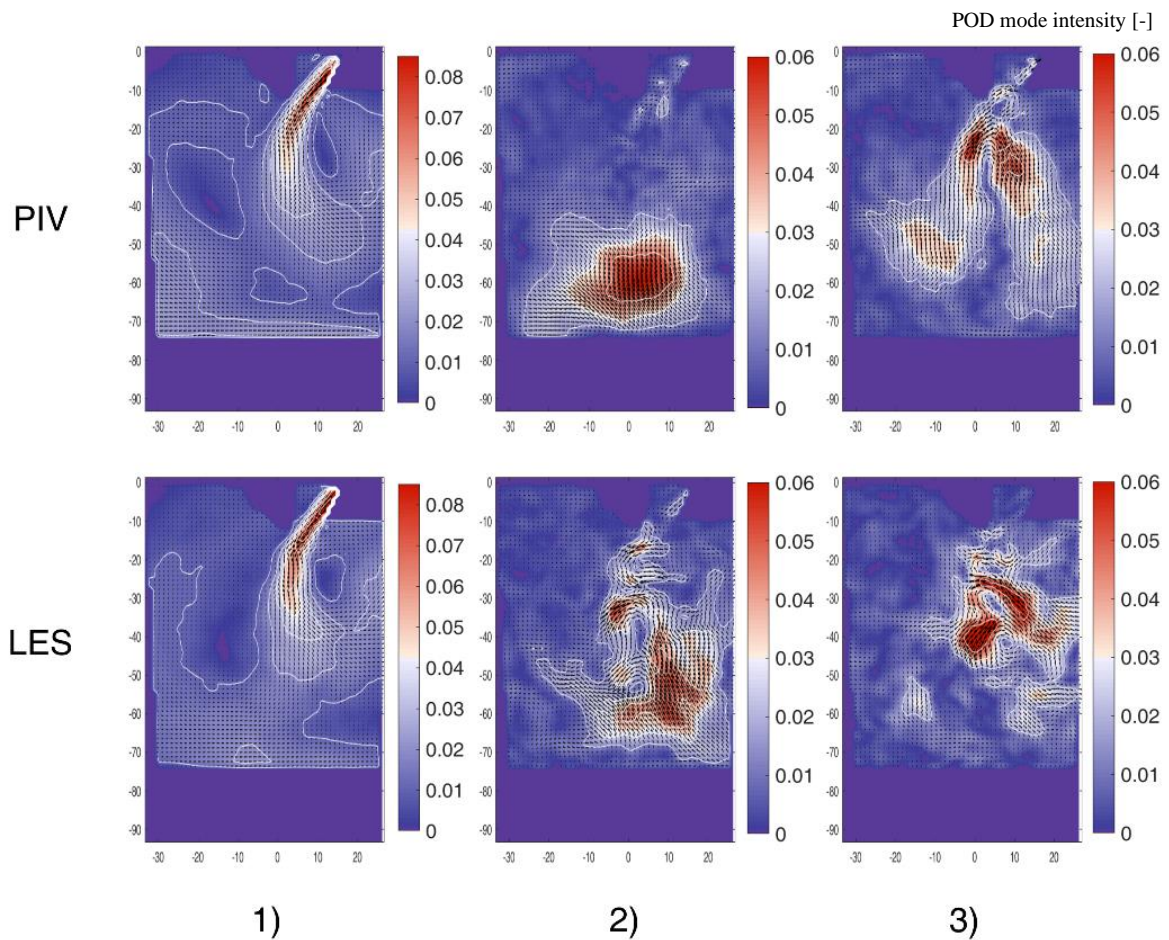


Figure 68 Most energetic POD modes (1, 2 and 3) comparison between PIV and LES

5.3.3 POD quadruple decomposition results

The POD decomposition introduced in Section 3.7 is here applied to both the LES and the PIV datasets. As already mentioned in Section 3, this tool can be used to perform a deeper analysis on the nature of the turbulent structures that cause the deviation from the mean flow field. Figure 69 shows the energy associated with mean, coherent, transition and incoherent parts, calculated as in Eq. 3.41, for all the 50 LES cycles in the CA position 475. The variability can be noticed mainly in the energy associated with the mean part and with the coherent part. The level of energy associated with the mean part is always high because of the predominant turbulent structure in the chosen 475 CA position, i.e. the intake jet flow. A high deviation from the average can be noted: the highest peaks represent the least deviating cycles, while the lowest ones represent the cycles that deviate the most from the average. In these last, the energy associated with the coherent part is higher, meaning that a high level of energy is dissipated in highly energetic turbulent structures different from the intake jet flow.

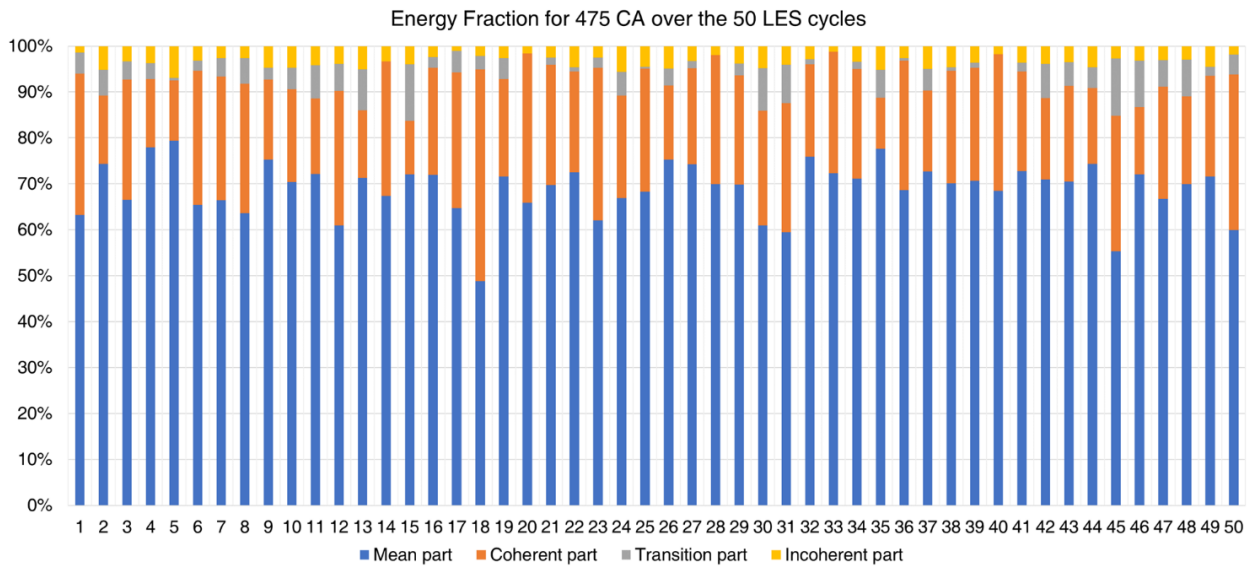


Figure 69 Energy associated with mean part, coherent part, transition part and incoherent part for the 50 LES cycles for the 475 CA position

Using the same methodology on the first 50 cycles in the PIV dataset, a comparison between the LES and PIV cycles that are the least and most deviating from the average field was performed. The energy spectra associated with the selected cycles are shown in Figure 70.

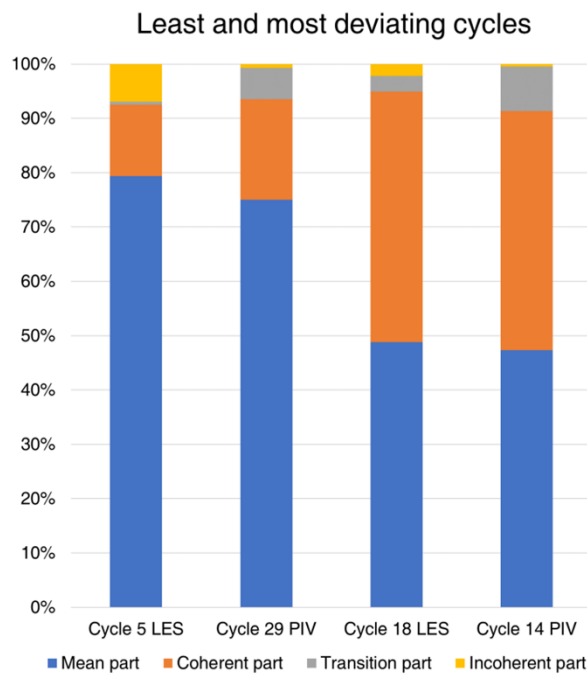


Figure 70 Energy spectra showing the contribution of each part of the turbulent field for the least (cycle 5 for LES and cycle 29 for PIV) and the most (cycle 18 for LES and cycle 14 for PIV) deviating cycles for LES and PIV

A visual representation of the selected cycles is shown in Figure 71.

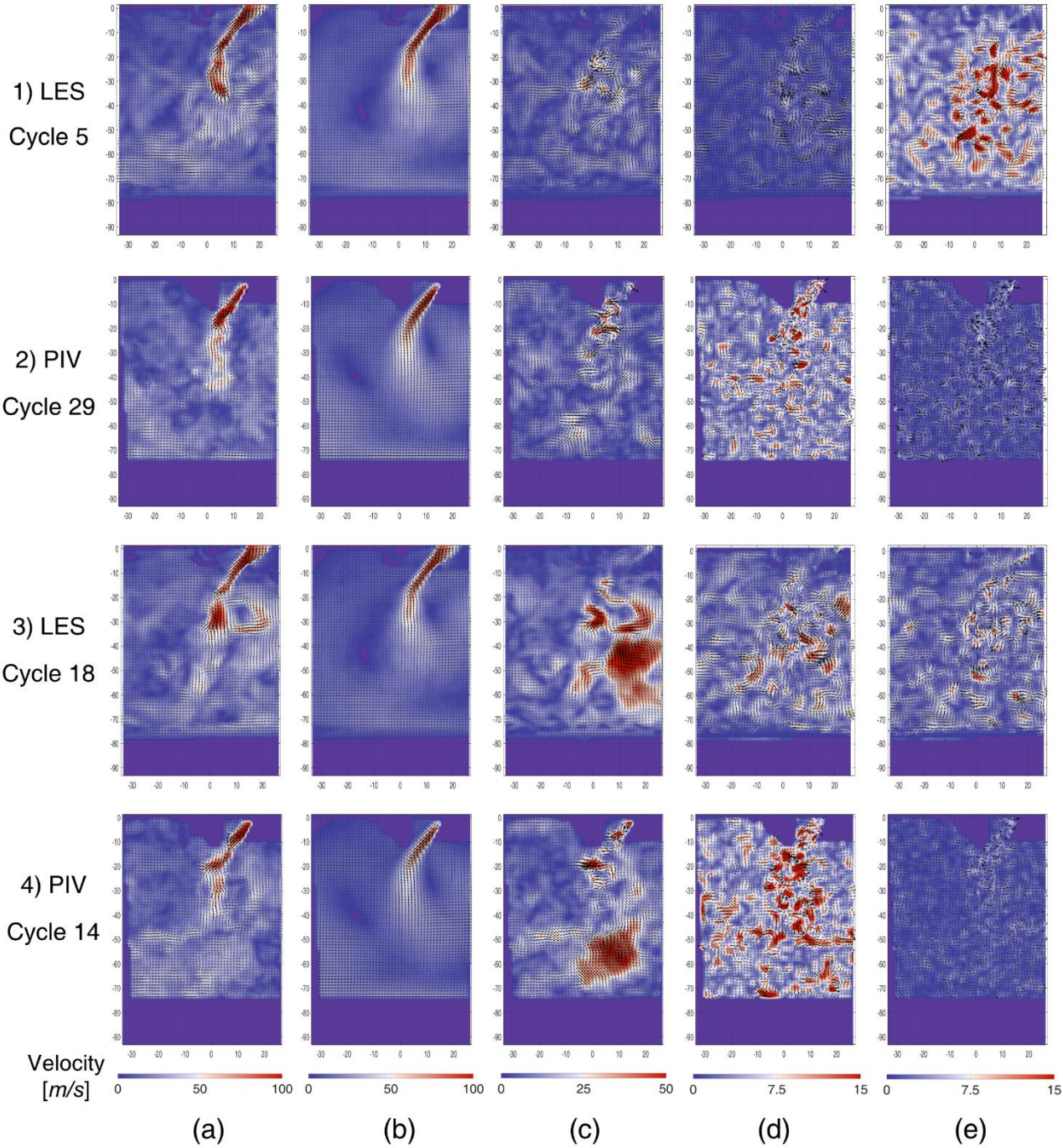


Figure 71 Comparison between the least deviating cycles (cycle 5 for LES and cycle 29 for PIV) and the most deviating cycles (cycle 18 for LES and cycle 14 for PIV)

Even though the instantaneous flow fields of all the considered cycles do not show significant differences, the quadruple analysis allows a deep insight of the dominant turbulent structures, especially

the ones responsible for the highest deviation from the average flow field. These are shown in Figure 71 3 c) and 4 c). The transition and the incoherent parts show a different distribution of energy. As stated in Section 3.7, the author believes that the combination of these two parts would not affect the accuracy of the analysis. The different distribution can be addressed to the different size of the available datasets for LES and PIV (50 LES cycles and on 240 PIV cycles). As stated before, Figure 65 demonstrated that the energy fraction of the most energetic POD modes doesn't show significant differences on the analysis made over 50 and 240 cycles. The effect of the analysis on a wider dataset is that the energy is fractionized in the lowest modes. The quadruple analysis performs a deep insight on the main vortex dimension on these very lowest modes, therefore a higher discretization leads to a finer analysis. This can be noticed by looking at the incoherent parts of LES and PIV in Figure 71 e): the PIV main vortex dimension is lower than the LES one. However, the amount of energy associated with the combination of transition and incoherent parts are quantitatively comparable, meaning that the lower discretization deriving from the less extensive LES dataset does not affect the recognition of the high energetic turbulent structures, responsible for the CCV. Figure 71 1 c) and 2 c) show the comparison of the coherent part of the turbulence in the less variable LES and PIV cycles. The energy associated with these structures is low, yet not negligible. Theoretically, a reduction of the CCV should lead to a reduction of the energy associated with these turbulent structures.

The analysis of the POD quadruple decomposition can be furtherly deepened: an analysis of the intake stroke relative to the most deviating cycles is proposed. The purpose of this analysis is not to reach definitive conclusions, but to propose a methodology to understand the origin of the turbulent structures responsible for both the "positive" and the "negative" deviations. The aim to reduce the CCV, should in fact lead to the maximization of the amount of energy associated with the mean part. For this reason, it is interesting to analyze also the least deviating cycles.

Among all the cycles, whose decomposition is visible in Figure 69, 6 cycles are selected: cycle 4, 5 and 35 are selected as the least deviating thanks to the high energy associated with the mean part and the low energy associated with the coherent part. On the contrary, cycles 18, 31 and 45 are selected as the most deviating ones.

Figure 72 shows the application of the POD quadruple decomposition to the intake stroke for the selected cycles. For clarity, only the evolution of the energy associated with the mean and the coherent parts is shown. A clear trend cannot be recognized between the least and the most deviating cycles. In particular, until 425 CA all cycles show a similar behavior. After this CA position, the evolution of the coherent energy is different: a progressive decrease is shown in the least deviating cycles. For the most deviating cycles, two different behaviors are detected: in cycles 31 and 45 the coherent energy decreases until 450 CA and then rises again, while in cycle shows 18 a progressive increase since the beginning of the intake

stroke. The 425 CA position seems to be a turning point in the cycle. To investigate the reason, Figure 73 shows the instantaneous flow field and the coherent part for these cycles at the 425 CA position.

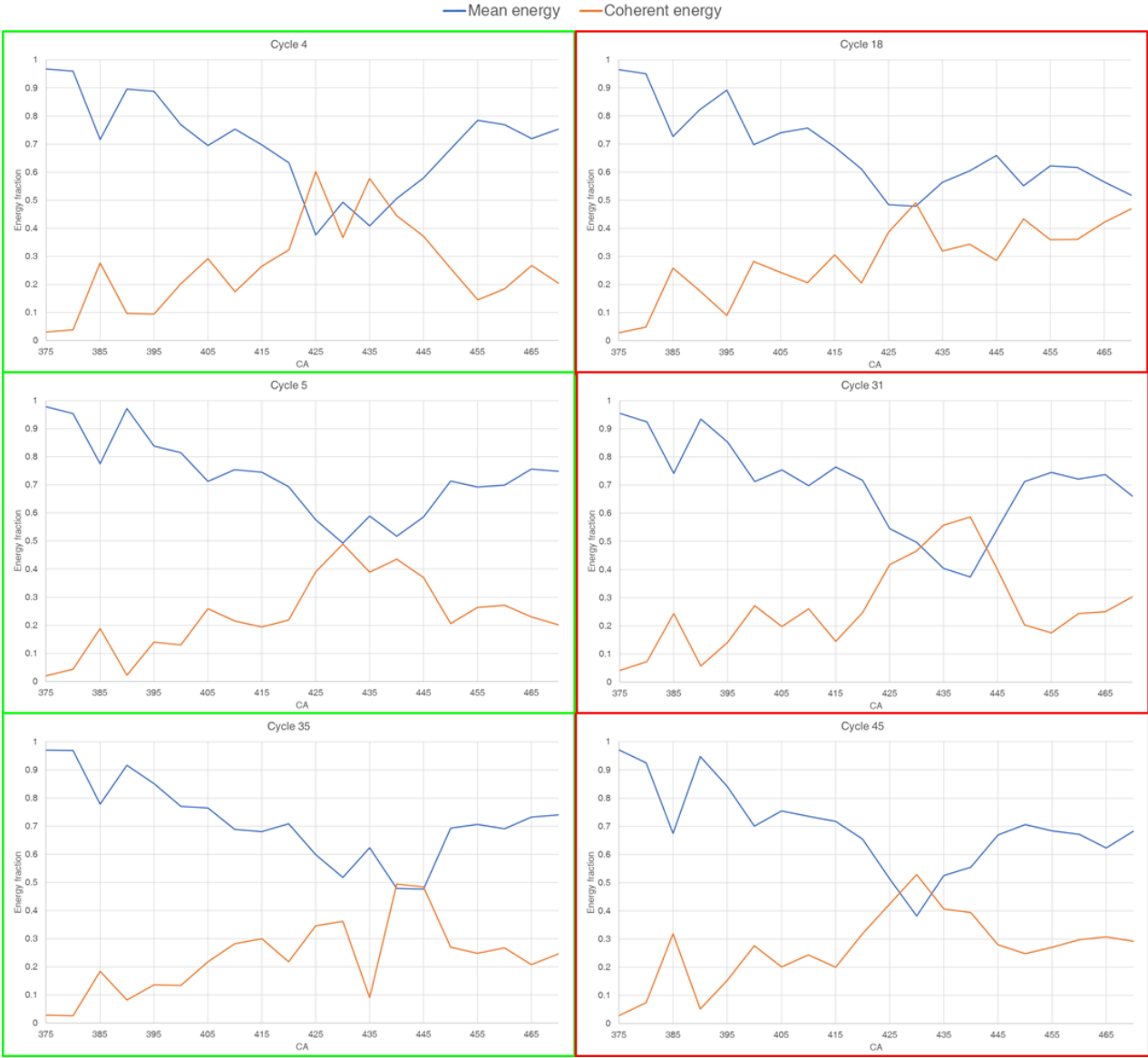


Figure 72 Energy associated with the mean part (in blue) and with the coherent part (in orange) during the intake stroke for least deviating cycles (4, 5 and 35, in green) and most deviating cycles (18, 31 and 45 in red)

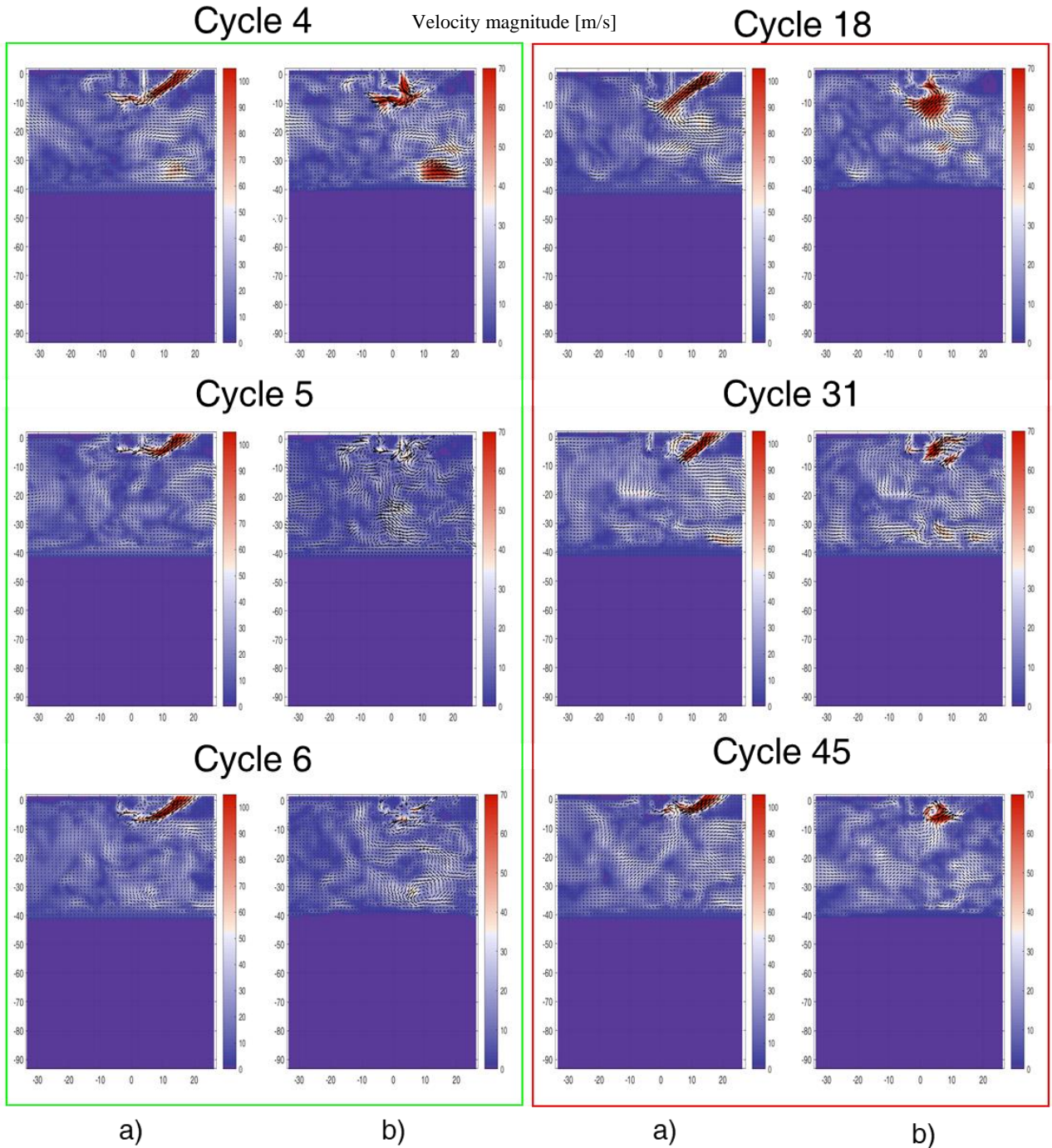


Figure 73 Instantaneous flow field (a) and coherent part of the turbulence (b) for the least (green) and the most (red) deviating cycles at the 425CA position

While the least deviating cycles are very similar, with a slightly more energetic coherent part in cycle 4, the two different behaviors in the least deviating cycles are now clear. In both cycle 31 and cycle 45 a strong recirculation vortex generates a disturbance onto the intake jet: the coherent part shows the recirculation vortex flowing in opposite direction compared to the intake flow. Cycle 18, on the other

side, is deviating from the average because of a higher penetration. The coherent structures are in fact “supporting” the main jet, resulting in a higher intake flow rate. As a matter of fact, cycle 18 is the best cycle in terms of volumetric efficiency.

A detailed view of the recirculation vortex visible for cycle 45 at the 420 CA position is visible in Figure 74 and Figure 75.

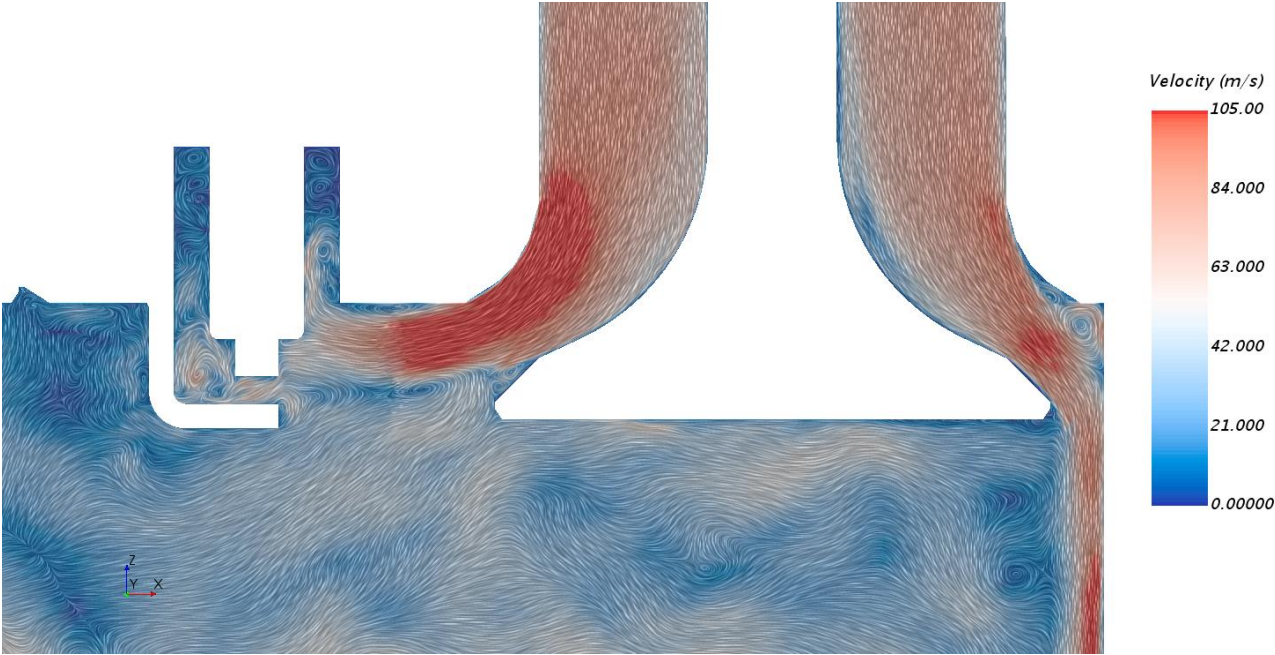


Figure 74 Line integral convolution of the velocity magnitude on the Y=0 plane at the 420 CA position for cycle 45

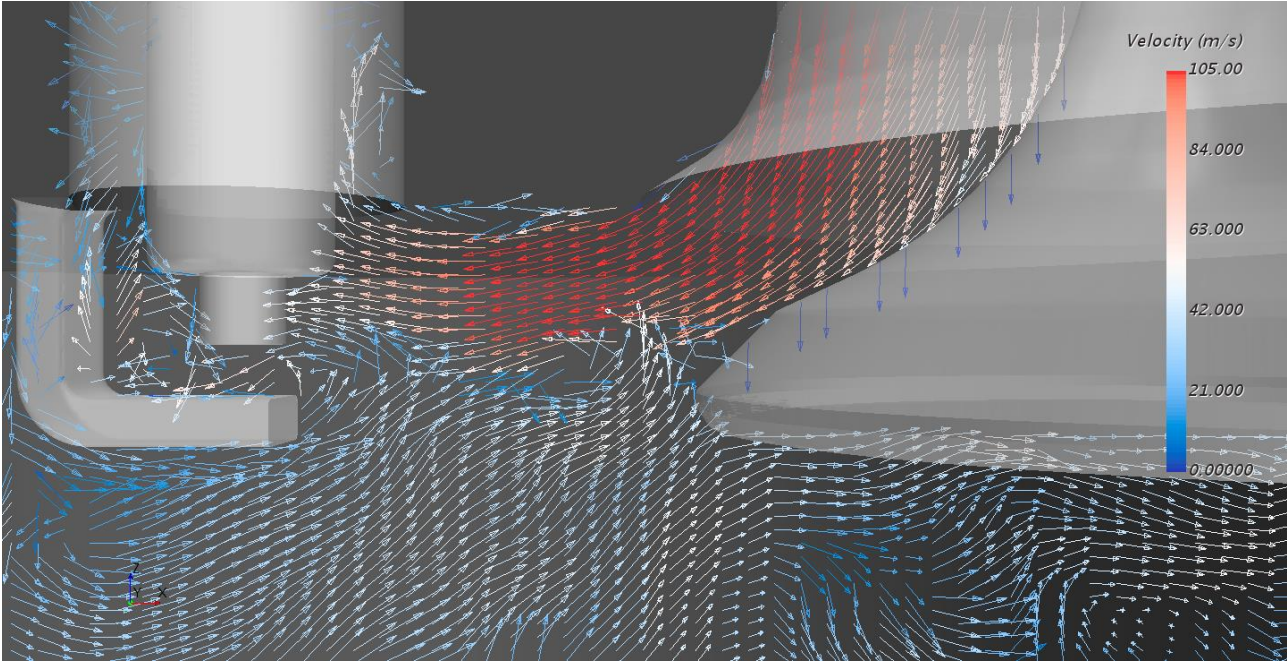


Figure 75 Vector field of velocity showing the detailed view of the recirculation vortex at the 420 CA position for cycle 45

The next logical step is trying to understand the origin of the recirculation vortices responsible for the deviation of cycles 31 and 45, which affects both intake jet bending and penetration. Due to the flat piston of the TCC-III engine, very low residual turbulence is expected after the TDC. Therefore, it is reasonable to suppose that any turbulent structure in the intake stroke is formed as a consequence of the intake flow rate. For this reason, the flow is analyzed in several section planes of the intake port. Figure 76 shows the three section planes analyzed.

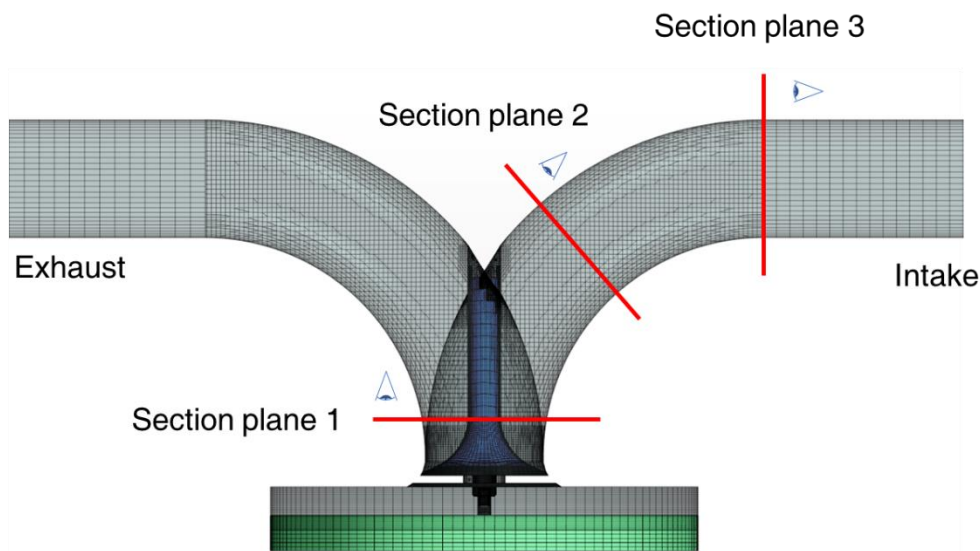


Figure 76 Section planes of the intake port analyzed

In Figure 77 the velocity field relative to section plane 1 is shown at the 470 CA position. Please note that the contour field is relative to the axial velocity magnitude, while the vector field is plotted for the radial velocity relative to the section plane. As expected, the axial velocity is higher in the lower part of the images, corresponding to the intrados, and a recirculation zone is noticeable at the extrados. The least deviating cycles and cycle 18 show a sort of symmetry in the velocity magnitude for the left and the right sides of the valve. On the contrary, cycles 31 and 45 show a clear asymmetry, with a zone of lower velocity caused probably by the higher pressure due to a recirculation vortex. Focusing on cycle 45, the evolution of the velocity field from 420 to 470 CA is shown in Figure 79. Looking at Section 1, the high pressure/low velocity zone denoted in Figure 77 is not present at the preceding CA, and an opposite swirling motion can be spotted from the 420 CA position.

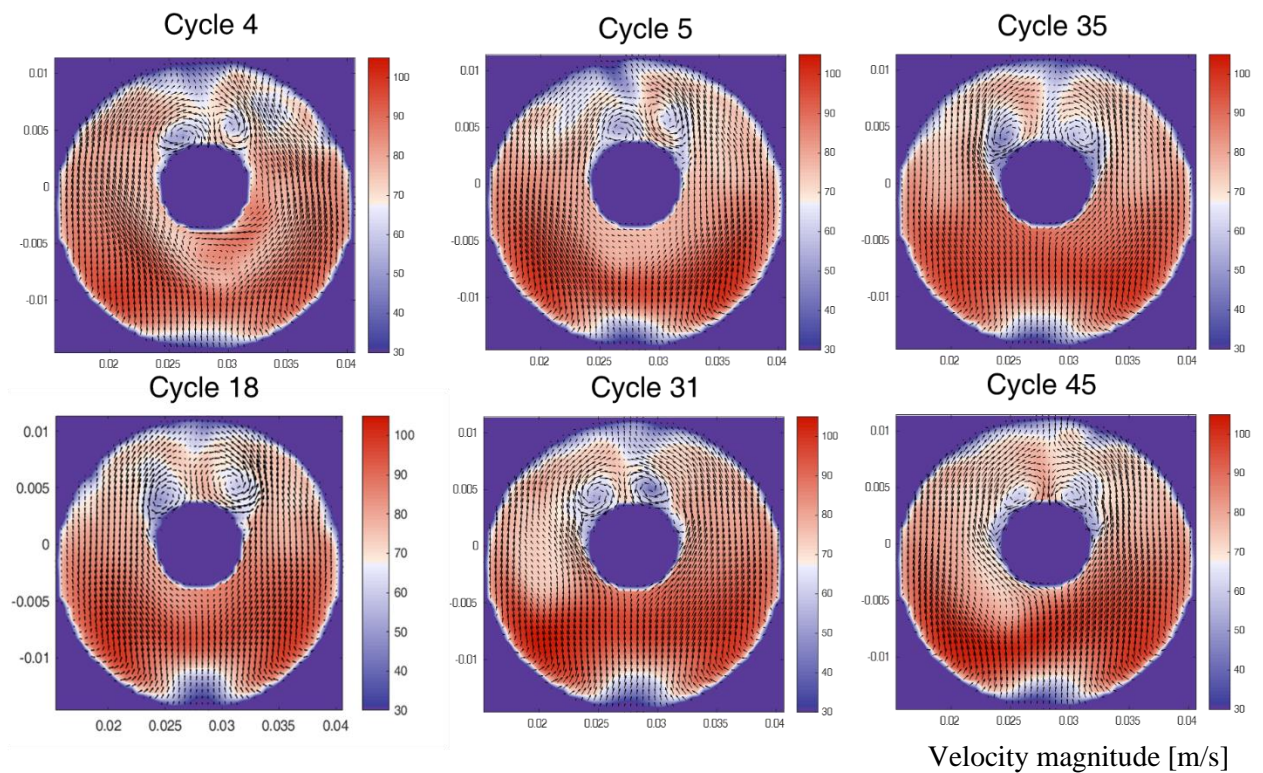


Figure 77 Velocity on the section 1 from Figure 76 at the 470 CA position for the selected cycles.. The contour is relative to the axial velocity, while the vector field comes from the radial components

As shown in Figure 74, the recirculation vortex in the proximity of the valve causes a local increase in pressure that intensifies the effect of the detachment of the velocity flow field from the valve curtain the turbulent structure visible at 420 CA. For a comparison, a different section plane from the same CA is shown in Figure 78, where no recirculation vortex affects the intake jet flow. This perturbation affects the intake jet flow, and it is reasonable to assume that it is related with its evolution. A more detailed analysis would be necessary to investigate the connection between the perturbation and the swirling motion within the intake port, and the interaction of the flow field with the pressure dynamics, whose effects in the velocity field are noticeable, especially in section plane 2 in Figure 79.

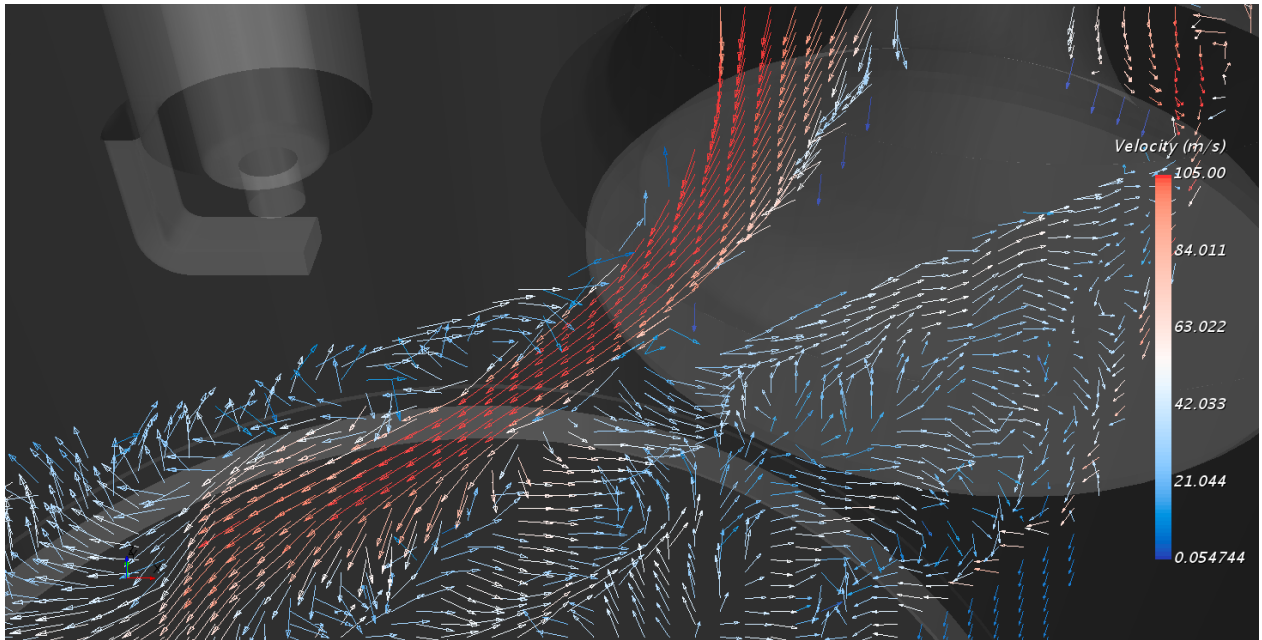
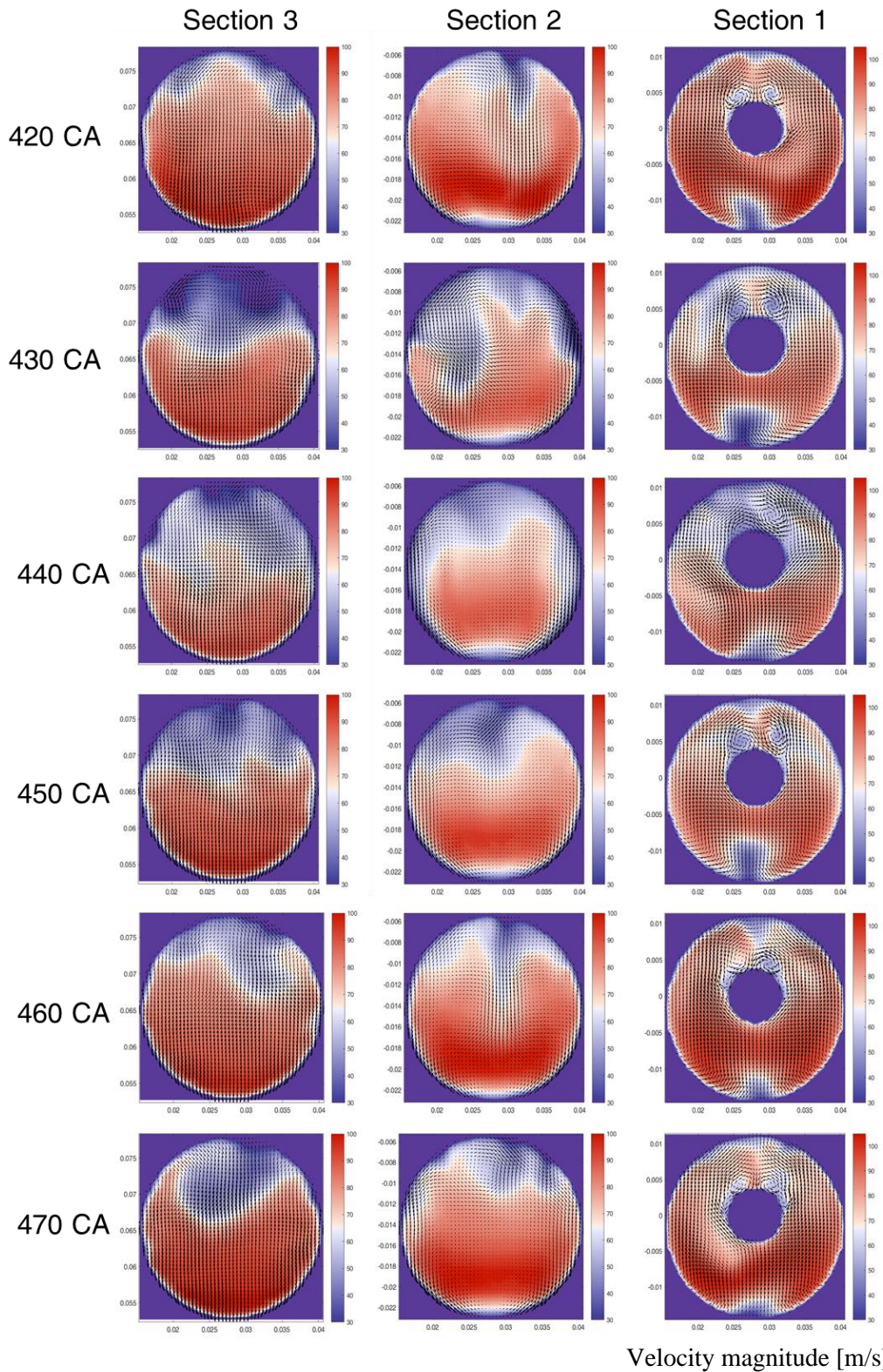


Figure 78 Vector field of the velocity magnitude at the 420CA position for cycle 45 where no recirculation vortex affects the intake jet flow

However, it is possible to assume that avoiding the swirling motion in the intake port could reduce the deviation of the intake stroke. This seems to be confirmed by the comparison of the flow field in section plane 1 with one of the least deviating cycles, for example Cycle 5, shown in Figure 80, where such swirling motion is not recognizable.

The objective of this analysis was not to reach definitive conclusions, but rather to propose a method of analysis based on the POD quadruple decomposition. Defining the most and the least deviating cycles from the 475 CA position is an arbitrary choice, with the idea of reducing the cyclic variability in a specific portion of the cycle. This could be a key factor in the development of an engine. For example, the repeatability of the turbulent flow field near the spark could help reducing the variability associated with the ignition. Also, a repeatable turbulent structure could improve the interaction with the spray in direct-injection engines, enhancing the distribution of the air-fuel mixture. POD quadruple decomposition proved to be a suitable tool for this purpose. Nevertheless, further analysis will be necessary to confirm or disprove the hypothesis that the reduction of the swirling motion inside the intake port could reduce the variability during the intake stroke.



Velocity magnitude [m/s]

Figure 79 Evolution of the velocity flow field for Cycle 45 in the section 1, 2 and 3 referring to Figure 76 from 420 to 470 CA

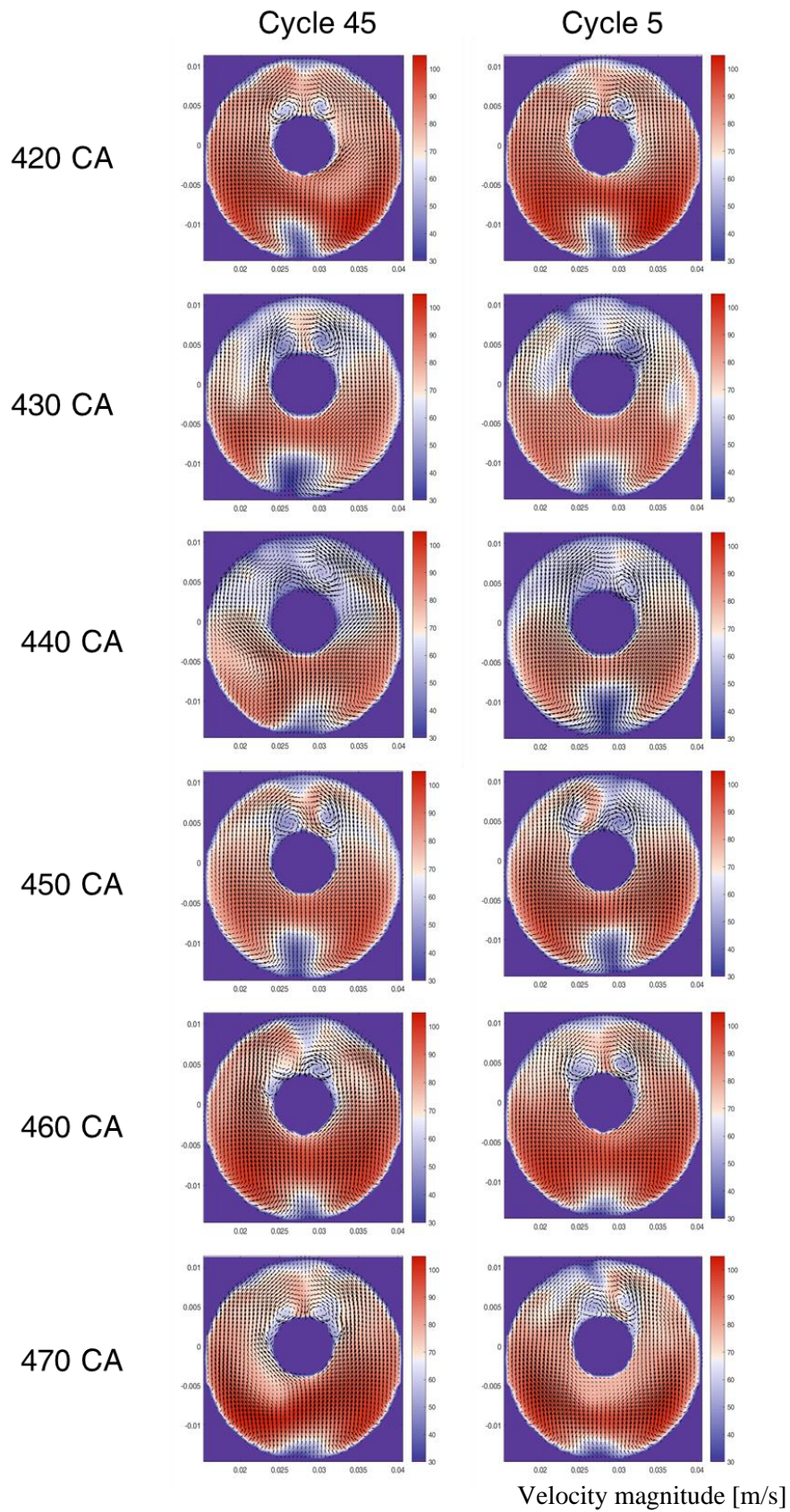


Figure 80 Comparison of the velocity flow field in Section 1 for the high deviating cycle 45 and the low deviating cycle 5

5.4 Conclusions

Overset mesh was demonstrated to be suitable for the CFD simulation of ICE flows, though only few applications are available in the literature. Such lack of contributions is probably due to the complexity of the grid generation process, which must be carefully addressed to handle the small gaps between the valves and valve seats at the valve opening events. Furthermore, the lack of conservativeness of the overset interpolation in closed domains discourages the adoption of the technique. The work shown in this section demonstrates that, by carefully designing the mesh, the application of the overset mesh technique is not only possible but also effective. The overset mesh technique, coupled with the adopted mesh structure, provided enough stability to allow the use of a high-order numerical scheme (MUSCL 3rd order/central-differencing scheme). The application of the overset mesh was eased by the specific geometry of the TCC engine, which allowed the author to design a purposely built grid. However, the technique would be suitable also for 4-valve pentroof configurations typical of modern GDI units. A careful post-processing of a population of 50 LES cycles was performed to discuss the agreement between LES predictions and experimental evidences. The ensemble average fields reveal that the flow topology is reasonably simulated over the whole cycle. This is quantitatively confirmed by the alignment parameter, and POD analysis is performed to confirm the agreement of the most energetic modes over the intake stroke, both in terms of values and trend. Finally, the original quadruple decomposition, applied to the LES results for the first time, gives a further insight on LES capability of simulating the turbulent structures responsible for CCV and, possibly, a tool to identify their origin.

Conclusions and future research

Cycle-to-cycle variability is one of the most limiting factors for the extraction of the full efficiency and emission potential of advanced ICEs. Among the mechanisms that lead to CCV, turbulence is dominant. The TCC-III engine has provided the researchers of a set of reliable and accurate experimental PIV data, allowing the refinement of the calculation techniques by means of an insight on the in-cylinder turbulence.

In this work, the TCC-III engine dataset in motored condition was analyzed for two main purposes:

- Testing post-processing techniques involving Proper Orthogonal Decomposition
- Improving the simulation techniques

Several POD-based flow analysis methods have been critically analyzed. In an attempt to overcome some limitations of these methods, a new method has been proposed. The application of these methods to the TCC-III engine revealed that:

- Much information can be obtained with phase dependent POD, but results must be critically analyzed to avoid misleading interpretations.
- The Conditional Averaging technique is a simple and effective technique, which can provide a reliable qualitative description of CCV. Its major drawback is that it should be limited to large datasets composed of a relevant number of cycles.
- POD triple decomposition is affected by the lack of objectiveness for the definition of the incoherent turbulent part of the flow field.
- POD quadruple decomposition introduces a transition turbulent part of the flow field which should improve the understanding of the energy cascade. Nevertheless, anisotropy is not used as a criterion to individuate the coherent part of turbulence, and the definition of the cutoff number for the incoherent field is not objective.
- The proposed decomposition method introduces a higher degree of objectiveness in the decomposition. Results show a better description of physical phenomena.

All the analyzed techniques are powerful tools for the analysis of turbulent flows, but very little practical information on how to limit CCV can be derived from a standalone application and a methodology of investigation is proposed.

To deepen the analysis, three SGS models were tested to assess the LES capabilities of simulating the CCV. Three datasets of 50 LES cycles were run using the SGS model Static Smagorinsky, Dynamic

Smagorinsky and Dynamic Structure Model. The correlation between field similarity and LES quality was then investigated using two different LES quality indices. The importance of the use of multiple LES quality estimators was discussed. The chosen estimators proved to be able to highlight criticalities in the adopted discretization strategy at the valve curtain region during the early induction phase. Nevertheless, the in-cylinder discretization was found adequate enough to properly resolve the investigated flow. A curtain under-resolution was detected, but it did not prevent reaching a high level of similarity with the PIV measurements.

Phase-dependent POD analysis was then carried out for the PIV data and for each of the adopted SGS models. Comparisons were carried out in terms of mode fraction evolution during a portion of the intake and compression strokes. The main findings of this research are summarized:

- According to the simulated cycles, both Dynamic Smagorinsky and DNS models show high performance, while the lowest values are obtained for the static Smagorinsky model. The best correlation with the PIV data was obtained with the Dynamic Smagorinsky model.
- Despite a ranking in LES quality indices can be clearly established, all the SGS models seem to adequately represent the average flow field evolution. Similarly, none of the models is able to properly estimate the amplitude of flow field variance around the mean. To some extent, this observation seems to suggest that SGS closure plays a secondary role with reference to spatial resolution and near wall discretization.

These findings put the bases for reaching better LES results using the Overset mesh technique. Despite only few applications are available in the literature, Overset mesh was demonstrated to be suitable for the CFD simulation of ICE flows. The overset mesh technique, coupled with the adopted mesh structure, provided enough stability to allow the use of a high-order numerical scheme (MUSCL 3rd order/central-differencing scheme). The application of the Overset mesh was eased by the specific geometry of the TCC engine, which allowed the design a purposely built grid. However, the technique would be suitable also for 4-valve pentroof configurations typical of modern GDI units. A careful post-processing of a population of 50 LES cycles was performed to show the agreement between LES predictions and experimental evidences. The proposed quadruple POD decomposition was applied to assess both the level of accuracy of the results and to understand the origin of the variability. Even though non-definitive conclusions were reached on the origins of CCV, the methodology involving POD quadruple decomposition proved to be suitable for the purpose.

Future work could be addressed in this direction. The added value of a CFD investigation is the accessibility to all the simulated computational domain for every time-step. The interaction between the turbulent motion of the intake port and the cylinder, for example, could only be supposed by observing

the experimental data, while an accurate LES simulation allows a deep analysis of such phenomena. The proposed method of analysis involving the POD quadruple decomposition could be extended to the three-dimensional domains of the cylinder and the intake port. Further methods of analysis for the coherent structures could be performed, such as the lambda2 method, for example. Additionally, more calculation could be performed in order to test hardware modification, such as septa or vortex generator, to induce the formation of desired turbulent structures or to reduce the undesired ones.

Acknowledgments

The TCC engine work has been funded by General Motors through the General Motors University of Michigan Automotive Cooperative Research Laboratory, Engine Systems Division.

The author acknowledges the CINECA award under the ISCRA initiative, for the availability of high-performance computing resources and support.

Definitions / Acronyms

ICE	Internal Combustion Engine
GHG	GreenHouse Gas
CCV	Cycle-to-cycle variability
COV	Coefficient of variation
IMEP	Indicated Mean Effective Pressure
PIV	Particle Image Velocimetry
CFD	Computational fluid dynamics
RANS	Reynolds averaged Navier Stokes
LES	Large Eddy Simulation
DNS	Direct Numerical Simulation
POD	Proper Orthogonal Decoposition
TCC	Transparent Combustion Chamber
CA	Crank Angle
FOV	Field of view
TDC	Top Dead Center
BDC	Bottom Dead Center
FFT	Fast Fourier Transform
u_0	Characteristic velocity of large eddies
l_0	Characteristic length scale of large eddies
τ_0	Characteristic time scale of large eddies
l_{EI}	Length scale defining the energy-containing range of eddies
T_{EI}	Rate of transfer of energy from large eddies to small eddies
ν	Kinematic viscosity
ε	Specific dissipation rate
η	Kolmogorov lengthscale
u_η	Kolmogorov velocity
τ_η	Kolmogorov timescale
l_{DI}	Lenght scale defining inertial subrange

$T(l)$	Rate of transfer of energy from large eddies to small eddies
k	Turbulent kinetic energy
ρ	Density
S_{ij}	Strain rate
μ	Molecular viscosity
μ_t	Turbulent viscosity
σ_k	Turbulent Prandtl number for kinetic energy
σ_ε	Turbulent Prandtl number for dissipation
$C_{1\varepsilon}, C_{2\varepsilon}$	Constants from the k - ε model
$\mathbf{U}(\mathbf{x}, t)$	Velocity field
$\bar{\mathbf{U}}(\mathbf{x}, t)$	Filtered component of the velocity field
$\mathbf{u}'(\mathbf{x}, t)$	Residual component of the velocity field
SGS	Sub-grid scale
$G(\mathbf{x}, \mathbf{x}')$	Filter kernel
τ_{ij}^s	Subgrid-Scale Reynolds stress
τ_{ij}^r	deviatoric residual (SGS) stress tensor
ν_r	residual (SGS) eddy viscosity
\bar{S}	Filtered rate of strain
C_s	Smagorinsky coefficient
P_r	Rate of production of residual kinetic energy
n^+	Distance from the wall in viscous wall units
A^+	Constant in van Driest damping model
τ_{ij}^R	residual (SGS) stress tensor
T_{ij}	modeled Reynolds stress
L_{ij}	resolved stress
k_r	residual kinetic energy
c_{ij}	symmetric tensor for backscattering in DSM model
A_n^m	vector field matrix for POD mathematical procedure
R	covariance matrix
v^i	eigenvectors

λ^i	eigenvalues
ϕ^i	POD modes
a_i	POD coefficients
u^n	snapshot velocity field
e_i	energy fraction
u_{RMS}	Root mean square deviation for the velocity
$\bar{\mathbf{u}}(\mathbf{x}, \phi)$	ensemble average
$\hat{\mathbf{u}}(\Phi)$	conditional average
$M(\Phi)$	number of cases for which the conditional averaging condition is valid
$\langle U_i(X, t) \rangle$	mean cycle average part of the instantaneous flow field
$\tilde{u}_i(X, t)$	fluctuating part of the instantaneous flow field
$S_{u'_i}$	Skewness coefficient
$T_{u'_i}$	Flatness / kurtosis coefficient
R	correlation coefficient
k_{Nyq}	Nyquist limit for the spatial-frequency domain
k_{co}	cut-off spatial frequency
L_{co}	characteristic length scale for the cut-off frequency
IQ_k	Energy resolved LES quality estimator
IQ_ν	Viscosity based LES quality estimator

References

1. Council, N.R., *Committee on the Assessment of Technologies for Improving Light-Duty Vehicle Fuel Economy*, in *Assessment of Fuel Economy Technologies for Light-Duty Vehicles*, T.N.A. Press, Editor. 2011.
2. Laboratory, N.R.E., *Light-Duty Vehicle Attribute Projections (Years 2015-2030)* 2018, California Energy Commission
3. L. Fulton, S.W., *Fuel Economy State of the World 2014: The World is Shifting into Gear on Fuel Economy*. 2014, Global Fuel Economy Initiative.
4. Ozdor, N., M. Dulger, and E. Sher, *Cyclic Variability in Spark Ignition Engines A Literature Survey*. 1994, SAE International.
5. Vermorel, O., et al., *Towards the understanding of cyclic variability in a spark ignited engine using multi-cycle LES*. *Combustion and Flame*, 2009. **156**(8): p. 1525-1541.
6. Johansson, B., *Cycle to Cycle Variations in S.I. Engines - The Effects of Fluid Flow and Gas Composition in the Vicinity of the Spark Plug on Early Combustion*. 1996, SAE International.
7. Baby, X., et al., *A New Methodology to Analyze Cycle-to-Cycle Aerodynamic Variations*. 2002, SAE International.
8. Reuss, D., et al., *Particle Image Velocimetry Measurements in a High-Swirl Engine Used for Evaluation of Computational Fluid Dynamics Calculations*. 1995.
9. Reuss, D.L., *Cyclic Variability of Large-Scale Turbulent Structures in Directed and Undirected IC Engine Flows*. 2000, SAE International.
10. Reuss, D.L., et al., *Instantaneous Planar Measurements of Velocity and Large-Scale Vorticity and Strain Rate in an Engine Using Particle-Image Velocimetry*. 1989, SAE International.
11. Abraham, P., D. Reuss, and V. Sick, *High-Speed Particle Image Velocimetry Study of In-Cylinder Flows with Improved Dynamic Range*. 2013, SAE International.
12. Sick, V., et al. *A Common Engine Platform for Engine LES Development and Validation*. in *LES4ICE, IFP Energies Nouvelles*. 2010. Rueil-Malmaison, France
13. Berni, F., G. Cicalese, and S. Fontanesi, *A modified thermal wall function for the estimation of gas-to-wall heat fluxes in CFD in-cylinder simulations of high performance spark-ignition engines*. *Applied Thermal Engineering*, 2017. **115**: p. 1045-1062.
14. Cicalese, G., F. Berni, and S. Fontanesi, *Integrated In-Cylinder / CHT Methodology for the Simulation of the Engine Thermal Field: An Application to High Performance Turbocharged DISI Engines*. *SAE International Journal of Engines*, 2016. **9**(1): p. 601-617.
15. Angelberger, C., T. Poinot, and B. Delhay, *Improving Near-Wall Combustion and Wall Heat Transfer Modeling in SI Engine Computations*. 1997, SAE International.
16. Zhou, D., et al., *Dual-fuel RCCI engine combustion modeling with detailed chemistry considering flame propagation in partially premixed combustion*. *Applied Energy*, 2017. **203**: p. 164-176.
17. Colin, O., et al., *A thickened flame model for large eddy simulations of turbulent premixed combustion*. *Physics of Fluids*, 2000. **12**(7): p. 1843-1863.
18. Berni, F., et al., *Numerical Investigation on the Effects of Water/Methanol Injection as Knock Suppressor to Increase the Fuel Efficiency of a Highly Downsized GDI Engine*. 2015.
19. Breda, S., et al., *CFD Optimization of n-Butanol Mixture Preparation and Combustion in an Research GDI Engine*. 2017, SAE International.

20. d'Adamo, A., et al., *A RANS knock model to predict the statistical occurrence of engine knock*. Applied Energy, 2017. **191**: p. 251-263.
21. Fontanesi, S., et al., *Knock Tendency Prediction in a High Performance Engine Using LES and Tabulated Chemistry*. Vol. 6. 2013. 98-118.
22. Corti, E., et al., *Comparison of Knock Indexes Based on CFD Analysis*. Energy Procedia, 2016. **101**: p. 917-924.
23. Granet, V., et al., *Large-Eddy Simulation and experimental study of cycle-to-cycle variations of stable and unstable operating points in a spark ignition engine*. Combustion and Flame, 2012. **159**(4): p. 1562-1575.
24. Enaux, B., et al., *LES study of cycle-to-cycle variations in a spark ignition engine*. 2011. **33**: p. 3115-3122.
25. d'Adamo, A., et al., *Understanding the Origin of Cycle-to-Cycle Variation Using Large-Eddy Simulation: Similarities and Differences between a Homogeneous Low-Revving Speed Research Engine and a Production DI Turbocharged Engine*. 2018, SAE International.
26. Hardy, R.L., *Theory and applications of the multiquadric-biharmonic method 20 years of discovery 1968–1988*. Computers & Mathematics with Applications, 1990. **19**(8): p. 163-208.
27. Benek, J., J. Steger, and F.C. Dougherty, *A flexible grid embedding technique with application to the Euler equations*, in *6th Computational Fluid Dynamics Conference Danvers*. 1983, American Institute of Aeronautics and Astronautics.
28. Berton, A., F. D'Orrico, and M. Sideri, *Overset grids for fluid dynamics analysis of internal combustion engines*. Energy Procedia, 2017. **126**: p. 979-986.
29. Scarcelli, R., et al., *Cycle-to-Cycle Variations in Multi-Cycle Engine RANS Simulations*. 2016, SAE International.
30. Buhl, S., F. Hartmann, and C. Hasse, *Identification of Large-Scale Structure Fluctuations in IC Engines using POD-Based Conditional Averaging*. Oil Gas Sci. Technol. – Rev. IFP Energies nouvelles, 2016. **71**(1): p. 1.
31. Rutland, C.J., *Large-eddy simulations for internal combustion engines – a review*. International Journal of Engine Research, 2011. **12**(5): p. 421-451.
32. Celik, I., I. Yavuz, and A. Smirnov, *Large eddy simulations of in-cylinder turbulence for internal combustion engines: A review*. International Journal of Engine Research, 2001. **2**(2): p. 119-148.
33. Haworth, D.C., *Large-Eddy Simulation of in-Cylinder Flows*. Oil & Gas Science and Technology - Rev. IFP, 1999. **54**(2): p. 175-185.
34. Geurts, B.J. and J. Fröhlich, *A framework for predicting accuracy limitations in large-eddy simulation*. Physics of Fluids, 2002. **14**(6): p. L41-L44.
35. Celik, I.B., Z.N. Cehreli, and I. Yavuz, *Index of Resolution Quality for Large Eddy Simulations*. Journal of Fluids Engineering, 2005. **127**(5): p. 949-958.
36. di Mare, F., R. Knappstein, and M. Baumann, *Application of LES-quality criteria to internal combustion engine flows*. Computers & Fluids, 2014. **89**: p. 200-213.
37. Haworth, D.C., Jansen, K., *Large-eddy simulation on unstructured deforming meshes: towards reciprocating IC engines*. Comput. Fluids, 2000. **29**(5): p. 493-524.
38. Jagus, K. and X. Jiang, *Large Eddy Simulation of Diesel Fuel Injection and Mixing in a HSDI Engine*. Flow, Turbulence and Combustion, 2011. **87**(2): p. 473-491.

39. Baumann, M., F. di Mare, and J. Janicka, *On the Validation of Large Eddy Simulation Applied to Internal Combustion Engine Flows Part II: Numerical Analysis*. Flow, Turbulence and Combustion, 2014. **92**(1): p. 299-317.
40. d'Adamo, A., et al., *LES Modelling of Spark-Ignition Cycle-to-Cycle Variability on a Highly Downsized DISI Engine*. SAE International Journal of Engines, 2015. **8**(5): p. 2029-2041.
41. Shekhawat, Y., et al., *An Experimental and Simulation Study of Early Flame Development in a Homogeneous-charge Spark-Ignition Engine*. Oil and Gas Science and Technology, 2017. **72**(5).
42. Hasse, C., V. Sohm, and B. Durst, *Numerical investigation of cyclic variations in gasoline engines using a hybrid URANS/LES modeling approach*. Computers & Fluids, 2010. **39**(1): p. 25-48.
43. Funk, C., et al., *Turbulence Properties of High and Low Swirl In-Cylinder Flows*. 2002, SAE International.
44. H Joo, S., et al., *The behaviour of small- And large-scale variations of in-cylinder flow during intake and compression strokes in a motored four-valve spark ignition engine*. Vol. 5. 2004. 317-328.
45. Lumley, J.L., *The structure of inhomogeneous turbulent flows*. Atmospheric Turbulence and Radio Wave Propagation (A. M. Yaglom and V. I. Tararsky, eds.), 1967: p. 166-178.
46. Chatterjee, A., *An introduction to the proper orthogonal decomposition*. Current Science, 2000. **78**(7): p. 808-817.
47. Fogleman, M., et al., *Application of the proper orthogonal decomposition to datasets of internal combustion engine flows*. Journal of Turbulence, 2004. **5**: p. N23.
48. Ko I., M.K., Rulli F., D'Adamo A., Berni F., Fontanesi S. , *Investigation of Sub-Grid Model Effect on the Accuracy of In-Cylinder LES of the TCC Engine under Motored Conditions*. SAE Technical Paper, 2017. **2017-24-0040**.
49. Fontanesi, S., D'Adamo, A., Paltrinieri, S., Cantore, G., Rutland, C., *Assessment of the Potential of Proper Orthogonal Decomposition for the Analysis of Combustion CCV and Knock Tendency in a High Performance Engine*. SAE Technical Paper, 2013. **2013-24-0031**.
50. Liu, K. and D. C. Haworth, *Development and Assessment of Proper Orthogonal Decomposition for Analysis of Turbulent Flow in Piston Engines*. 2010.
51. Abraham, P., et al., *Evaluating Large-Eddy Simulation (LES) and High-Speed Particle Image Velocimetry (PIV) with Phase-Invariant Proper Orthogonal Decomposition (POD)*. Oil Gas Sci. Technol. – Rev. IFP Energies nouvelles, 2014. **69**(1): p. 41-59.
52. Arányi, P., et al., *Analysis of different POD methods for PIV-measurements in complex unsteady flows*. International Journal of Heat and Fluid Flow, 2013. **43**: p. 204-211.
53. Graftieux, L., M. Michard, and N. Grosjean, *Combining PIV, POD and vortex identification algorithms for the study of unsteady turbulent swirling flows*. Measurement Science and Technology, 2001. **12**(9): p. 1422.
54. Hao, C., et al., *A practical guide for using proper orthogonal decomposition in engine research*. International Journal of Engine Research, 2012. **14**(4): p. 307-319.
55. Sirovich, L., *Turbulence and the dynamics of coherent structures. I - Coherent structures. II - Symmetries and transformations. III - Dynamics and scaling*. Vol. 45. 1987.

56. Roudnitzky, S., P. Druault, and P. Guibert, *Proper orthogonal decomposition of in-cylinder engine flow into mean component, coherent structures and random Gaussian fluctuations*. Journal of Turbulence, 2006. **7**: p. N70.
57. Qin, W., et al., *Large eddy simulation and proper orthogonal decomposition analysis of turbulent flows in a direct injection spark ignition engine: Cyclic variation and effect of valve lift*. Science China Technological Sciences, 2014. **57**(3): p. 489-504.
58. Schiffmann, P., et al., *TCC-III Engine Benchmark for Large-Eddy Simulation of IC Engine Flows*. Oil Gas Sci. Technol. – Rev. IFP Energies nouvelles, 2016. **71**(1): p. 3.
59. Morse, A.P., J.H. Whitelaw, and M. Yianneskis, *Turbulent Flow Measurements by Laser-Doppler Anemometry in Motored Piston-Cylinder Assemblies*. Journal of Fluids Engineering, 1979. **101**(2): p. 208-216.
60. Khalighi, B., D.C. Haworth, and M.S. Huebler, *Multidimensional Port-and-in-Cylinder Flow Calculations and Flow Visualization Study in an Internal Combustion Engine with Different Intake Configurations*. SAE Transactions, 1994. **103**: p. 805-822.
61. Reuss, D.L. and M. Rosalik. *PIV Measurements During Combustion in a Reciprocating Internal Combustion Engine*. in *Laser Techniques Applied to Fluid Mechanics*. 2000. Berlin, Heidelberg: Springer Berlin Heidelberg.
62. Funk, C., et al., *Turbulence Properties of High and Low Swirl In-Cylinder Flows*. 2002.
63. Pope, S.B., *Turbulent Flows*. 2000: Cambridge University Press.
64. BARDINA, J., J. FERZIGER, and W. REYNOLDS, *Improved subgrid-scale models for large-eddy simulation*, in *13th Fluid and PlasmaDynamics Conference*.
65. Germano, M., et al., *A dynamic subgrid-scale eddy viscosity model*. Physics of Fluids A: Fluid Dynamics, 1991. **3**(7): p. 1760-1765.
66. Chumakov, S.G. and C.J. Rutland, *Dynamic structure subgrid-scale models for large eddy simulation*. International Journal for Numerical Methods in Fluids, 2005. **47**(8-9): p. 911-923.
67. Chen, H., D.L. Reuss, and V. Sick, *On the use and interpretation of proper orthogonal decomposition of in-cylinder engine flows*. Measurement Science and Technology, 2012. **23**(8): p. 085302.
68. Bizon, K., et al., *Application of Proper Orthogonal Decomposition to the analysis of I.C.E. space and time resolved data*. 2007, Consiglio Nazionale delle Ricerche.
69. Bizon, K., et al., *POD-based analysis of combustion images in optically accessible engines*. Combustion and Flame, 2010. **157**(4): p. 632-640.
70. Chen, H., et al., *A practical guide for using proper orthogonal decomposition in engine research*. International Journal of Engine Research, 2012. **14**(4): p. 307-319.
71. Rulli, F., et al., *A critical review of flow field analysis methods involving proper orthogonal decomposition and quadruple proper orthogonal decomposition for internal combustion engines*. International Journal of Engine Research, 2019: p. 1468087419836178.
72. Liu, K., et al., *Large-eddy Simulation of Motored Flow in a Two-valve Piston Engine: POD Analysis and Cycle-to-cycle Variations*. Flow, Turbulence and Combustion, 2013. **91**(2): p. 373-403.
73. Yusoff, S. and B. Yap, *Comparison of conventional measures of skewness and kurtosis for small sample size*. 2012. 1-6.
74. Ali, M.M., *Stochastic Ordering and Kurtosis Measure*. Journal of the American Statistical Association, 1974. **69**(346): p. 543-545.

75. Wang, T., et al., *Large-eddy simulation of in-cylinder flow in a DISI engine with charge motion control valve: Proper orthogonal decomposition analysis and cyclic variation*. Vol. 75. 2015. 561-574.
76. Enaux, B., et al., *Large Eddy Simulation of a Motored Single-Cylinder Piston Engine: Numerical Strategies and Validation*. Flow, Turbulence and Combustion, 2011. **86**(2): p. 153-177.
77. Choi, H. and P. Moin, *Effects of the Computational Time Step on Numerical Solutions of Turbulent Flow*. Journal of Computational Physics, 1994. **113**(1): p. 1-4.
78. Pope, S.B., *Ten questions concerning the large-eddy simulation of turbulent flows*. New Journal of Physics, 2004. **6**: p. 35-35.
79. Kravchenko, A.G. and P. Moin, *On the Effect of Numerical Errors in Large Eddy Simulations of Turbulent Flows*. Journal of Computational Physics, 1997. **131**(2): p. 310-322.
80. Meyers, J., B.J. Geurts, and M. Baelmans, *Database analysis of errors in large-eddy simulation*. Physics of Fluids, 2003. **15**(9): p. 2740-2755.
81. Celik, I., M. Klein, and J. Janicka, *Assessment Measures for Engineering LES Applications*. Journal of Fluids Engineering, 2009. **131**(3).
82. Davidson, L., *Large Eddy Simulations: How to evaluate resolution*. International Journal of Heat and Fluid Flow, 2009. **30**(5): p. 1016-1025.
83. Ko, I., et al., *Study of LES Quality Criteria in a Motored Internal Combustion Engine*. 2017, SAE International.
84. Rulli, F., et al., *LES analysis of the turbulent flow in an optically accessible internal combustion engine using the Overset mesh technique*. International Journal of Engine Research, 2020.
85. Hadzic, H., *Development and Application of a Finite Volume Method for the Computation of Flows Around Moving Bodies on Unstructured, Overlapping Grids*, in *Arbeitsbereiche Schiffbau*. 2006: Auflage, Hamburg.
86. Buhl, S., et al., *A comparative study of intake and exhaust port modeling strategies for scale-resolving engine simulations*. International Journal of Engine Research, 2017. **19**(3): p. 282-292.
87. Barbato, A., et al., *A Comparison between Different Moving Grid Techniques for the Analysis of the TCC Engine under Motored Conditions*. 2019, SAE International.
88. Stansfield, P., et al., *PIV analysis of in-cylinder flow structures over a range of realistic engine speeds*. Experiments in Fluids, 2007. **43**(1): p. 135-146.